INVESTIGATION OF DRY AND NEAR-DRY ELECTRICAL DISCHARGE MILLING PROCESSES

by

Jia Tao

A dissertation submitted in partial fulfillment
of the requirements for the degree of
Doctor of Philosophy
(Mechanical Engineering)
in The University Of Michigan
2008

Doctoral Committee:

Professor Albert J. Shih, Co-Chair
Professor Jun Ni, Co-Chair
Professor Elijah Kannatey-Asibu Jr.
Professor Lumin Wang
Yue-Feng Luo, Federal-Mogul Corporation

ACKNOWLEDGEMENTS

First of all, I would like to thank my advisors, Profs. Albert Shih and Jun Ni for their insightful guidance and relentless efforts on my PhD study. I also would like to thank Dr. Yue-feng Luo for his practical advice and generous assistance on this research. I also thank Drs. Lumin Wang and Elijah Kannatey-Asibu Jr. for their careful review of this dissertation and valuable comments as a committee member.

My research was primarily sponsored by the Advanced Technology Program of the National Institute of Standards and Technology. I am grateful to George Qiao of S.M. Wu Manufacturing Research Center, Prof. Jyoti Mazumder and Dr. Bhaskar Dutta of POM Group, Dr. Jim Wu of Stellite Coatings, Dr. Jean-Louis Staudenmann of National Institute of Standards and Technology, Prof. Wansheng Zhao, Dr. Yongbing Li and Yan Jia of Shanghai Jiao Tong University, John MacGregor and Chuck Sannes of Ann Arbor Machine Company for their technical support and remarkable assistance on my research. I particularly thank my friends at S.M. Wu Manufacturing Research Center for their supports and encouragements.

Finally, I would like to express my especial gratitude to my wife and my family for their continued support throughout my PhD journey.

TABLE OF CONTENTS

CHAPTER

LIST OF FIGURES

LIST OF TABLES

CHAPTER 1

INTRODUCTION

This research aims to develop an innovative electrical discharge machining (EDM) process, i.e., dry and near-dry EDM milling, as the finishing technology for rapid and precision die, mold and tool fabrication. Applied as the post-process of direct metal deposition (DMD), the dry and near-dry EDM milling processes are targeted to finish the near-net-shape parts produced by DMD.

1.1. Research Backgrounds

Conventional fabrication of die and mold is a time consuming multi-step process, beginning with a block of raw material, followed by computer numeric control (CNC) machining, heat treatment, CNC machining to near net shape, and finishing by EDM, electro-chemical discharge machining (ECDM) or manual polishing. In general, the forging dies produced in the U.S. requires a lead time of at least 5 weeks (Fallbohmer et al., 1996). Therefore, it has always been desirable to seek a more time efficient and cost effective process for the die and mold manufacturing.

DMD is an emerging method that allows for a short-time and low-cost delivery of dies or molds (Mazumder et al., 1997). DMD is a multi-layer metal cladding process where a fully dense clad layer is produced pixel by pixel by melting metal powder with a laser beam. A hardened near-net-shape part can be generated in a single step through DMD, thus eliminating several intermediate steps in conventional fabrication process. By depositing material at the damaged location of the tool, DMD can also be used for on-site tooling repair. In all, DMD is regarded as a time and cost efficient method for die, mold and tool manufacturing.

For the near-net-shape part produced by DMD, the observed surface finish is on the order of 20 μm, geometric accuracy is of 170 to 250 μm, and the material is of high hardness with fine microstructures (Mazumder et al., 2000). A proper post processing method is necessary to finish the DMD part in precision applications.

Due to its unique feature of machining metals regardless of hardness, EDM is widely used in the die and mold manufacturing industry, where high hardness, intricate geometry and stringent surface quality requirement are encountered (Altan et al., 1993). Considering the high hardness and potential complex sculpture surface of the DMD part, EDM becomes the top candidate for its post processing.

1.2. Research Motivation

In spite of the advantages, conventional EDM process has certain limitations in production application, including low material removal rate, long lead time for pre-shaped tool preparation, large tool wear, environmental concern caused by toxic dielectric disposal, etc. It is the purpose of this research to develop a EDM process compatible with the DMD process and in the mean while enhancing the conventional EDM performance and alleviating certain constrains. Innovations will be applied on two aspects of the EDM process, the machining dielectric medium and the machine configuration. The importance of these two aspects and their prospects in EDM process enhancement will be discussed in the following sections.

1.2.2. Dielectric Medium

The dielectric medium plays an essential role in the EDM process. It not only works as the insulation medium between the polarized electrodes to induce discharge, but also influences the plasma channel expansion and material erosion during the discharge, and the debris flushing and discharge gap reconditioning after the discharge. Therefore, understanding and selecting the right dielectric medium with proper electrical, mechanical and thermal properties is considered a thrust area of this research.

According to the type of dielectric medium used, there are several categories of EDM processes, including wet EDM, powder mixed dielectric (PMD) EDM, dry EDM and near-dry EDM. Conventional EDM uses liquid dielectric medium, such as hydrocarbon oil or deionized water, and it is therefore called wet EDM. Even though it is a well established process, some problems associated with wet EDM are electrolysis corrosion when using water as the dielectric and toxic hydrocarbon disposal when kerosene based dielectric is used (Yeo et al., 1998; Leao and Pashby, 2004).

PMD EDM can enhance the machining performance of wet EDM. It utilizes powder mixed liquid dielectrics and has the advantage of achieving good machining stability and finishing quality, especially in the finish operation with small discharge energy (Mohri et al., 1985; 1987). However, the usage of powder increases the machining cost and the consequent toxic disposal causes more environmental concern (Yeo et al., 1998). For production practices, the powder suspended dielectric circulation system is also challenged by separating the machined debris from the useful powders and maintaining a constant powder concentration.

Dry EDM, which applies high flow rate gaseous dielectric fluid, tends to alleviate the environmental problem resulted from the liquid and powder mixed dielectrics and also enhance the machining performance. Using inert gas to drill small holes (NASA, 1985) is the first dry EDM attempt. Oxygen has been identified by Kunieda et al. (1991; 1997) as an ideal dielectric medium for high material removal rate (MRR) in dry EDM. By applying oxygen, a discharge duration lower than 5μs can stimulate the "quasi-explosion" mode and accelerate the material removal significantly (Yu et al., 2003). In addition to the high material removal capability, extremely low tool wear ratio is also observed. Therefore, Kunieda et al. (2004) and Yu et al. (2003; 2004) applied oxygen in EDM milling process, where the electrode tool wear used to be a concern, and achieved great success in the roughing performance. The shortcomings of dry EDM include low quality of surface finish due to debris reattachment, odor of burning and very low MRR when using non-oxygen gases (Yoshida et al., 1998; Kao et al., 2006).

As an alternative method, the near-dry EDM uses liquid-gas mixture as the dielectric medium. The liquid content in the mist media helps to solidify and flush away the molten debris and hence the debris reattachment is alleviated in near-dry EDM. After the first exploitation by Tanimura et al. (1989), not much study has been conducted on this process until recently by Kao et al. (2007) in near-dry wire EDM. It is found that near-dry EDM has the advantage in finish operation with low discharge energy considering its higher MRR than wet EDM and better surface finish quality than dry EDM.

Among all different types, dry EDM and near-dry EDM are of large interest for this research. First, since high machining speed and ultra-fine surface finish is demanded for our EDM post-processing technology, a potential match is perceived from the high MRR capability of the oxygen-assisted dry EDM and the good finish quality potential with the near-dry EDM. In addition, dry EDM or near-dry EDM does not need a fluid tank to submerge the workpiece, as opposed to conventional wet EDM. The simpler system configuration makes it possible for the in-situ integration with the DMD process by sharing the operation chamber for DMD and EDM. Therefore, gases and liquid-gas mixtures will be investigated as the dielectric fluid in this research and enhanced machining performance is anticipated from dry and near-dry EDM.

1.2.1. EDM Machine Configuration

Generally, EDM can be categorized into three types: wire EDM, die-sinking EDM and EDM milling (Bleys, 2005). Wire EDM, as shown in Figure 1.1(a), uses traveling wire as electrode to cut the profile along the workpiece. With 3-D orientation of the wire electrode, intricate profile can be attained with high precision. However, wire EDM is limited from making cavity geometries due to the thread-through configuration of the wire supply, and therefore it is not suitable for our particular application of sculpture surface machining in die, mold and tool fabrication.

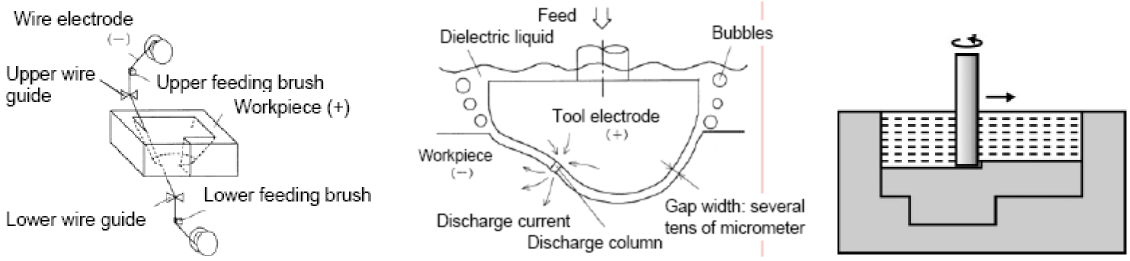

(a) (b) (c)

Figure 1.1. EDM configuratios, (a) wire EDM (Kunieda et al., 2005), (b) sinking EDM (Kunieda et al., 2005) and (c) EDM milling (Bleys et al., 2005)

Die-sinking EDM, as shown in Figure 1.1(b), is widely used for making or finishing mold cavity, which can contain complex sculpture surfaces. Die-sinking EDM uses pre-shaped electrode, which is usually machined out of bulk copper or graphite, and copies the electrode geometry to the workpiece thus generating the part with free-form surfaces. However, the need of pre-shaped electrode retards the whole process because the electrode shaping takes time and extra machining cost and several electrodes may be needed, depending on the finishing requirement, owing to the significant electrode wear during EDM.

Considering these constrains, it would be ideal if a more flexible EDM configuration is available. EDM milling, as shown in Figure 1.1(c), is a relatively new concept that can meet this criterion. It uses a rotating cylindrical or tubular tool electrode to traverse along the workpiece and thus make free form surfaces. Eliminating the needs of pre-shaping the electrode, EDM milling would make the machining process easier by using standard size cylindrical or tubular electrode. However, some challenges of its practical implementation are: need of machining parameter rearrangement due to the different machining condition encountered in EDM milling that has relatively small erosion area as opposite to conventional die-sinking EDM where large area machining is usually applied (Luo, 1998b); need of compensation algorithm for electrode tool wear, which is quite significant in the EDM process (Bleys et al., 2004); and ideally need of five degree of freedom (5DOF) electrode orientation capability for freeform surface machining.

This research investigates the EDM milling configuration considering its potential benefits and the areas needed for further exploration. In addition, the milling configuration fits well with dry and near-dry EDM because it can apply tubular tool electrode, through which the gas or liquid-gas dielectric can be delivered directly to the machining region with no need of a submerging tank.

1.3. Research Objectives and Tasks

The objective of this research is to investigate the dry and near-dry EDM milling processes for rapid and high quality finish machining. The process is expected to achieve 0.1 μm R_a surface finish on the final finished surface within a reasonable processing cycle time.

However, it is a challenge for the EDM process to achieve the 0.1 μm R_a target, which indicates an ultra-fine surface finish with mirror-like appearance. It is because the surface generated by EDM is inherently rugged due to the natural of its material removal mechanism. In EDM, the workpiece material is removed by rapidly recurring consecutive electrical discharge pulses, each of which erodes small amount of material and leaving a discharge crater on the machined surface, resulting in a machined surface composed of multiple discharge craters overlapped on each other. Even though it has been practiced to achieve ultra-fine surface finish with EDM by providing low discharge energy to smooth individual discharge craters (Luo and Chen, 1990), it sacrifices the MRR drastically and does not meet our rapid machining requirement.

Therefore, this research aims to thoroughly exploit the dry and near-dry EDM processes for good surface finish with high MRR capacity. Advantages and potential of different gases and liquid-gas mixtures will be investigated and compared. The properties of the dielectric fluid will be optimized by selecting the right gas or liquid-gas medium and tailoring the liquid-gas combination in the mixture dielectric fluid. In addition, process parameters that dominate the EDM process will be investigated and optimized. As a whole, a set of process parameters specifically selected for dry and near-dry EDM milling processes will be presented to enable the high quality finish machining with reasonable machining speed.

Furthermore, a model of the EDM process will be constructed to better understand the mechanism of the material removal process. It can be used to facilitate the process selection and improvement.

1.4. Outline

This dissertation presents observations, results, and future research directions of dry and near-dry EDM. Chapter 2 investigated the dry and near-dry EDM milling for roughing operation. Targeting a high MRR, the process investigation is carried out by studying the effects of different dielectric fluids, electrode materials and process parameters. An ideal combination of these variables will be presented to facilitate the high speed roughing process. A projected response surface will be generated to characterize the roughing operation within certain range of the discharge parameters to facilitate the parameter selection meeting different machining requirements. Attempt is also made to explain the mechanism of high MRR EDM process.

Chapter 3 investigates the dry and near-dry EDM milling for finish machining. Targeting a smooth surface finish, a similar investigation procedure applied in the roughing process study, is carried out to study the effects of different dielectric fluids, electrode materials and process parameters. Key factors of high quality, mirror-like surface finish, have been identified and considered achievable via near-dry EDM milling process. Efforts are made to realize the mirror-like surface finish in two ways, stretching the capacity of a low-end EDM pulse generator and implementing an advanced EDM pulse generator. The capability of the near-dry EDM to achieve a 0.1 μm R_a surface finish is demonstrated. Finally, the roughing and finishing dry and near-dry EDM processes are integrated and its capability is demonstrated to finish a DMD part.

Chapter 4 provides an in-depth understanding of the EDM process by building a model to simulate the crater formation during an electrical discharge. With the aid of a commercial computational fluid dynamics (CFD) package, the behaviors of the workpiece material, including melting, splashing, ejection and resolidification, within a cycle of electrical discharge can be simulated and a close to real discharge crater can be obtained. The experimental validation is presented to evaluate the model. The model confirms the advantage of near-dry EDM in finish machining and the effect of lower discharge pulse energy for better EDM surface finish quality.

The conclusions and recommendations for future work are presented in Chapter 5.

CHAPTER 2

ROUGH MACHINING BY DRY AND NEAR-DRY EDM MILLING

2.1. Introduction

Dry EDM using oxygen as the machining medium can be applied to achieve very high MRR for the rouging process. Kunieda et al. (1997; 2001; 2003) first explored the process by applying oxygen gas through a rotating tubular electrode to conduct dry EDM milling. MRR higher than that of the conventional wet EDM was achieved under the so-called “quasi-explosion” mode (Kunieda et al., 2003). The study expands this concept and looks into the oxygen-assisted high MRR dry process.

In addition to the dry EDM, the near-dry EDM with varied liquid-gas mixture is also investigated for high MRR. The feasibility of near-dry EDM was explored by Tanimura et al. (1987), who investigated EDM in water mists with air, nitrogen and argon gases. Further investigation of near-dry EDM was conducted by Kao et al. (2007) in wire EDM experiments. The advantage of near-dry EDM was identified as stable machining process at low discharge energy finish machining. In addition, good machined surface integrity without debris reattachment that occurred in dry EDM was attained since the liquid enhances the debris flushing. Other potential advantages of near-dry EDM are the broad selection of gases and liquids and flexibility to adjust the concentration of liquid in gas. The dielectric properties can thus be tailored in near-dry EDM to meet various machining needs, such as high MRR or fine surface finish. The technical barrier in dry and near-dry EDM lies in the selection of proper dielectric medium and process parameters. Therefore, it becomes the goal of this research to explore the process capability and parameter selection of the dry and near-dry EDM processes through experimental studies.

The dielectric fluid and its delivery method are critical to the performance of EDM. The electrical, mechanical and thermal properties of the dielectric fluid influence the processes of discharge initiation, plasma expansion, material erosion, debris removal, and discharge channel reconditioning in EDM (Kunieda et al., 2005). Table 2.1 summarizes key properties of the gas and liquid as EDM dielectric fluids. Properties of the liquid-gas mixture are expected to lie in-between the properties of the base materials.

Table 2.1. Electrical, thermal, and mechanical properties of liquid and gas dielectric media at room temperature*.

	Liquid		Gas			
	Deionized water	Kerosene / hydrocarbon oil	Air	N_2	O_2	He
Dielectric strength (MV/m)	13	14 to 22	3.0	2.8	2.6	1.2
Dielectric constant	80	1.8	1.0	1.0	1.0	1.1
Dynamic Viscosity (g/m-s)	0.92	1.6	0.019	0.017	0.020	0.020
Thermal conductivity (W/m-K)	0.61	0.15	0.026	0.025	0.026	0.015
Heat capacity (J/g-K)	4.2	2.2	1.0	1.0	0.92	5.2

*(Shugg, 1986; Yaws, 1995; Avallone and Baumeister, 1996; Vedensky and Vul, 1965; Gerasimov, 2005; Peyton, 2002; Forsythe, 2003; Incropera and DeWitt, 2007)

The dielectric strength determines the gap distance between the electrode and workpiece. Higher dielectric strength requires a higher electric field to breakdown the dielectric fluid, and thus decreases the gap distance. Liquid dielectric media have higher dielectric strength (> 10 MV/m) than that of gas dielectric media (< 4 MV/m). The dielectric constant determines the stray capacitance induced by the overlapping area between the electrode and workpiece. Large inertia and viscosity of the fluid increase the bubble expansion force and material removal per discharge (Hockenberry and Williams, 1967). The larger inertia and higher viscosity of the liquid dielectric indicate a higher MRR potential but rougher surface finish. Heat conductivity and heat capacity are important factors that affect the solidification of molten debris and the cooling of the electrode and the workpiece surfaces (Koenig et al., 1975). In Table 2.1, the liquid dielectric fluids have the thermal conductivity and heat capacity at least 10 times and twice that of gas dielectric fluids (except for He, which has exceptionally high heat capacity). A wide range of dielectric properties can be obtained by using different compositions and properties of the dielectric media, and dry and near-dry EDM will thus yield a diverse range of performance compared with conventional wet EDM. This study investigates the high MRR roughing process by implementing the dry and near-dry EDM.

In the chapter, the experimental setup and design for dry and near-dry EDM is first presented. The selection of dielectric medium and electrode material, exploratory experiments is conducted to determine the setup for the external air jet, depth of cut, discharge current and pulse duration, and then detailed design of experiments (DOE) is conducted to explore the effect of discharge parameters on the EDM roughing process. Finally the mechanism for high MRR in the oxygen-assisted dry EDM is discussed.

2.2. Experimental Setup and Design

2.2.1. Experimental Setup

The dry and near-dry EDM milling experiments are conducted on a Vanguard 150H CNC die-sinking EDM machine from EDM Solutions. A rotary spindle, Rotobore RBS-1000, with through-spindle flushing capability is used to hold the tubular electrode. Figure 2.1(a) shows the setup of the spindle, tool electrode and dielectric medium inlet. The spindle rotates the tool electrode to maintain uniform tool wear and enhance the debris removal. The dielectric fluid, which can be in the form of liquid, gas or liquid-gas mixture, is delivered through a tubular tool electrode. The liquid-gas mixture is generated by an AMCOL 6000 pulsed spray generator, as shown in Figure 2.1(b), designed for minimum quantity lubrication (MQL) machining applications. In this study, the input liquid flow rate is fixed at 5 ml/min. Figure 2.1(c) shows the setup of a nozzle to deliver chilled air jet (around −3°C) from an Exair Model 5215 cold gun system. The external air jet helps to solidify and flush away the molten debris. This is especially useful in the high MRR process which generates large amount of molten debris.

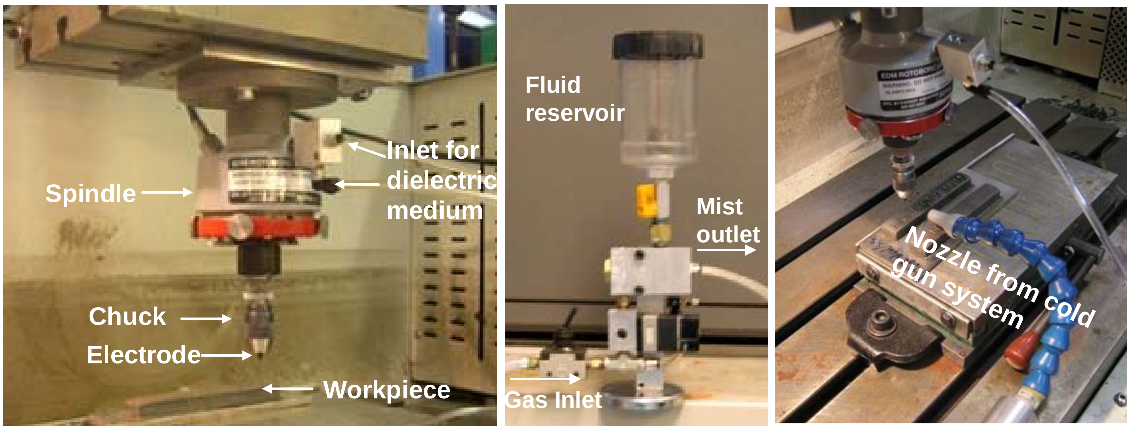

(a) (b) (c)

Figure 2.1. Dry and near-dry EDM experimental setup: (a) rotary spindle and electrode, (b) spray delivery device and (c) nozzle to deliver cold air

The experimental process variables and settings are summarized in Table 2.2. The workpiece material is AISI H13 tool steel deposited by DMD process. Copper and graphite, the two most commonly used electrode materials in EDM, are evaluated at this point. The tubular electrode is of 3 mm outer diameter and 1.5 and 1 mm inner diameter for copper and graphite electrode, respectively. For liquid dielectrics, deionized water and kerosene are selected. The liquid dielectric is mixed with four types of gas: air, oxygen, nitrogen, and helium in near-dry EDM. Oxygen is expected to yield high MRR (Kunieda et al., 2003), air is a readily available gas, helium has very high heat capacity and is an inert gas which is expected to prevent oxidation and improve surface quality, and nitrogen can potentially form a hard nitride layer on steel workpiece surface to improve the wear resistance (Yan et al., 2005). The kerosene-oxygen mixture is excluded from investigation owing to the risk of fire and explosion (Kunieda and Furuoya, 1991).

The depth of cut (DOC) is varied between 0.1 to 0.6 mm in roughing operation to achieve high MRR. The electrode rotational speed is fixed at 250 rpm since no obvious influence is observed at higher speed.

The discharge parameters are also important factors in EDM. The discharge current (i_e) and discharge duration (t_i) determine the discharge energy per pulse; the pulse interval (t_0) decides the time available for gap reconditioning between two consecutive discharges; the gap voltage (u_{gap}) and open circuit voltage (u_i) controls the discharge gap distance. In this research, different levels of these discharge parameters are selected to study dry and near-dry EDM processes. As to the electrode polarity, negative polarity or cathode is applied on the tool electrode in all dry EDM for reduced tool wear (Kunieda, 2003) and in the near-dry EDM with water based liquid-gas mixture to reduce electrolysis corrosion (Jilani et al., 1984). Positive polarity or anode is applied on the tool electrode for near-dry EDM with kerosene based liquid-gas mixture. It provides higher cathode or workpiece removal rate when kerosene is used as a dielectric fluid in EDM with discharge duration longer than 3 μs (Arunachalam, 1995).

Table 2.2. Process parameters for dry and near-dry EDM experiment.

Machining media	Workpiece material:	AISI H13 from DMD
	Electrode material:	copper, graphite
	Dielectric fluid:	Liquid: deionized water, kerosene Gas: oxygen, air, nitrogen, helium Liquid-gas mixture: water with oxygen, air, nitrogen, or helium; kerosene with air, nitrogen, or helium
Machining parameters	Depth of cut (mm):	0.1−0.6
	Electrode diameter (mm):	3
	Electrode rotary speed (rpm):	250
Discharge parameters	Discharge current (A):	20, 25, 30, 40
	Pulse duration (μs):	4, 8, 12
	Pulse interval (μs):	4, 8, 16, 20, 40
	Gap voltage (V):	160, 210, 260
	Open circuit voltage (V):	40, 60, 80
	Polarity:	Dry EDM and near-dry EDM with water mixture: Electrode negative Near-dry EDM with kerosene mixture: Electrode positive

2.2.2. Experimental Procedures

Figure 2.2 illustrates the configuration of the EDM milling process. Grooves of 8 mm in length and varied depth for different processes are made. To measure the surface roughness at the bottom of the slot, a Taylor Hobson Form Talysurf profilometer with 2 μm stylus radius was used. The cut off length is set to 0.8 mm. The measurement length was set to 8 mm. The weight of the part before and after machining is measured using an Ohaus GA110 electronic scale with 0.1 mg resolution and is then converted to the volumetric material removal to calculate the MRR.

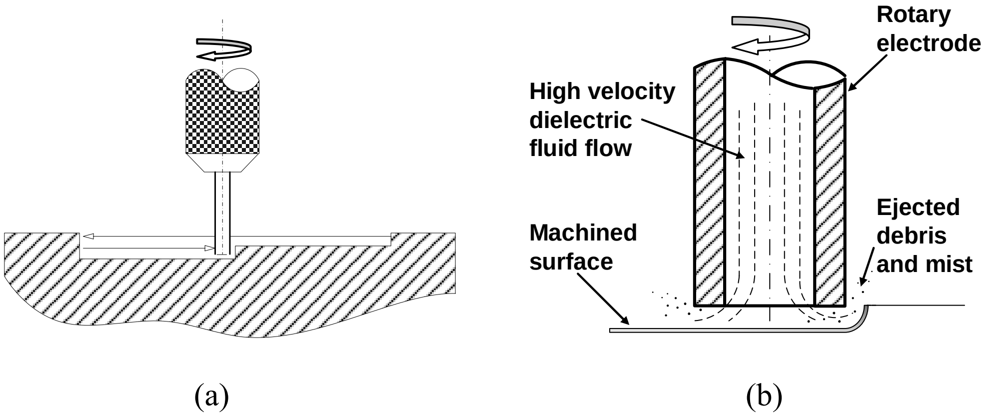

(a) (b)

Figure 2.2. Configuration of EDM milling: (a) overview and (b) close-up view of the electrode and cutting region.

The experimental investigation of dry and near-dry EDM roughing processes is carried out in three sets of experiments, marked as Exps. I, II and III.

1. Exp. I. Dielectric Medium and Electrode Material Selection: Screening experiments are conducted to select the candidate dielectric medium and electrode material for the roughing operation. The depth of cut and input pressure are fixed at 0.1 mm and 480 kPa.
2. Exp. II. Exploratory Experiments: Based on the selected dielectric medium and electrode material, several sets of exploratory experiment are conducted to investigate the effects of external air jet, depth of cut and extreme discharge conditions.
3. Exp. III. Design of Experiments (DOE): The DOE test based on a 2^{5-1} fractional

factorial design is performed to study the effect of five parameters (i_e, t_i, u_{gap}, t_0 and u_i) and their interactions. The 2^{5-1} fractional factorial design requires smaller number of experiments than the full factorial design but it has a compounding effect with resolution V (five). It means the effect of the nth order interaction tends to entangle with that of the 5-nth order interaction. In general, lower order interaction has stronger effect than the higher order interaction. Hence, the current design is capable of detecting up to the second order interaction. Four center points are used in the design to test the curvature effect of the model. The design matrices are listed in Table 2.3. Analysis of variance (ANOVA) is applied to analyze the main effects and interactions of input parameters (Carrano et al., 2004; Luis et al., 2005; Puertas et al., 2005). The response surfaces of MRR and surface roughness can be generated through DOE to predict the performance of the roughing operation.

Table 2.3. Experiments design for roughing process

Run	t_i (μs)	i_e (A)	u_i (V)	u_{gap} (V)	t_0 (μs)	Run	t_i (μs)	i_e (A)	u_i (V)	u_{gap} (V)	t_0 (μs)
1	4	20	160	40	20	11	4	30	160	80	20
2	12	20	160	40	8	12	12	30	160	80	8
3	4	30	160	40	8	13	4	20	260	80	20
4	12	30	160	40	20	14	12	20	260	80	8
5	4	20	260	40	8	15	4	30	260	80	8
6	12	20	260	40	20	16	12	30	260	80	20
7	4	30	260	40	20	17	8	25	210	60	14
8	12	30	260	40	8	18	8	25	210	60	14
9	4	20	160	80	8	19	8	25	210	60	14
10	12	20	160	80	20	20	8	25	210	60	14

2.3. Exp. I Results – Electrode Material and Dielectric Medium

Figure 2.3 shows the results on MRR and surface roughness at high discharge energy input. The copper electrode is capable to remove work-material in nearly all dry and near-dry EDM cases (except for the near-dry EDM with kerosene-nitrogen and kerosene-helium mixture). For the graphite electrode, even though it can cut material effectively in the wet EDM condition, it is not suitable for the dry and near-dry EDM roughing process due to severe arcing. Deposited workpiece material, similar to that in arc welding, was observed at the outer circumference of the machined spot, as shown in Figure 2.4(a). The severe arcing causes discharge localization and large scale material melting, while ideal sparks should uniformly distribute over the machining area and erode material. The arcing is likely stimulated by the excessive amount of graphite powder chipped off from the electrode tip, as shown in Figure 2.4(b). The concentration of discharges on the edge of the electrode, which first confronts the workpiece material in the machining, results in dramatically uneven distribution of the thermal load. The gas or liquid-gas flushing with low cooling efficiency is not effective enough to alleviate the excessive temperature rise along the electrode edge. Resultantly, the induced thermal stress cracked the brittle graphite electrode. The graphite powder bridged the workpiece and electrode causing discharge localization and thus arcing. Therefore, graphite turns out not suitable for the dry or near-dry EDM milling process even though it is widely used in high MRR die-sinking EDM scenario.

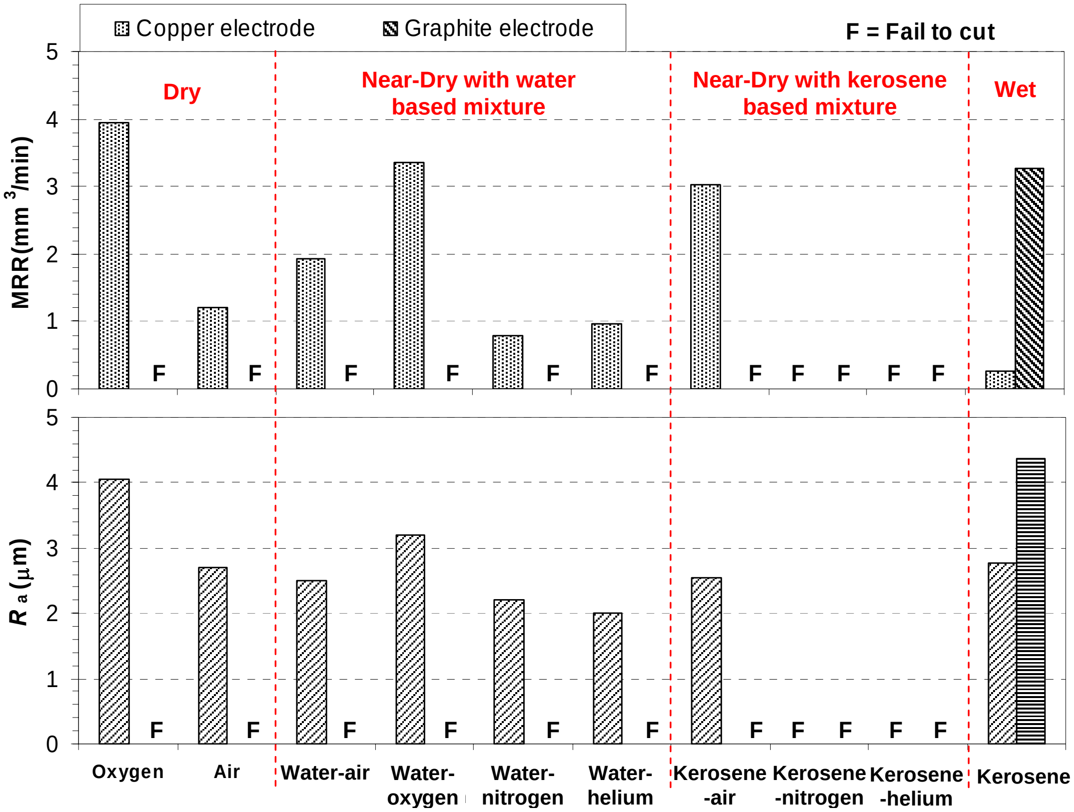

Figure 2.3. MRR and R_a results of different dielectric fluids for copper and graphite electrode materials at high discharge energy input (i_e = 10 A, t_i = 4 μs, t_0 = 8 μs, u_{gap} = 60 V and u_i = 200 V)

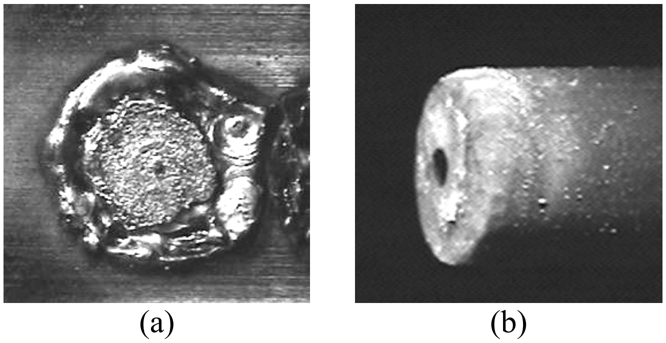
(a) (b)

Figure 2.4. Graphite electrode in near-dry EDM at high discharge current: (a) damaged workpiece surface due to arcing and (b) damaged tool (i_e = 10 A, t_i = 4 μs, t_0 = 8 μs, u_{gap} = 60 V and u_i = 200 V)

For the effect of dielectric medium, as shown in Figure 2.3, oxygen, water-oxygen mixture, and kerosene-air mixture are found to achieve comparable MRR and better surface finish than liquid kerosene in wet EDM. The lower viscosity of the liquid-gas mixture resulted in shallower craters on the machined surface and thus better surface finish.

Since oxygen is confirmed to have the highest MRR, its potential is to be further exploited in this study. Water-oxygen mixture can be another good candidate for roughing since it provides high MRR close to that of oxygen and yielded low R_a value. However, the water combined with oxygen content induces severe corrosion or oxidation resulting in rusty look of the machined surface. Compared with oxygen, the kerosene based liquid-gas mixture encounters the problem of excessive tool wear. As shown in Figure 2.5, very obvious tool wear pattern is seen when using kerosene-air mixture as the dielectric fluid while consistent geometry is observed on the slot machined with the oxygen.

In all, the combination of copper electrode and oxygen gas is the top selection for further study of high MRR roughing EDM.

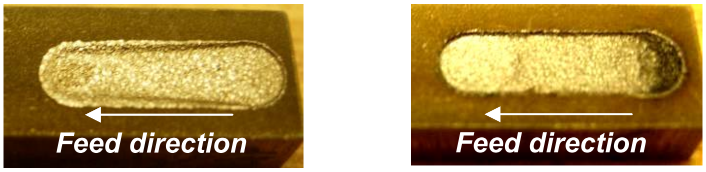

(a) (b)

Figure 2.5. Sample slots machined by (a) kerosene-air mixture and (b) oxygen (i_e = 20 A, t_i = 4 μs, t_0 = 8 μs, u_{gap} = 60 V and u_i = 200 V)

2.4. Exp. II Results – Exploration of External Air Jet, Depth of Cut and Discharge Current

The application of external air jet, selection of depth of cut and exploration of extreme discharge conditions are investigated to further understand the oxygen-assisted dry EDM roughing processes.

2.4.1. External Air Jet

Blowing an air jet externally to the EDM region can improve the surface quality in roughing EDM, where high discharge energy generates a large amount of molten debris. Flushing solely with the gas supplied through the tubular electrode is not enough to remove all the molten debris. As observed in Figure 2.6(a), spherical debris droplets re-solidify to the machined surface and deteriorated the surface quality. The tool electrode also had the same problem of debris deposition. Aided by the external air jet, the molten debris is better chilled and flushed away. As a result, the surface finish and appearance is improved and the shape of the electrode is better maintained, as shown in Figure 2.6(b). In addition, arcing frequency is greatly reduced due to the improved discharge gap conditioning. The surface finish, R_z, was improved from 112 to 94 μm and the MRR is also increased, from 20 to 22 mm^3/min, by applying the external air jet close to the EDM region. Hence, all following DOE roughing EDM experiments are then carried out with the air jet assisted debris flushing.

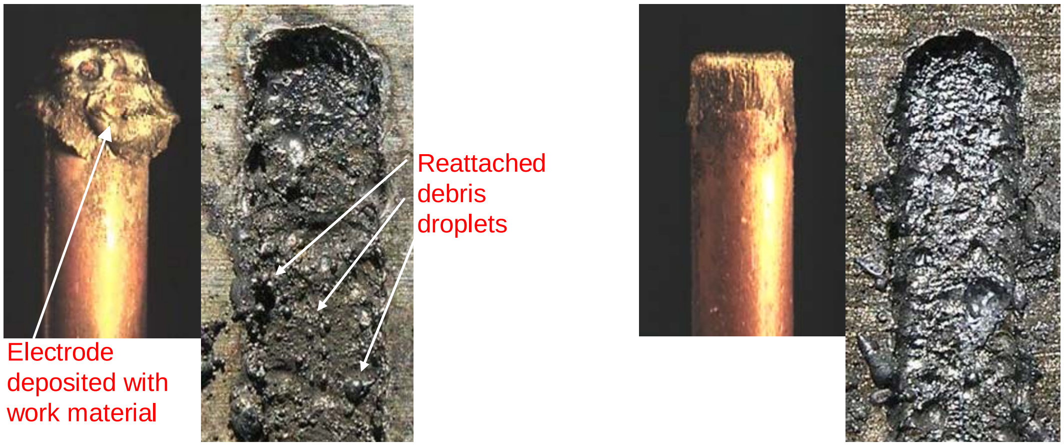

(a) (b)

Figure 2.6. Worn electrode and grooves milled using oxygen as dielectric fluid (i_e = 40 A, t_i = 4 μs, t_0 = 8 μs, u_{gap} = 60 V and u_i = 200 V): (a) without using cold gun (R_z = 112 μm, MRR = 20 mm^3/min) and (b) using cold gun (R_z = 94 μm, MRR = 22 mm^3/min).

2.4.2. Depth of Cut

Figure 2.7 shows the effect of depth of cut in oxygen-assisted dry EDM. The MRR reached the maximum, 22 mm^3/min, at 500 μm depth of cut. When the depth of cut is beyond 500 μm, the increase of MRR saturates due to the debris removal problem. The debris can bridge between the electrode sidewall and workpiece, resulting in arcing or short circuit. This is confirmed by observing frequent servo retraction of the electrode to regulate the discharge condition. The surface roughness is generally not affected by the depth of cut because it does not influence the discharge condition at the bottom of the electrode. In the following DOE roughing experiments with oxygen, the depth of cut is set at 500 μm.

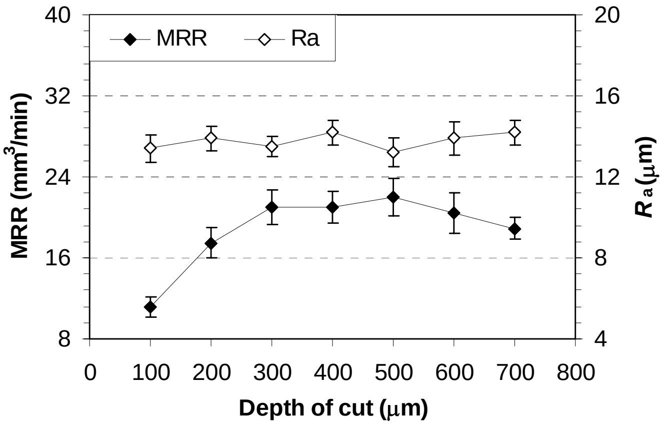

Figure 2.7. Effect of depth of cut on dry EDM rough cutting with oxygen (i_e = 30 A, t_i = 4 μs, t_0 = 8 μs, u_{gap} = 60 V and u_i = 200 V)

2.4.3. Abnormal Discharges and Explosion Mode

For roughing EDM, at certain discharge parameter settings of high discharge energy input, i.e., high i_e (≥ 40 A) and low t_0 (≤ 2 μs) the discharge can occur in the explosion mode (Kunieda et al., 2003) with uncontrollable material removal and excessive electrode wear, as shown in Figure 2.8. With the observation, the following DOE exploration is conducted in a parameter region that avoids the abnormal discharges. The reason for stimulation of the explosion mode in oxygen-assisted dry EDM will be discussed in Section 2.6.

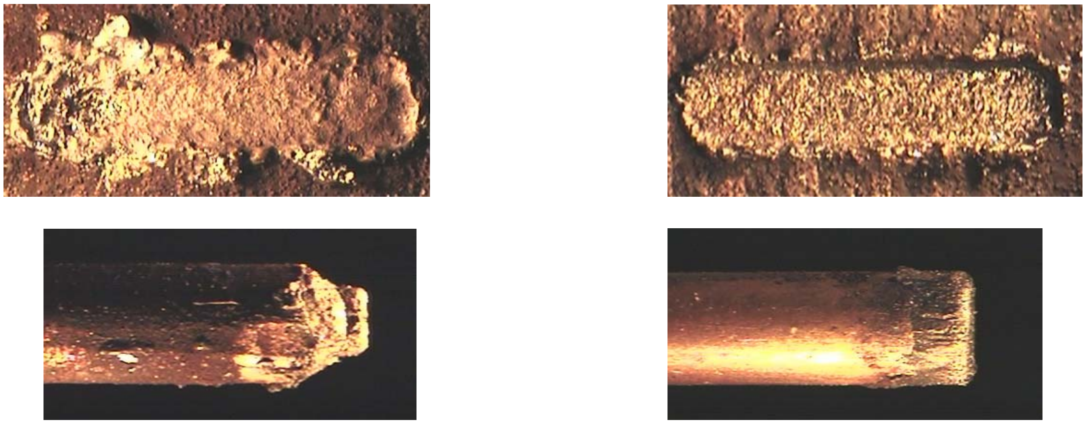
(a) (b)

Figure 2.8. Comparison the effect of (a) explosion mode (i_e = 40 A, t_i = 12 μs, t_0 = 8 μs, u_e = 60 V and u_i = 200 V), and (b) normal mode (i_e = 20 A, t_i = 4 μs, t_0 = 8 μs, u_{gap} = 60 V and u_i = 200 V).

2.5. Exp. III Results – Design of Experiments (DOE)

The DOE results for oxygen-assisted dry EDM roughing are summarized in Table 2.4. The ANOVA indicates that the significant factors influencing the MRR are discharge pulse duration, t_i, discharge current, i_e, and discharge interval, t_0, and the second order interaction, i_e*t_0. The t_i and i_e are well recognized important EDM process parameters because they determine the discharge energy. The significance of t_0 is consistent with the study of Kunieda et al. (2003), who reported that by maintaining t_0 in the range of 5 to 10 μs, the discharge was under the 'quasi-explosion mode' and the MRR was considerably increased compared with that at longer t_0.

Table 2.4. MRR and R_a results for roughing process.

Run	1	2	3	4	5	6	7	8	9	10
MRR (mm^3/min)	1.14	7.89	26.04	3.23	3.26	2.19	2.21	50.0	2.95	2.74
R_a (μm)	4.37	4.32	17.94	3.82	3.66	3.67	4.47	20.2	4.35	3.99
Run	**11**	**12**	**13**	**14**	**15**	**16**	**17**	**18**	**19**	**20**
MRR (mm^3/min)	2.43	36.04	1.20	12.5	28.2	6.10	5.76	5.90	5.93	5.29
R_a (μm)	5.01	18.75	6.13	4.15	17.34	4.52	5.58	5.98	5.31	5.68

The response surfaces of MRR and surface roughness vs. t_i, i_e and t_0 are shown in Figures 2.9(a) and (b), respectively. In the first plot of Figure 2.9(a), a very steep rise of MRR is observed when increasing i_e and decreasing t_0. It indicates that both high i_e ($\geq$ 25 A) and low t_0 ($\leq$ 10 μs) are required to promote the intense MRR mode in oxygen-assisted dry EDM. In Kunieda's study (2003), all experiments were conducted at i_e = 40 A, and hence only the significance of t_0 on the discharge mode was noticed. In this experiment, the effect of i_e is also addressed. The high discharge energy input via high i_e and high discharge frequency as a result of low t_0 stimulates the rapid exothermal oxidation and generates extra amount of heat. As a result of the intensified heat, the MRR is dramatically increased. In the following section, the mechanism of this rapid oxidation in oxygen-assisted dry EDM will be discussed in detail.

The main factors, i_e and t_0, and second order interactions, i_e*t_0, i_e*t_i and t_i*t_0 are found as the significant terms influencing the R_a value. Figure 2.9(b) shows their effects. Generally, lower i_e and higher t_0 yields a better surface finish. The effect of t_i on surface finish is complicated. In the last two plots of Figure 2.9(b), at high i_e or low t_0 (high MRR), higher t_i increases the surface roughness. However, at low i_e or high t_0 (low MRR), reducing t_i unexpectedly increases the surface roughness. As shown in Figure 2.10 are the enlarged pictures of the EDM surface at normal discharge mode. At low t_i (= 4 μs), milling marks can be observed on the machined surface. With low t_i, low i_e and high t_0, the energy input is small and it is not appropriate for large depth of cut. The material removal was not efficient and the electrode feeding was slow with frequent electrode retraction, which caused the milling marks. This explains why the surface roughness cannot be improved although the MRR has been reduced at low t_i.

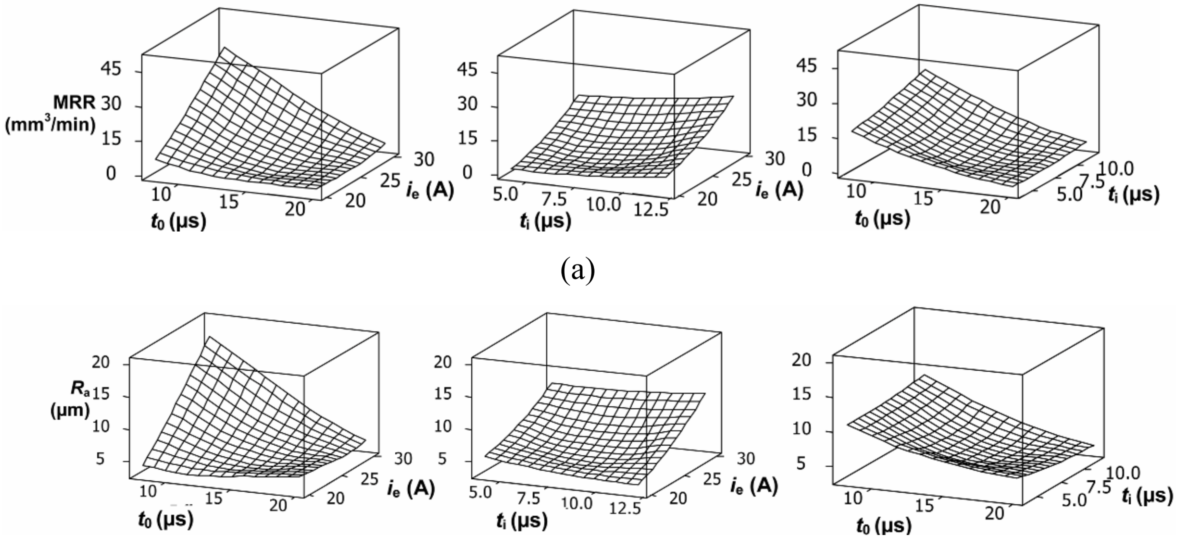

(a)

(b)

Figure 2.9. Projected surfaces of (a) MRR and (b) R_a versus i_e and t_0, i_e and t_i, and t_i and t_0 for roughing EDM

(a) $t_i = 12$ μs

(b) $t_i = 4$ μs

Figure 2.10. EDM surfaces at normal discharge mode: (a) without milling mark, $R_a = 4.32$ μm ($i_e = 20$ A, $t_i = 12$ μs, $t_0 = 8$ μs, $u_{gap} = 40$ V and $u_i = 160$ V) and (b) with milling mark, $R_a = 6.13$ μm ($i_e = 20$ A, $t_i = 4$ μs, $t_0 = 20$ μs, $u_{gap} = 80$ V and $u_i = 260$ V)

At extremely high i_e (≥ 25 A) and low t_0 (≤ 10 μs), the surface roughness is poor, exceeding 25 μm R_a. Figure 2.11 shows the optical micrographs of the surface after quasi-explosion mode EDM. Deep craters as a result of arcing or energy concentration caused by rapid oxidation can be observed. These deep craters severely deteriorated the surface quality.

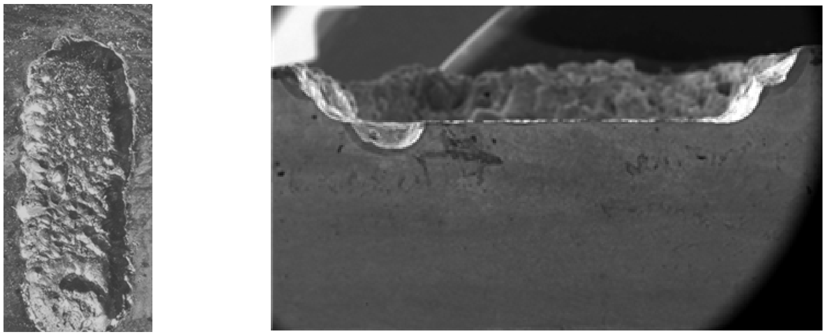
(a) (b)

Figure 2.11. Optical micrographs of quasi-explosion mode EDM surface with deep craters (a) top view and (b) cross-section view (i_e = 30 A, t_i = 12 μs, t_0 = 8 μs, u_{gap} = 60 V and u_i = 260 V)

2.6. Mechanism of High MRR in Oxygen-assisted Dry EDM

The high MRR in oxygen-assisted dry EDM is due to the rapid oxidation of ferrous metal stimulated by the high temperature in the EDM plasma channel. The occurrence of oxidation is inferred from the observation of dramatic increase of oxygen content on the surface machined by oxygen-assisted dry EDM. The detected oxygen increase is more than 10 times of the original value, which is discussed in Chapter 5.

The rapid oxidation generates heat assisting the material removal and can even promoting self-sustained oxidation or combustion (Emsley, 1998). The possible oxidation reactions for pure iron are:

$$4\ Fe(s) + 3\ O_2\ (g) \rightarrow 2\ Fe_2O_3\ (s) \tag{2.1}$$

$$3\ Fe(s) + 2\ O_2\ (g) \rightarrow Fe_3O_4\ (s) \tag{2.2}$$

Both of these are exothermic process. It gives out 820 kJ/mol heat, equivalent of 5.2 kJ heat with 1 g Fe_2O_3 produced, and gives out 1120 kJ/mol heat, equivalent of 4.8 kJ heat with 1g Fe_3O_4 produced (Latimer, 1952). During the dry EDM process, the production of Fe_3O_4 is considered the major process. Spray of sparks was observed ejecting from the machining region and solidified into black debris. The black debris is mainly composed of Fe_3O_4 based on the observation of several its attributes, including the magnetic property, which is uniquely possessed by Fe_3O_4 among iron oxides (FeO, Fe_2O_3 and Fe_3O_4) (Cornell and Schwertmann, 2004), the dark grey color (Fe_2O_3 is brown and FeO is black in color) and the high percentage of oxygen elements detected via the energy dispersive spectroscopy analysis. The extra heat generated by the oxidation assists the machining by melting workpiece material and/or stimulating rapid iron oxidation, i.e. iron combustion. In addition to the heat generation, the oxidation converts some iron directly into oxide which is easier to remove. In the oxidation, the iron does not go through the molten status. The iron oxides have loose structure and lower density than iron (Golladay et al., 2006), and tends to detach from the base material. Unlike molten iron, which tends to re-deposit to the machined surface or electrode, the oxide debris tends to detach easily.

In oxygen-assisted dry EDM, the level of oxidation can be used to explain the different discharge modes, normal, quasi-explosion and explosion modes, as observed by

Kunieda et al. (2003) and also in our experimental investigation. The machined surfaces of these three modes are shown in Figures 2.10, 2.11 and 2.8, respectively.

At the normal mode, the oxygen does not yield better machining performance as compared with using air for dry EDM. The MRR is less than 10 mm^3/min and the R_a is less than 6 μm. With low i_e ($\leq$ 25 A) and high t_0 ($\geq$ 10 μs), the discharge pulse energy is relatively low and high temperature cannot be maintained in the discharge gap. The rapid oxidation, which requires certain activation energy and high environmental temperature, cannot be stimulated in this case even though the discharge gap is filled with oxygen.

Under the quasi-explosion mode, the MRR (> 20mm^3/min) is increased considerably and the surface finish (R_a > 15 μm) deteriorates due to scattered deep craters, as shown in Figure 2.11. When the i_e is close to 30 A, and t_0 is between 4 and 15 μs, the rapidly recurring high energy discharge pulses provide the high temperature and high energy condition to simulate and maintain the iron oxidation. The iron oxidation generates heat, which can help sustain the oxidation process itself without the external power input. This self-sustaining iron oxidation is called iron combustion (Emsley, 1998). With the iron combustion, the material removal is continued even during the discharge interval when the discharge power input is cut off. In addition, higher temperature is thus expected in the discharge gap. High temperature can lower the breakdown strength of the dielectric medium (Coelho, 1979), and facilitates the discharge ignition when the discharge power is turned on. This explains the observation of no discharge ignition delay in the quasi-explosion mode. On the other hand, the high velocity gas flow flushes through the discharge gap and cools down the combustion location. It helps to constrain the iron combustion and maintain a controllable material removal in the quasi-explosion mode.

Further increase of i_e ($\geq$ 40 A) and decrease of t_0 ($\leq$ 2 μs) can ignite the explosion mode. The high discharge current helps to simulate the iron combustion and the short discharge interval allows the rapidly reoccurred simulation. The iron is thus ignited and the combustion sustains itself. The gas (oxygen) flow simply provides more fuel for the combustion. The process thus becomes uncontrollable with intensive heat damaging the electrode and melting too much work-material, which cannot be coagulated and flushed away by the flushing gas. Under the explosion mode, the workpiece surface is damaged and the electrode also experiences excessive wear, as shown in Figures 2.8.

2.7. Concluding Remarks

This study investigated the dry and near-dry EDM roughing processes targeting to achieve high MRR. The oxygen-assisted dry EDM demonstrated the capability to boost the MRR. The effects of external air jet, depth of cut and five discharge parameters were studied to improve the performance of oxygen-assisted dry EDM. Three discharge modes, normal, quasi-explosion, explosion, were observed. High i_e and low t_0 were found to be the key factors to stimulate the high MRR quasi-explosion mode. But the explosion mode, under which undesirable damage to the workpiece and electrode can occur, should be prevented by limiting the decrease of t_0.

The mechanism of high MRR in oxygen-assisted dry EDM was discussed. The exothermal iron combustion process induced by the high temperature and high proportion of oxygen during the electrical discharge was proposed as the catalytic factor.

CHAPTER 3

FINISH MACHINING BY DRY AND NEAR-DRY EDM MILLING

3.1. Introduction

This study explores the dry and near-dry EDM in finish machining to achieve an ultra fine surface finish and develops a process plan to integrate the roughing and finishing EDM processes.

To achieve ultra fine surface finish is a challenge for the EDM process because the EDM surface is composed of discharge craters overlapped on each other and is thus inherently rugged, as shown in Figure 3.1. Over the years, researchers have explored the super fine EDM finishing process. Two dominant technologies are (1) using ultra low discharge pulse energy (Luo et al., 1988; Luo and Chen, 1990; Egashira et al., 2006; Okada et al., 2006) and (2) implementing powder mixed dielectric (PMD) EDM (Narumiya et al., 1989; Mohri et al., 1991; Wong et al., 1998; Pecas and Henriques, 2003; Zhao et al., 2005). However, both methods have their limitations.

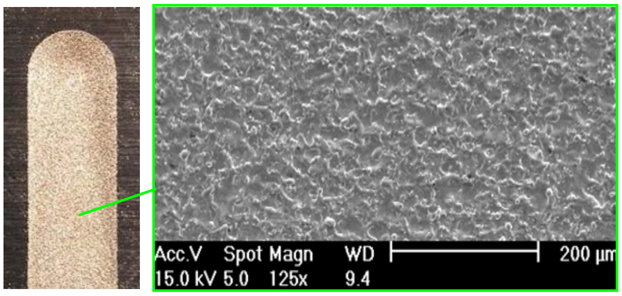

Figure 3.1. A typical EDM surface with medium finish quality, R_a = 1.2 μm.

Luo et al. (1988; 1990) demonstrated a super finished EDM surface with 0.04 μm R_a by lowering the discharge pulse energy through extremely short discharge duration, t_i, less than 0.2 μs. Egashira et al. (2006) applied the ultra-low discharge energy, less than 3 nJ, to conduct finish machining with the assistance of ultrasonic vibration. Okada et al. (2006) studied the radio-frequency plasma with 0.1 μs discharge duration to produce a surface roughness of 0.15 μm R_a on aluminum. The disadvantage of the low pulse energy method is the low material removal rate (MRR) and long machining cycle due to the small amount of material removal per discharge and the frequent abnormal discharges as a result of the narrow gap distance.

The PMD EDM has been recognized as a more practical finishing process to generate very fine surface finish at relatively high MRR (Mohri et al., 1985, 1987, 1991; Narumiya et al., 1989). Powders such as graphite, silicon and aluminum suspended in the dielectric help to stabilize the machining process at low pulse energy by increasing the discharge gap distance, decreasing the stray capacitance and dispersing the discharge pulses (Wong et al., 1998; Zhao et al., 2005). However, the use of powder increases the machining cost and the subsequent toxic disposal causes an environmental concern (Yeo et al., 1998; Pecas and Henriques, 2003). In production application, the powder suspended dielectric circulation system is also challenged by separating the machined debris from the useful powders and maintaining a constant powder concentration.

Dry and near-dry EDM has the potential for finishing operation. Kunieda et al. (2001) and Wang et al. (2004) applied the dry process to precision wire EDM finish cutting to improve the straightness and geometrical accuracy owing to the considerably reduced wire vibration due to the small disturbance force by gas flow. Kao et al. (2006) applied the near-dry process in wire EDM using water-air mixture and found its benefit of better machining stability and higher MRR than the wet EDM in finishing process. Also, using the gas or liquid-gas dielectric medium, the dielectric disposal of dry or near-dry EDM is cleaner than that of PMD EDM.

This research explores the dry and near-dry EDM milling as a finishing process and a mirror surface with 0.09 μm R_a is achieved by the near-dry EDM finish machining. Efforts are further applied to integrate the oxygen-assisted dry EDM roughing and near-dry EDM finishing processes by using the same copper tubular electrode. The integrated process is applied in flat surface milling to achieve a mirror surface on a DMD part.

In the following sections, the effects of dielectric fluid, electrode material and discharge parameters are first investigated and proper settings and directions are identified for the ultra fine finish machining. Efforts are then taken to improve the surface finish with the aid of different EDM power generator systems. The capability for near-dry EDM milling to achieve the ultra fine surface finish is finally demonstrated.

3.2. Experimental Setup and Design

3.2.1. Experimental Setup

Two EDM systems, EDM Solutions Vanguard EDM machine and Sodick AQ55L

EDM machine, are used in the finishing process investigation. The setup on the EDM Solutions machine is the same as that of the roughing process investigation in Chapter 2. The Sodick machine has an advanced EDM power generator with better electrode servo control and discharge regulation. A reference gauge is attached to the Sodick machine, as shown in Figure 3.2, to measure the electrode length such that the shortening of the electrode can be monitored and compensated.

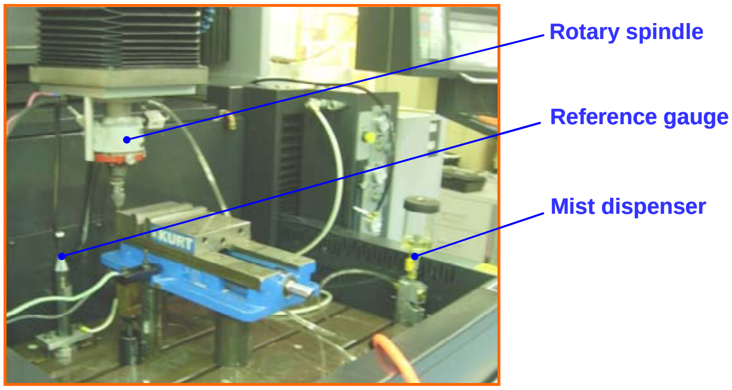

Figure 3.2. Dry and near-dry EDM milling setup on the Sodick EDM machine.

The same EDM milling configuration and dielectric dispensing system as in the previous chapter are applied. Air and nitrogen are tested as the medium for dry EDM and they are mixed with water and kerosene as the liquid-gas mixture medium for the near-dry EDM. Three common electrode materials, graphite (C), copper infiltrated graphite (CuC) and copper (Cu) are compared. For all finishing process experiments, negative polarity, i.e., electrode as cathode, is used considering the lower cathode wear at low discharge pulse duration (Arunachalam, 1995) and smoother discharge craters on anode (Tamura and Kobayashi, 2004).

In addition to the Talysurf Intra profilometer and Ohaus GA110 electronic scale used in the previous investigation, an Agilent Infiniium 54833A digital oscilloscope is used to monitor the current and voltage waveforms and an Olympus PME3 optical microscope is used to inspect the machined surface and discharge craters.

3.2.2. Experimental Procedures

The investigation of dry and near-dry EDM milling finishing processes is carried out in three steps.

First, effects of different dielectric fluids and electrode materials are characterized. The statistical analysis using independent two-sample *t*-test (Montgomery, 2005) is applied to test the significance of those effects. The proper combination of dielectric fluid and electrode material is identified for the EDM finishing process.

Second, The DOE of 2^{5-1} fractional factorial design with four center points, as listed in Table 3.1, is applied to systematically study the effect of all the discharge parameters (i_e, t_i, u_{gap}, t_0 and u_i) on the machining performance. As discussed in previous Chapter, the experimental design is capable of detecting the effect of main factors and second order interactions. The DOE can provide a guideline to adjust the discharge parameter for better surface finish.

Third, the process improvement is conducted according to the DOE projection. Modification of the EDM generator (of the EDM Solutions machine) and implementation of the advanced generator (of the Sodick EDM machine) are carried to attain the ideal discharge waveform for the target surface finish, 0.1 μm R_a. In the EDM fine finishing experiments, four additional parameters, tool wear ratio (TWR), R_z, discharge gap distance and actual depth of cut (ADOC), are appended for the machining performance evaluation and the machining process planning. The TWR is defined as the volume of tool wear divided by the volume of work-material removed. The R_z is the average peak-to-valley height of the surface profile. The discharge gap distance defines the averaged gap size between the electrode and workpiece during EDM. The ADOC is the actual cutting depth on a machined surface. It is different from the quantity of depth of cut (DOC), which defines the servo position of the electrode during the machining, because the discharge gap distance causes the ADOC larger than the DOC while the tool wear reduces the ADOC. In the experiments, the ADOC is attained by measuring the profile of the machined slot using a profilometer. The gap distance is calculated as: gap distance = ADOC – DOC + electrode shortening length. The electrode shortening length, i.e., tool wear, is measured using a reference gauge attached to the machine.

Table 3.1. DOE design for finishing process

Run	t_i (μs)	i_e (A)	u_i (V)	u_{gap} (V)	t_0 (μs)	Run	t_i (μs)	i_e (A)	u_i (V)	u_{gap} (V)	t_0 (μs)
1	4	2	160	80	12	11	4	6	260	80	4
2	8	2	160	40	4	12	8	6	260	40	12
3	4	6	160	40	12	13	4	2	160	40	12
4	8	6	160	80	4	14	8	2	160	80	4
5	4	2	260	80	4	15	4	6	160	80	12
6	8	2	260	40	12	16	8	6	160	40	4
7	4	6	260	40	4	17	6	4	210	60	8
8	8	6	260	80	12	18	6	4	210	60	8
9	4	2	260	40	4	19	6	4	210	60	8
10	8	2	260	80	12	20	6	4	210	60	8

The last part of the study demonstrates the integration of dry EDM roughing and near-dry EDM finishing processes to achieve the ultra fine finish machining on a DMD part. The process planning is carried out to select proper and economic machining steps.

3.3. Effect of Dielectric Media and Electrode Materials

3.3.1. Dielectric Media

Figure 3.3 compares the dry, near-dry and wet EDM using different dielectric media at the low discharge energy level. The dry EDM is obviously not suitable for the finishing process. It yields the roughest surface and the MRR is low. The gas medium has low flushing capability to blow away the machining debris. The molten material tends to reattach on the machined surface leaving a rugged surface. The debris reattachment also deteriorates the discharge gap condition and reduces the MRR.

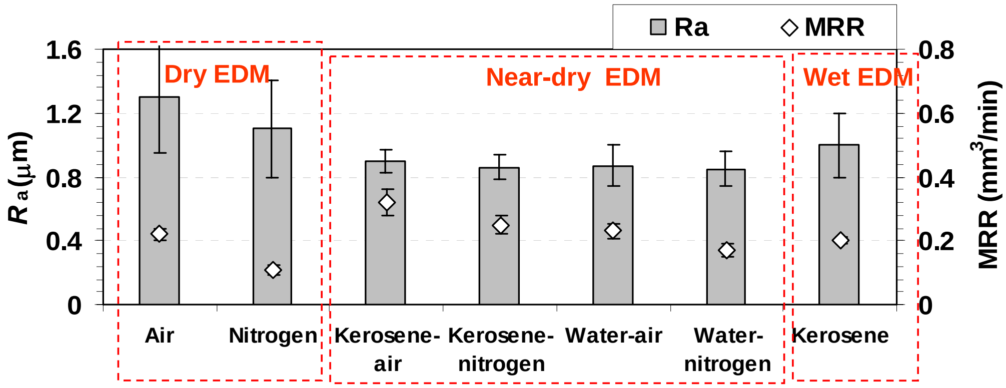

Figure 3.3. MRR and R_a results of different dielectric fluids for copper and graphite electrode materials at low discharge energy input (i_e = 2 A, t_i = 4 μs, t_0 = 8 μs, u_{gap} = 60 V and u_i = 200 V, copper infiltrated graphite electrode, EDM Solutions machine).

According to the statistical significance analysis, the near-dry EDM outperformed the wet EDM in better surface finish with a 60% confidence level and the MRR is also higher if the kerosene based liquid-gas mixture is used as the dielectric fluid (91% confidence level). In general, the surface machined by near-dry EDM is of shallower discharge craters and results in better surface finish. The reason is related to the electrical, mechanical and thermal properties of the dielectric fluid, which influences the discharge channel formation and material expulsion. In Chapter 4, a EDM model will be used to discuss the difference between the near-dry and wet EDM performance considering the mechanical and thermal properties of their dielectric fluids. In addition, the higher MRR of the near-dry EDM process is attributed to the more stable machining process. At low discharge energy, the wet EDM is observed to have frequent electrode servo retraction indicating inappropriate discharge gap condition. The liquid-gas mixture in the near-dry EDM is of lower dielectric strength. It is easier for discharge to initiate and form stable consecutive discharges than wet EDM. This effect is especially significant at the low discharge energy case, where very small gap distance (< 30μm) is needed for discharge initiation. The smaller discharge gap distance in wet EDM makes the discharge condition mores sensitive to floating debris in the gap. The debris can cause detrimental discharges, like arcing or short circuit, by bridging the workpiece and electrode. Then the electrode has to be retracted to recondition the discharge gap. The unstable discharge condition can occur repeated especially if the electrode servo system is of low response frequency. The near-dry EDM, however, does not address that high requirement on the servo system at the low discharge energy.

In the near-dry EDM, the performance of water based and kerosene based liquid-gas mixture is further compared. As seen from Figure 3.3, the surface finish is about the same, between 0.85 to 0.9 μm R_a, for the four near-dry EDM dielectric fluids. However, severe electrolysis corrosion and deteriorated surface quality is observed on the surface machined with water based liquid-gas mixture, as in Figure 3.4. The individual discharge crater created by the water based liquid-gas mixture is finer than those of kerosene based liquid-gas mixture, but the electrolysis causes the blackened and rugged surface. Even though the nitrogen medium can prevent the water electrolysis by isolating the oxygen content to some extent, the water electrolysis is still provoked due to the more frequent arcing and short circuiting at the low pulse energy case. It indicates that the electrolysis is an obstacle to implement the water based liquid-gas mixture for super finishing near-dry EDM.

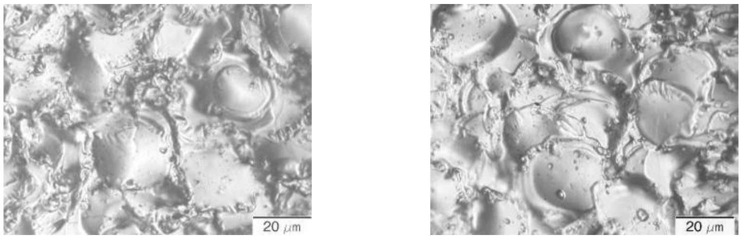

Kerosene-air mixture Kerosene-nitrogen mixture

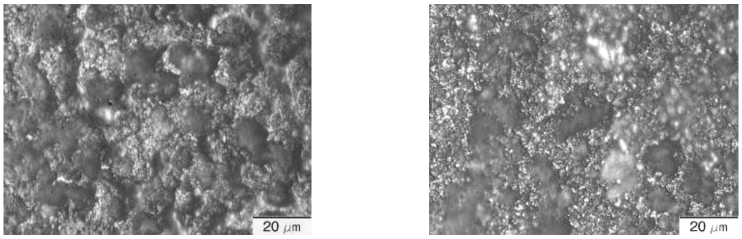

Water-air mixture Water-nitrogen mixture

(b)

Figure 3.4. Comparison of dielectric fluids in near-dry EDM milling, (a) surface roughness and MRR, and (b) micrographs of the discharge craters (i_e = 2 A, t_i = 4 μs, t_0 = 8 μs, u_{gap} = 45 V and u_i = 100 V, copper infiltrated graphite electrode).

The kerosene based liquid-gas mixture exhibits the advantages of shiny surface, high MRR and comparable surface finish. Comparing the gas media in the mixture, air obviously enhances the MRR, as the oxygen content in the air generates more heat for material removal through an exothermic reaction (Yan et al., 2005), while its surface is slightly rougher than that of nitrogen. The nitrogen medium, which is used for preventing oxidation or electrolysis, does not contribute much to improve the surface finish, since little oxidation or electrolysis occurs when kerosene is used. Considering the high MRR and easy availability of air, kerosene-air mixture is chosen as the dielectric fluid for further investigation.

3.3.2. Electrode Materials

The comparison of electrode materials is first conducted among copper, graphite and copper infiltrated graphite on the EDM Solutions machine. The test results are summarised in Figure 3.5.

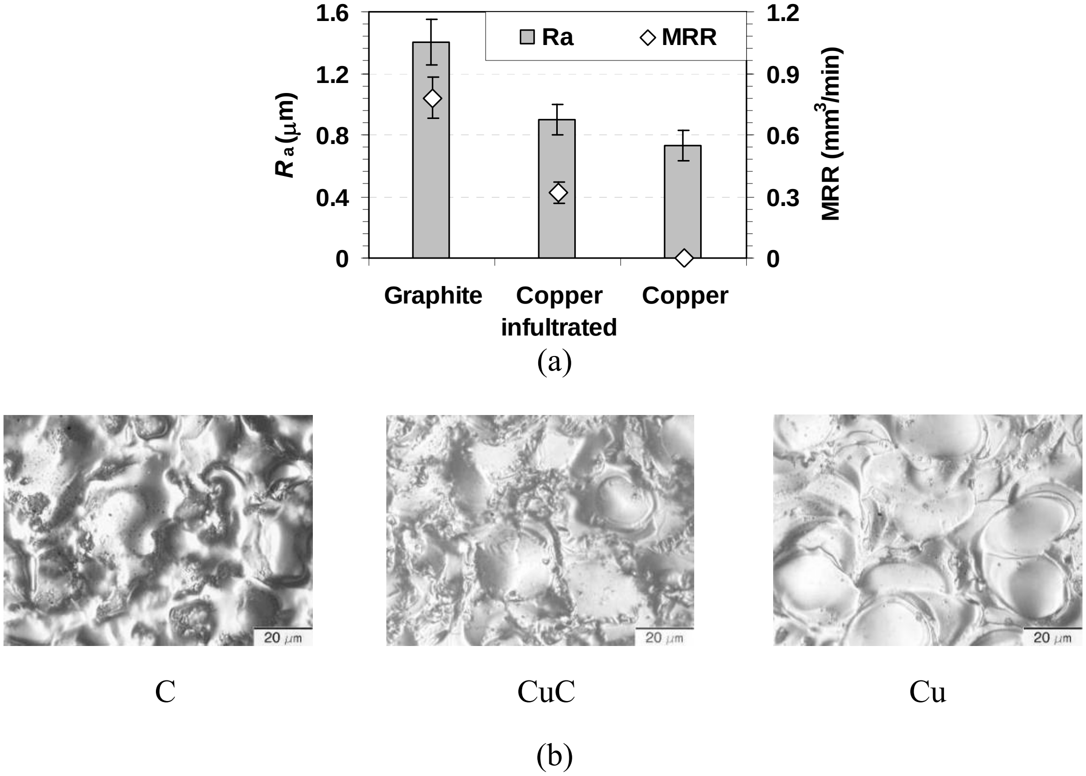

(a)

C CuC Cu

(b)

Figure 3.5. Comparison of different electrode materials in near-dry EDM, (a) surface roughness and MRR, and (b) micrographs of the discharge craters (i_e = 2 A, t_i = 4 μs, t_0 = 8 μs, u_{gap} = 45 V and u_i = 100 V, kerosene-air mixture, EDM Solutions machine)

Among the three electrode materials, graphite has the highest MRR but its surface finish is the worst. As shown in the first picture of Figure 3.5(b), the machining marks by graphite electrode are observed as deep craters with deposition of overflowed molten material on the crest. This indicates that a large amount of material is melted during the discharge but the expulsion force is not strong enough to eject all the molten material. Such discharge pulse is close to the status of arcing, which is considered induced by the graphite powders flaked from the electrode. The graphite powder can be aligned in the electric field to bridge the electrode and workpiece to induce arcing. In arcing, the material melting is significant but material expulsion is not powerful.

The copper electrode generates a clean surface, as in the third picture of Figure 3.5(b), but the MRR is unacceptably low on the EDM Solutions machine. At low discharge pulse energy, the gap distance between the electrode and workpiece is small. It requires a servo system with high sensitivity and quick response to maintain the proper gap distance. Otherwise, the system will switch between the open and short circuit and thus lower the MRR significantly. When machining using the copper electrode, this situation occurs frequently on the EDM Solutions machine.

The copper infiltrated graphite electrode takes the advantages of both materials, as shown in the second picture of Figure 3.5(b). The graphite or carbon content, once dispersed into the discharge gap at a small amount, can assist the machining process by improving the discharge transitivity (Luo, 1997) for evenly distributed discharges (Yang and Cao, 2007). Thus, a stable machining and moderate MRR can be achieved. In the meanwhile, the copper content increases the thermal conductivity of the electrode. It helps reduce the thermal impact on the electrode during the discharge. Copper also has high fracture toughness to hold the electrode material together in near-dry EDM. The flaking of graphite powder can thus be prevented, which helps reduce the occurrence of arcing as in the graphite electrode case. Smooth discharge craters can be generated.

The second electrode comparison is conducted between the copper infiltrated graphite electrode (CuC) and copper electrode (Cu) using the Sodick EDM machine. The Sodick machine uses linear motor driven stage with much high dynamic response than the ball screw driven stage of the EDM Solutions machine. Hence, it is able to achieve fairly stable machining using copper electrode. Figure 3.6 shows the performance of the two electrodes. As is expected, the copper electrode provides better surface finish in terms of both R_a and R_z values. It also has much lower TWR even though the MRR is a little bit lower.

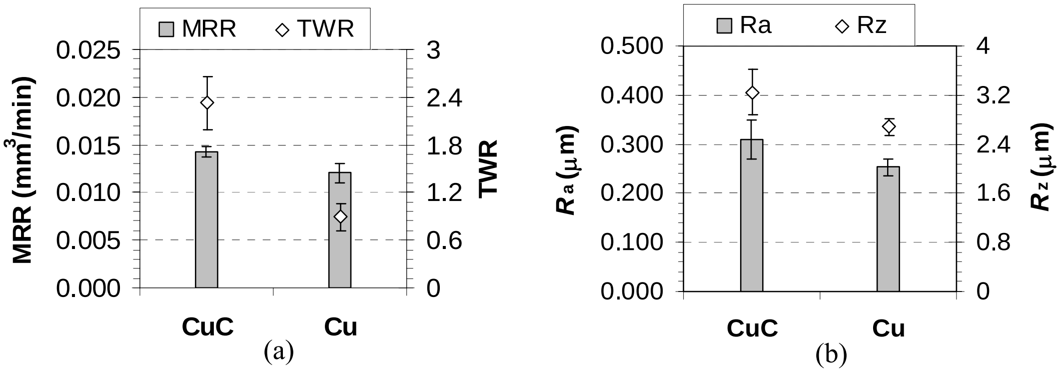

Figure 3.6. Comparison of copper (Cu) and copper infiltrated graphite electrodes (CuC) (i_e = 2 A, t_i = 0.5 μs, t_0 = 10 μs, and u_i = 210 V, kerosene-air mixture, Sodick machine).

As seen in Figure 3.7, the surface machined by copper electrode is fairly clean with distinguishable individual discharge craters while the copper infiltrated graphite electrode generated surface is obliterated by molten droplets and attached black particles.

The graphite powder detached from its base structure helps improve the MRR a bit but deteriorates the surface finish quality and is the reason for the slightly higher tool electrode wear. In this case, the copper infiltrated graphite has no advantage for the final finish machining.

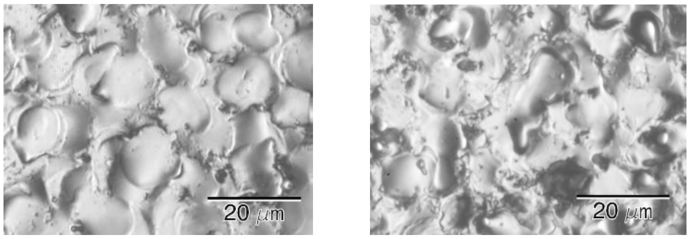

Copper Copper infiltrated graphite

Figure 3.7. Micrographs of the surface machined by copper and copper infiltrated graphite electrodes (i_e = 2 A, t_i = 0.5 μs, t_0 = 10 μs, and u_i = 210 V, kerosene-air mixture, Sodick machine)

As a short summary, the graphite electrode is not ideal for the finishing process. The copper electrode is capable to provide the best surface finish among the test materials and is selected in the ultra-fine finishing process using the Sodick EDM machine. But the copper electrode has stringent requirement on the electrode servo system at low discharge energy. Without the advanced servo control, it is hard to maintain a stable machining. In this case, the copper infiltrated graphite electrode can be a cost effective substitution. It yields stable machining and moderate surface finish without much stress on the machine servo system.

3.4. Effect of Discharge Parameters

The effect of discharge parameter is investigated with the aid of DOE. The MRR and surface roughness results of the DOE are summarized in Table 3.2. According to the ANOVA, the significant terms influencing the MRR are the main factors, i_e and t_i, and second order interaction, t_0*t_i.

Table 3.2. MRR and R_a results for finishing process

Run	1	2	3	4	5	6	7	8	9	10
MRR (mm^3/min)	0.075	0.145	0.161	0.157	0.129	0.161	0.168	0.206	0.151	0.152
R_a (μm)	0.80	1.34	1.03	1.64	0.85	1.24	1.08	1.52	1.76	1.08
Run	11	12	13	14	15	16	17	18	19	20
MRR (mm^3/min)	0.121	0.125	0.176	0.145	0.147	0.120	0.126	0.129	0.135	0.136
R_a (μm)	1.45	0.86	1.50	0.93	1.18	0.86	1.12	1.17	1.22	1.30

The response surfaces of MRR versus the significant factors, t_i, i_e and t_0, are shown in Figure 3.8(a). High i_e and t_i increases MRR. The effect of t_0 varies with the level of t_i. At high t_i, the MRR decreases when decreasing t_0. Higher t_i generates more debris and requires longer t_0 to recondition the discharge gap. Otherwise, with reduced t_0, arcing tends to occur due to the degraded discharge gap condition, the electrode frequently retracts, and the MRR decreases. The degraded discharge gap condition also deteriorated the surface finish. At low t_i, less debris was generated with lower discharge energy. Less time is required to recondition the discharge gap. In this case, shorter t_0 increased the discharge frequency and therefore increased the MRR.

It is found that the main factors, i_e, t_i, t_0, and second order interaction, t_0*t_i, have significant effects on surface finish. The projected surfaces of surface roughness vs. t_i, i_e, and t_0 are shown in Figure 3.8(b). The third plot of the figure shows that the surface finish can be efficiently improved by decreasing i_e and t_i. Similar to the MRR results, the effect of t_0 varies with the level of t_i. At high t_i, the surface finish deteriorates with decreasing t_0 due to the arcing in degraded discharge gap condition. Under low t_i, a long t_0 was not required to maintain a good discharge gap condition. The surface finish is only related to the pulse discharge energy.

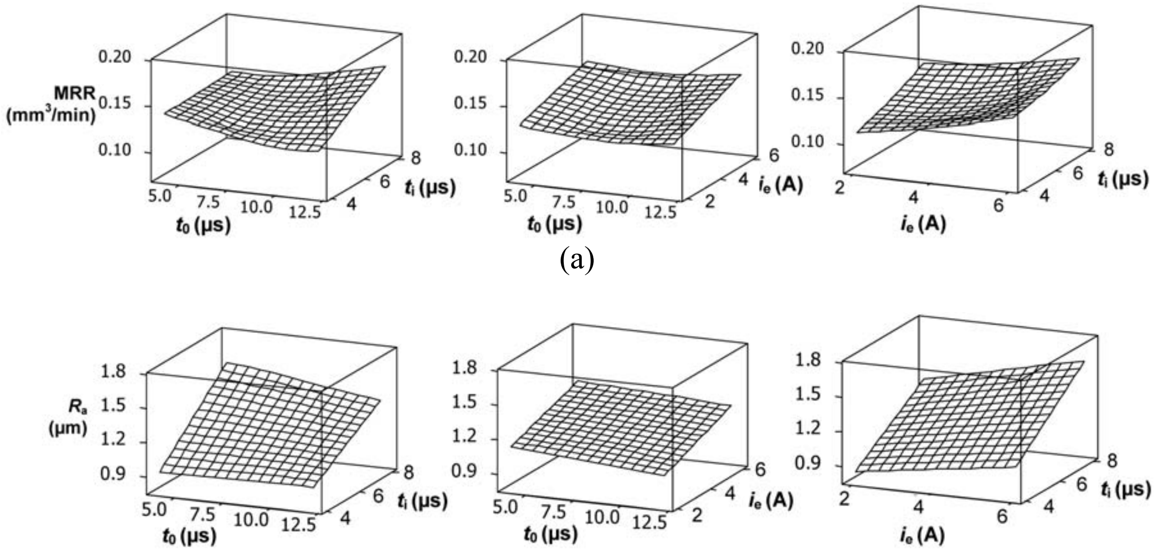

(a)

(b)

Figure 3.8. Response surfaces of (a) MRR and (b) R_a versus t_i and t_0, i_e and t_0, and i_e and t_i for finishing EDM

From the response surface, a linear decreasing trend of R_a is observed when reducing i_e and t_i and raising t_0. The linear trend indicates that the current machining conditions are still far from the minimum R_a region and the potential for further improving the surface finish is large. In addition, the effect of i_e and t_i can be described by a unified parameter, discharge pulse energy, E_d, which can be expressed by

$$E_d = \int_0^{t_i} i_e(t)u_e(t)dt \cong \sum_{t=0}^{t_i} i_e(t)u_e(t)\Delta t \tag{3.1}$$

where u_e is the discharge voltage, which depends on the discharge channel property and is not directly controlled by the discharge parameters. This is in accordance with the perception that lower pulse energy removes less material per discharge, leaves shallower discharge crater and yields smoother surface. To achieve better surface finish, efforts are made to reduce the discharge pulse energy by lowering i_e and t_i.

3.5. Process Improvement

Two attempts are made to shorten the discharge duration and lower the discharge current for the finishing process improvement. In the first attempt, modification of EDM Solutions machine's generator, of which the original minimal i_e and t_i are high, is conducted. The EDM generator modification is of much lower cost than the second attempt, implementing the advanced EDM generator of the Sodick EDM machine. The effect of these two attempts will be discussed in the following sections.

3.5.1. EDM Generator Modification for Reduced Discharge Current

The EDM generator modification is carried out in two directions, reducing discharge duration, t_i, and reducing discharge current, i_e.

The practice of reducing t_i is not effective. A trigger signal modulator is applied attempting to reduce the t_i. Since the t_i and t_0 are controlled by the on and off time of the trigger signal, as shown in Figure 3.9, efforts are made on the trigger circuit to reduce the on time duration, T_{on}. However, when the trigger signal with T_{on} lower than 4 μs is applied, highly distorted waveform with the drop in amplitude is observed. It means the driving frequency of the input signal is beyond the frequency response of the power supply. To output shortened t_i, further modification is needed on the power supply to reduce its system inertia. But it is beyond our current capability.

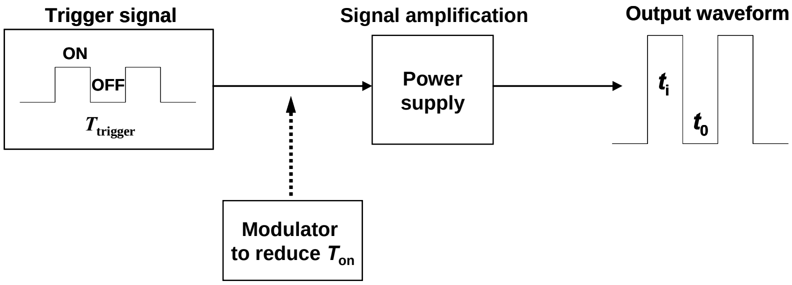

Figure 3.9. Schematics for controlling and shortening t_i.

The scheme to reduce the discharge current, i_e, is shown in Figure 3.10(a). An external resistor, R, which can dissipate energy and reduce the current passing through, is inserted to the discharge loop. Its effect on the discharge current and voltage waveforms is shown in Figure 3.10(b). With the insertion of a 10 kΩ power resistor the peak discharge current is effectively reduced from 4 to 1 A. However, the open circuit voltage and discharge voltage is slightly altered by the insertion of the power resistor. The open circuit voltage, u_0, drops from 80V to 60V and discharge voltage, u_e, rises from 20V to 25V. The alternation of the voltage, which can result from the measurement error or leakage current, is not an expected output and cannot be explained with concrete support. No detailed investigation is conducted since neither of them has been identified as the significant process parameters by the DOE analysis in Section 3.4. To accommodate the effect of varying discharge voltage, the discharge pulse energy, E_d, as calculated by Equation 3.1, is used to characterize the surface finish improvement.

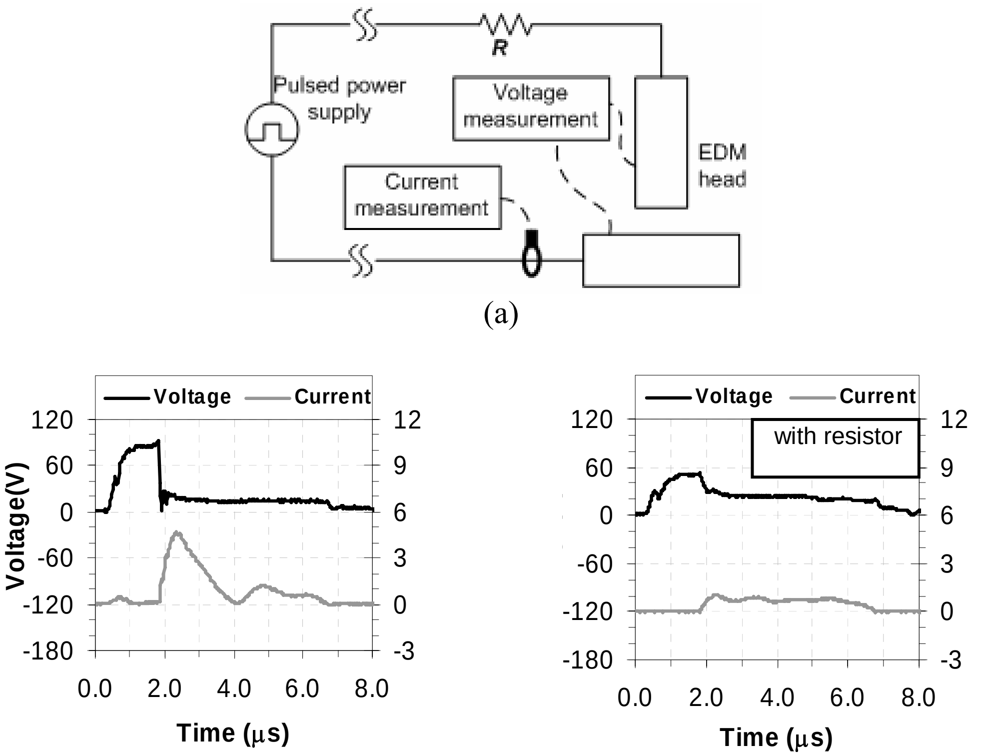

(a)

Without external resistor

With external resistor

(b)

Figure 3.10. Modification of EDM generator to reduce discharge current, (a) circuit schematic, and (b) effect on the output discharge waveform (EDM Solutions)

Figure 3.11 shows the improvement of surface finish with the reduction of E_d and a surface finish of 0.32 μm R_a is demonstrated. As shown in the micrographs, the small E_d reduces the depth of the discharge crater and the molten material overflow. The best surface finish achieved is 0.32 μm R_a with the pulse energy of 100 μJ by applying a 50 kΩ resistor in the discharge circuit. Further increase of the resistance (up to 20 mΩ) does not help improve the surface finish significantly and no significant material removal is induced. The advancement is restrained due to the limitation of the equipment with 4 μs minimum discharge duration. The mismatch between the small discharge current and the relatively long discharge duration makes is not desired. In general, discharge duration equal to or lower than 1 μs is needed in the finishing EDM (Luo and Chen, 1990; Pecas and Henriques, 2003).

Certain success has been achieved by modifying the EDM generator. The discharge current is reduced at a very low cost and the surface roughness has been reduced more than 50%. But to achieve the ultimate surface finish, both low discharge current and discharge duration are needed and the effect is presented in the next section.

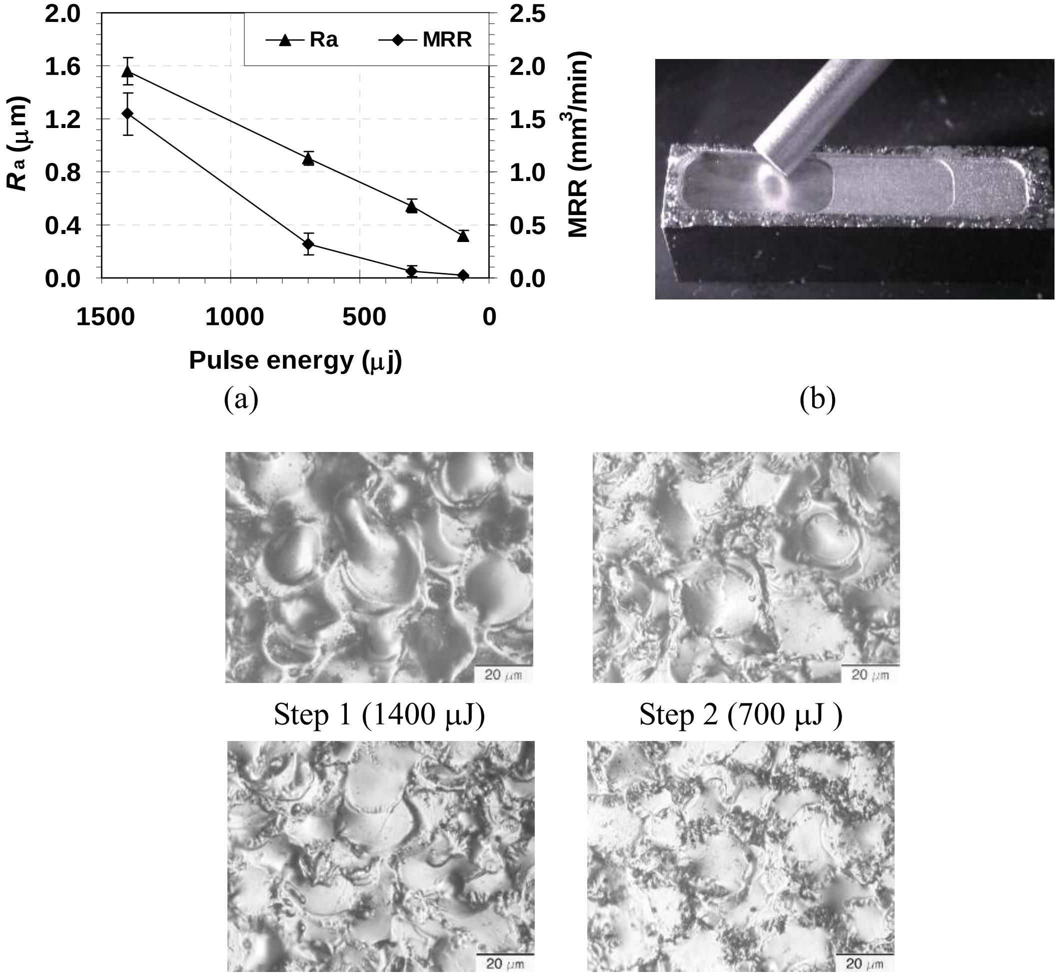

(a) (b)

Step 1 (1400 μJ) Step 2 (700 μJ)

Step 3 (300 μJ) Step 4 (100 μJ)

(c)

Figure 3.11. Effect of improving surface finish with reduced discharge energy (a) Surface roughness and MRR, (b) illustration of the machined surface, and (c) optical micrographs of the discharge craters at different finishing steps. (EDM Solutions)

3.5.2. Advanced EDM Generator with Reduced Discharge Current and Duration

The Sodick EDM machine is used to further exploit the near-dry EDM finishing capacity. Its generator for ultra finishing is capable to provide t_i less than 1 µs and i_e lower than 1 A. However, the specific generator works differently from the conventional approach that the machining performance is tuned by adjusting the discharge parameters, such as i_e, t_i, and t_0. Instead, the discharge waveform is selected by specifying the discharge condition. Nine discharge conditions, marked as F1 to F9 in Table 3.3, are evaluated for the near-dry EDM finishing.

Table 3.3. Parameters of the nine EDM finishing discharge conditions.

Discharge condition	i_e (A)	t_i (µs)	u_e (V)	t_0 (µs)	u_i (V)
F1	0.7	0.5	28	10	140
F2	0.7	1.0	28	10	140
F3	1.4	0.75	28	10	140
F4	2.0	0.2	25	10	210
F5	1.8	0.5	28	10	140
F6	2.2	0.2	25	10	210
F7	1.5	1.0	28	10	210
F8	1.5	0.75	35	10	210
F9	3	0.5	35	10	210

Figure 3.12 shows the machining performance, including R_a, R_z, MRR, TWR and discharge gap distance, of the nine near-dry EDM setups, F1 to F9, numbered in ascending order of their R_a, varying from 0.09 to 0.4 µm. The best surface finish of 0.09 µm R_a is achieved using the F1 setup with $i_e = 0.7$ A, $t_i = 0.5$ µs and $E_d = 10$ µJ.

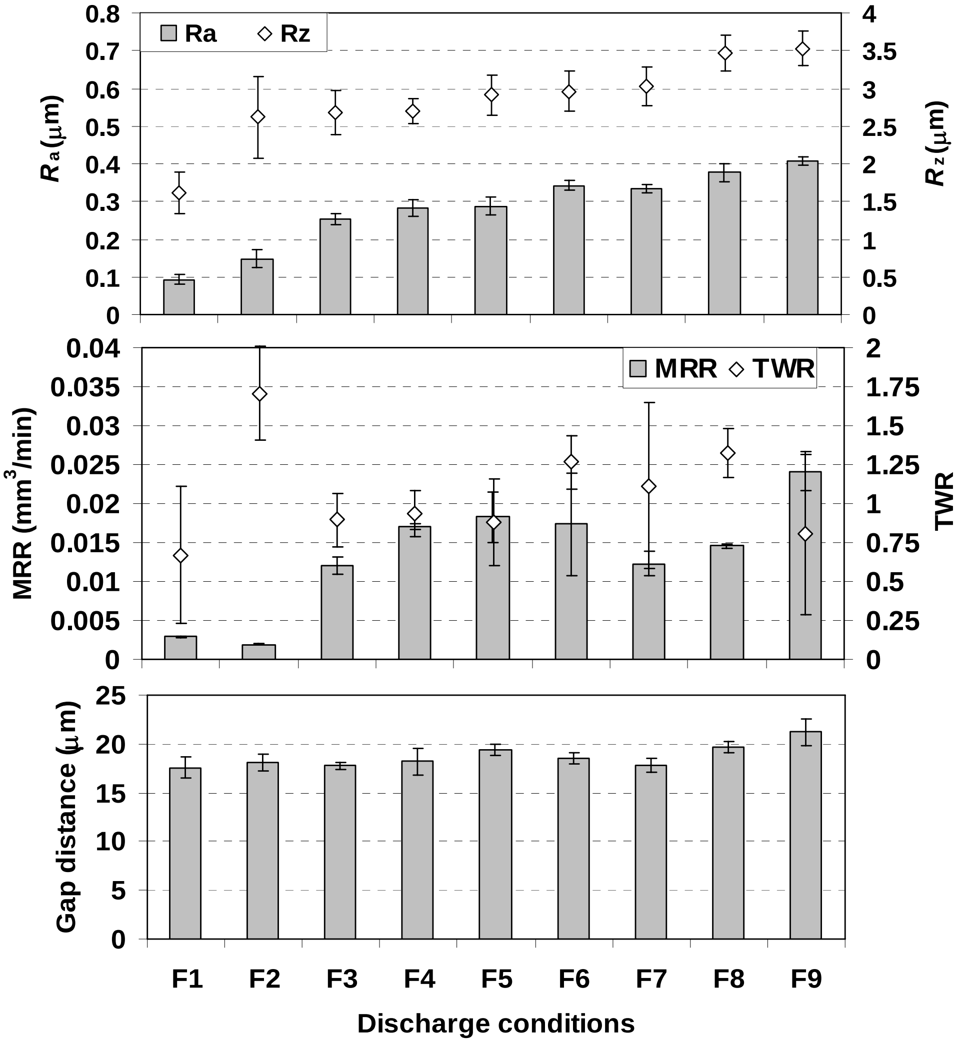

Figure 3.12. Performance of near-dry EDM using kerosene-air mixture under different discharge conditions.

In addition to the discharge energy, the EDM fine finishing process is observed sensitive to two other factors, which cannot be explained thoroughly but their effects are worthwhile to notify. The first factor is the carbon content decomposed from the kerosene oil. In finishing EDM, a glossy surface can usually be expected if the surface is covered by a uniform layer of carbon sludge. The surface will be rougher if the carbon sludge is not well retained during the machining. The phenomenon was also observed by

Yang and Cao (2007). The carbon sludge is considered to distribute the discharge energy and flatten the discharge crater. But there is still no well established and in-depth explanation for the mechanism, which expects further investigation. The second factor is that the machined surface finish can be improved by connecting a voltage probe in parallel to the discharge circuit. The inclusion of the voltage probe could have changed the impedance of the circuit and reduced the discharge energy. Even though the voltage probe should have been built to cause the minimal influence on the inspection circuit, the impedance of the discharge circuit can be very sensitive to the change of the circuitry components and inclusion of the voltage probe can influence in a positive way to lower the discharge energy. Future investigation is recommended to study the effect of the voltage probe on the discharge circuit impedance and find a way to improve the EDM surface finish.

Associated with the fine surface finish, the MRR is found very low in finishing EDM. In Figure 3.12, the MRR of F1 setup is only about 0.003 mm^3/min. If without proper process planning, excessive machining time can be used for F1 to finish even a nominal surface area. For example, it takes about 80 min to complete the slot of the 5 mm long and 11 μm depth shown in Figure 3.13(a).

Large TWR is associated with the fine finishing process as shown in Figure 3.12. For setups F1 to F9, the TWR varies from 0.7 to 1.3 for all cases except F2, which yields very high TWR, 1.75. The high TWR is inherent in finishing EDM with short t_i.

The discharge gap distance varies from around 18 to 21 μm from setups F1 to F9. This gap distance is relatively small as compared to those (30 ~ 100 μm) generated at higher discharge energy (Kunieda et al., 2005).

The low MRR and large TWR are two challenges to implement the finishing EDM for large area machining. In Sections 3.6.2 and 3.6.3, the process planning will be discussed to reduce the total machining time and compensate the tool wear for the flat surface machining.

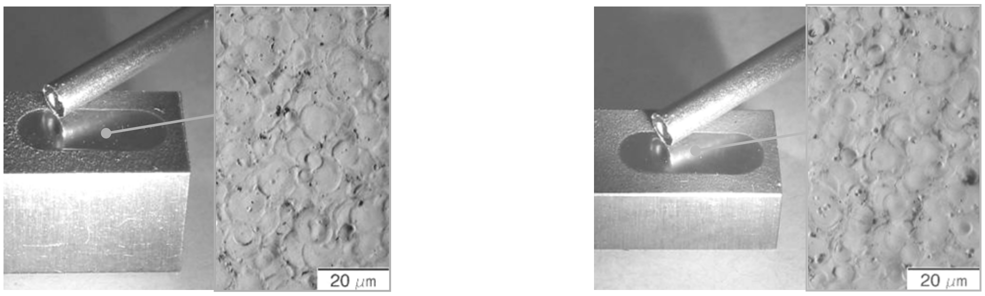

(a) (b)

Figure 3.13. EDM finished with R_a = 0.09 μm (a) final-finished by F1 with 11 μm ADOC, 80 min machining time, and (b) semi-finished by F5 with 10 μm ADOC F1 and final-finished by F1 with 3 μm ADOC, 22 min total machining time.

3.6. Integration of EDM Roughing and Finishing Processes

Integration of the oxygen-assisted dry EDM roughing and near-dry EDM finishing is carried out on the Sodick machine. The integrated process using the same copper electrode is applied to finish a flat surface on a DMD part. The process planning is conducted to select proper and economic machining steps.

3.6.1. Roughing Process Planning

As found for the oxygen-assisted dry EDM in Chapter 2, the three discharge modes, explosion, quasi-explosion and normal, represents three levels of machining performance of the process. Figure 3.14 shows the performance of the representative discharge conditions with the Sodick EDM machine. The process parameters of R1 to R7 setups are listed in Table 3.4.

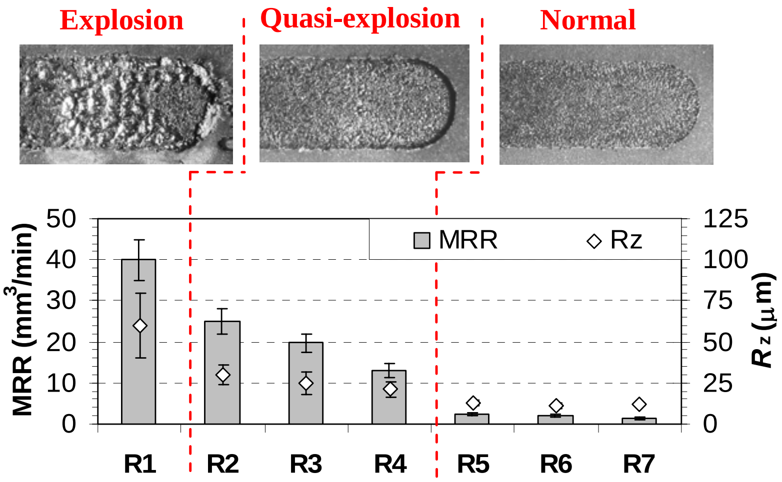

Figure 3.14. Performance of oxygen-assisted dry EDM under selected discharge conditions.

Table 3.4. Discharge parameters of selected oxygen-assisted dry EDM conditions.

Discharge condition	i_e (A)	t_i (μs)	u_e (V)	t_0 (μs)	u_i (V)
R1	40	5	25	1	210
R2	40	5	25	2	210
R3	40	4	25	4	210
R4	40	4	25	8	210
R5	25	5	25	10	210
R6	20	4	25	8	210
R7	15	2	25	4	210

The explosion mode is not desirable for the roughing process as it generates violent material removal such that the machined surface is ruined and the electrode experiences excessive wear. The quasi-explosion mode is ideal for the roughing process with high MRR and nearly zero tool wear even though the surface finish is rough. At the normal mode, the oxygen-assisted dry EDM still has advantage over wet or near-dry EDM in much lower tool wear even though their MRR and surface finish are comparable. Also, the 15 μm R_z from the normal mode is found as the limit of the surface roughness that oxygen-assisted dry EDM can achieve at the current setup.

Therefore, two machining steps are planned in the roughing process. R2, which as the highest MRR in the quasi-explosion mode, operates in the first step roughing to remove most of the redundant material and R3, which has the highest MRR in the normal mode, operates in the second step roughing to flatten the surface.

3.6.2. Finishing Process Planning

The process is planned to minimize the material removal, equivalently, the ADOC, for the final finish machining. It is because the F1 setup, which will be the final finishing step to achieve the 0.1 μm R_a surface finish requirement, has fairly low MRR. Any unnecessary material removal at this step will increase the total machining time significantly. The selection of the semi finishing process is thus critical because it determines the surface finish prior to F1. The ADOC of F1 should be selected according to the semi-finished surface quality so as to ensure the complete removal of the rough surface features from the prior machining. To find the minimum ADOC needed, the investigation is carried out as follows.

Two sets of experiments are conducted to use F1 to finish the surfaces semi-finished by F3 and F9 setups in each experiment. F3 and F9 are selected as the semi-finishing condition because they generate the roughest and finest surfaces (of the highest and lowest R_z values), respectively, among F3 to F9 setups in Table 3.3 and can thus represent two extreme cases in the selection of semi-finishing process prior to F1. When applying F1 to finish the two semi-finished surfaces, the DOC is incremented by 1 μm (but the ADOC varies due to the discharge gap and tool wear) for each cycle of machining. The surface finish after each cycle is measured to track its improvement with the increase of ADOC. Three cycles with 0.9, 1.7 and 2.5 μm ADOC are conducted to fully finish the F3 generated surface and five cycles with 0.7, 1.5, 2.3, 3.1 and 3.7 μm ADOC are conducted to fully finish the F9 generated surface.

As seen in Figure 3.15(a), the F3 semi-finished surface has R_z of 2.6 μm. As the ADOC of F1 increases, the surface finish improves until the ADOC reaches 2.5 μm, which is about the R_z of original F3 finished surface, and the best R_a value is 0.09 μm. It reaches F1 finishing capability, 0.09 μm R_a (Figure 3.12). For F9 semi-finished surface with 3.6 μm R_z, as in Figure 3.15(b), a 3.7 μm ADOC is needed to make the F1 final-finished surface reach 0.09 μm R_a. The good match between the R_z of the semi-finished surface and the minimal ADOC for F1 to achieve the fully finished surface indicates the criterion to determine the minimal ADOC for the F1 final finishing: the minimal ADOC should be at least equal to the R_z of the prior surface.

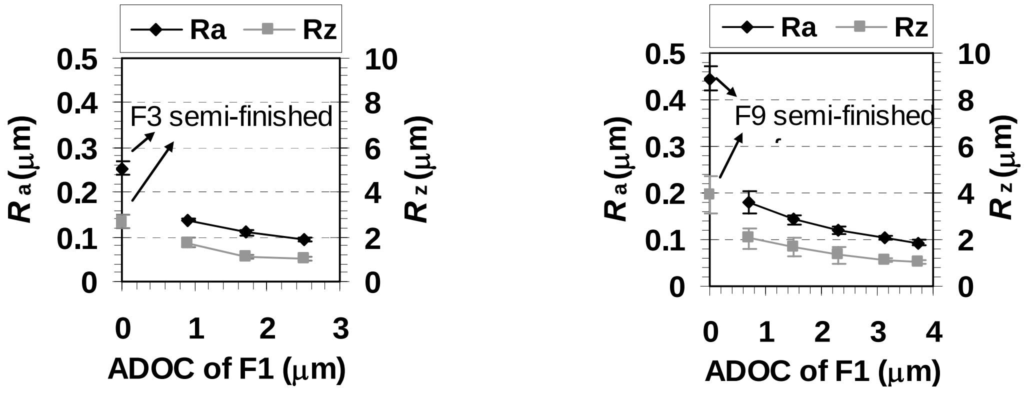

(a) (b)

Figure 3.15. Effects of DOC in F1 finishing on surfaces semi-finished by (a) F3, and (b) F9.

With that, the selection of the semi-finishing setup can be carried out by calculating and comparing the total machining time of combined semi and final finish machining with the aid of the MRR and R_z information in Figure 3.12. The comparison and selection are carried out among F3, F4, F5 and F9 setups in Table 3.3. F6, F7 and F8 are excluded from consideration due to their rough surface and low MRR than those of F5. Since the total machining time can vary with the size of machining area, two sets of estimation are conducted. The first one is based on a 5 mm stroke machining, as in Figure 3.13, and the other one is based on a nearly 9 mm × 9 mm square surface as in Table 3.5 and Figure 3.17. For both estimations, a 10 µm ADOC is assumed for the for the semi-finishing process and the ADOC for the final-finishing process is set equal to the R_z of the semi-finished surface (Figure 3.12). The machining time can be estimated based on the geometric calculation of the volume of material removal and the MRR in Figure 3.12.

Figure 3.16 shows the estimation of the total machining time with different semi-finishing conditions. In both cases, the F5 semi-finishing yields the shortest total machining time. A test is conducted using the F5 setup with 10 µm ADOC for semi finishing and the F1 setup with 3 µm ADOC as the final finishing process. The machined surface, as shown in Figure 3.13(b), has the same level of surface roughness, 0.09 µm R_a, as the surface machined only by the F1 setup as in Figure 3.13(a). The total machining time is reduced to 22 min (25 min from estimation) compared to 80 min using the single step machining by F1 at 11 µm ADOC (Figure 3.13(a)).

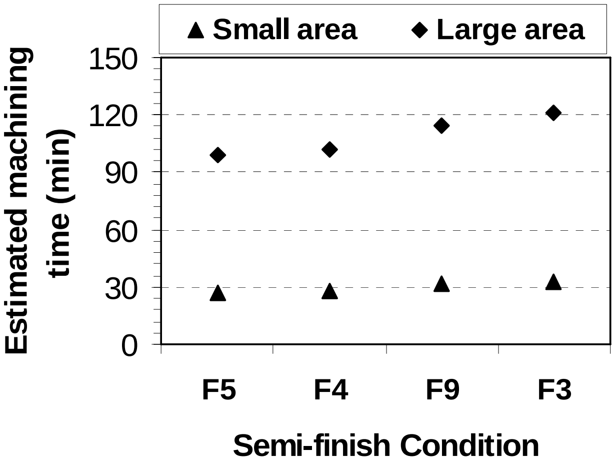

Figure 3.16. Estimation of total machining time with different semi-finish conditions.

Therefore, two steps are planned for the finishing processes: F5 setup with 10 μm ADOC for semi finishing and the F1 setup with 3 μm ADOC as the final finishing process.

3.6.3. Integrated Machining

In addition to the selected roughing and finishing processes, an intermediate machining step, near-dry EDM with F10 setup (Table 3.5), is found necessary to bridge to the two processes. Applying the tool path in Figure 3.17(a), totally five machining steps are applied to finish the flat surface in Figure 3.17(b). Table 3.5 lists the machining information for each step, including discharge setup, total machining depth, size of the square surface (*a*), machining time, and R_z and R_a of the machined surface.

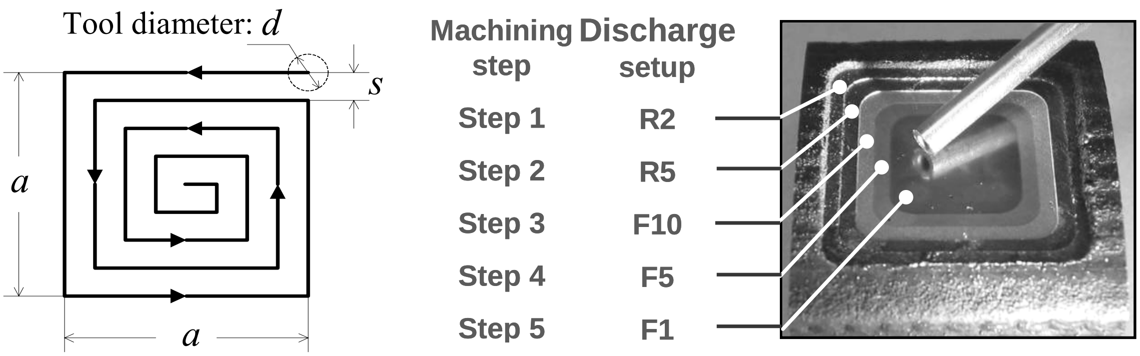

(a) (b)

Figure 3.17 Flat surface milling with integrated dry and near-dry EDM, (a) tool path and (b) finished mirror surface.

Table 3.5. Process information in finishing the DMD part.

Step	1	2	3	4	5
Discharge setup*	R2	R5	F10	F5	F1
Dielectric medium	Oxygen		Kerosene-air mixture		
Total machining depth (μm)	2100	50	30	10	3
a (mm)	17.5	15	12.5	10	7.5
Duration (min)	20	4	33	111	113
R_z (μm)	30	15	8	3	1
R_a (μm)	4.5	2	1	0.3	0.1

**Refer to Table 3.4 for parameters of setups R2 and R5 and Table 3.3 for F1 and F5. Parameters for F10 are* $i_e = 3$ *A,* $t_i = 2$ *μs,* $u_e = 30$ *V,* $t_0 = 5$ *μs and* $u_i = 210$ *V.*

In Steps 1 and 2, oxygen-assisted dry EDM is applied. Step 1 takes 7 cuts to make a pocket of about 2 mm depth on the DMD part. The total machining time is 20 min. In Step 2 reduces the surface roughness R_z from 30 to 15 μm in 4 min. Since the tool wear is fairly small in oxygen-assisted roughing, the flat surface is generated in one single path of machining.

From Step 3, the near-dry EDM using kerosene-air mixture is applied. The large tool wear in near-dry EDM finishing (TRW > 50% in Figure 3.12) becomes a challenge for the flat surface machining. Assuming a perfectly flat surface before machining, the machined surface height at the starting point will be lower than that at the ending point due to the tool shortening (wear) if only one single path of machining is applied. To overcome the problem, the machining has to be repeated along the same tool path. After each machining, the shortening of electrode is measured using the reference gauge attached to the machine. The shortening is then compensated by offsetting the electrode toward the workpiece with the same shortening amount. The machining is repeated several times until the measured electrode wear is less than 1 μm. Although the process is time consuming, it is a robust method without the automatic tool wear detection and compensation for flat surface EDM milling.

In Step 3, it takes three milling repetitions to complete the flat surface in 33 min. The surface roughness is reduced to 8 μm R_z. In Step 4, the semi-finishing by F5, seven milling repetitions are taken to flatten the surface to 3 μm R_z in 111 min. In Step 5, the final-finishing by F1, eight milling repetitions are taken to finish the surface to 0.1 μm R_a in 113 min.

Large portion of the machining time is consumed in the last three near-dry EDM finishing steps. It is partially due to the inherently low MRR. The relatively large tool wear and the need to compensate the tool wear to produce a flat surface also prolong the machining time. The real machining time is twice of the estimation due to the milling repetition. The machining time is expected to significantly reduce if the automatic tool wear compensation is applied.

3.7. Concluding Remarks

This study exploited the capability of dry and near-dry EDM milling in finishing operations. The effect of dielectric fluid, electrode material and discharge parameters was investigated. Near-dry EDM was found able to generate better surface finish than wet EDM under the same discharge condition. Kerosene based liquid-gas mixture and copper electrode was recommended for fine surface finish machining. Copper infiltrated graphite electrode can be a substitution for moderate surface finish if copper electrode cannot enable stable machining. Low discharge current (< 2 A), low discharge duration (< 2 μs) and negative polarity were found necessary for fine surface finish. A simple modification to reduce the discharge current turned out to be cost-effective to improve the surface finish. The near-dry EDM milling was proven capable of achieving a surface finish of 0.09 μm R_a with the aid of an advanced EDM pulse generator.

However, low MRR and high TWR was found associate with the EDM finishing process. Proper process planning was recommended to minimize the material removal in the finishing process to avoid excessive machining time. The problem of high TWR was overcome by repeating the machining path and sacrificing the machining speed. The development of tool wear compensation algorithm and searching of low wear electrode materials is highly recommended for future study.

CHAPTER 4

MODELING OF ANODE DISCHARGE CRATER FORMATION

4.1. Introduction

In EDM, the material removal is realized by rapidly reoccurring electrical discharges. In an individual electrical discharge, the plasma channel exerts intensive power density on the discharge spot to induce the material melting and expulsion and then leave a crater on the surface (DiBitonto et al., 1989). The consecutive discharges yield continual material removal and produce a machined surface composed of numerous overlapped discharge craters. This study aims to model the crater formation process, including the material melting, expulsion and re-solidification during an individual electrical discharge. The model can provide insights to the material behavior and crater formation during the electrical discharge process. The model is used to investigate the wet and near-dry EDM by comparing the effect of liquid and liquid-gas mixture dielectric fluids on the crater formation.

The modeling effort concentrates on the EDM finishing process. The finishing EDM typically has the negative polarity setup with the workpiece as the anode. This polarity has low cathode electrode tool wear at short discharge duration (< 3 μs) (Arunachalam, 1995) and smooth crater morphology on the anode surface (Tamura and

Kobayashi, 2004). Individual discharge craters are the dominant feature on the finishing EDM machined surface on anode. An example is shown in Figure 4.1(a). The model developed in this study will be able to estimate the anode material behavior in a discharge of the EDM finishing process. Even though both the anode and cathode experience rapid temperature rise and resultantly material melting, they are found to have distinct material expulsion mechanisms and generate different crater morphologies (Luo and Tao, 2008).

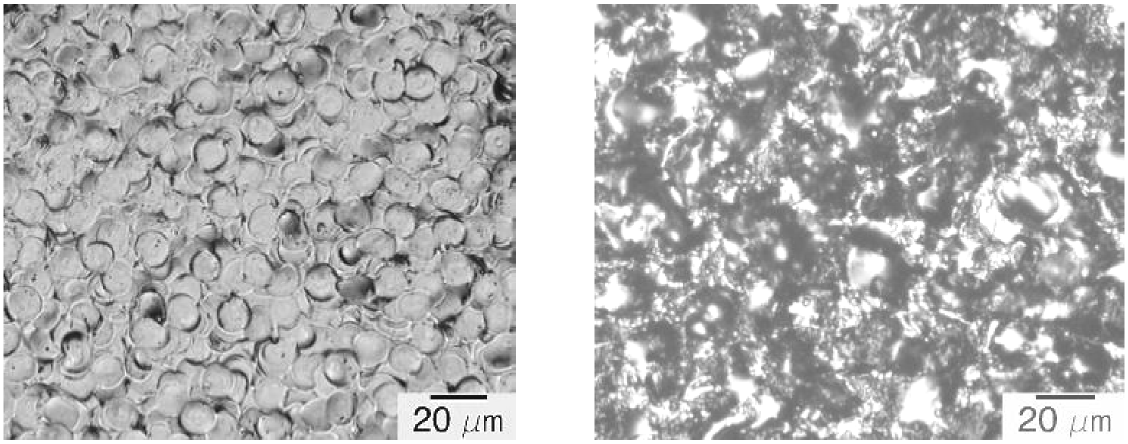

(a) (b)

Figure 4.1. EDM surfaces of H13 tool steel with (a) negative polarity showing surface with clear feature of individual discharge craters (discharge current, i_e = 1 A, discharge duration t_i = 0.5 μs, open circuit voltage and u_i = 210 V) (b) positive polarity showing rough surface with rugged features (i_e = 2 A, t_i = 4 μs and u_i = 210 V) (electrode: copper).

The anode crater formation during electrical discharge is composed of two phases: plasma heating and bubble collapsing. The plasma heating phase starts after the dielectric fluid break-down when a plasma channel is formed. The plasma heats the electrode with the high power density, melts the anode material, and forms a melt pool (DiBitonto et al., 1989). The temperature at the center of the plasma channel measured by spectrometer is high, ranging from 4000 to 8000K (Natsu et al., 2004). The plasma channel is filled with gaseous mix and expands as the discharge power input continues

(Eubank et al., 1993). The expansion of the plasma channel is constrained by the surrounding dielectric fluid. High pressure is built up inside the plasma. At the end of the discharge, the power input is ceased. The plasma, which is now in the form of bubble, is compressed by the surrounding fluid and starts to collapse. The collapsing of the bubble exerts impact on the melt pool and causes the splashing of the molten liquid (DiBitonto et al., 1989). Some molten liquid is ejected into the surrounding dielectric fluid and flushed away. The remainder resolidifies and becomes part of a discharge crater.

Considerable efforts on modeling the plasma heating phase and material removal in a discharge have been conducted. DiBitonto et al. (1989) modeled the cathode material melting using a point heat source model. Patel et al. (1989) proposed an expanding heat source model where a Gaussian distributed heat flux with time variant heating area was implemented as the heat source to melt the anode material. Eubank et al. (Eubank et al., 1993) developed a variable mass model capable to calculate the temperature and pressure in the plasma bubble. The expanding heat source model (Patel et al., 1989) has been adopt by finite element analysis (FEA) models to simulate the work-material melting, thermal stress, deformation and microstructure change caused by electrical discharge (Murali and Yeo, 2005; Yeo et al., 2007; Das et al., 2003; Lasagni et al., 2004). In this study, the expanding heat source model (Patel et al., 1989) is adopted. The heat input can be applied to predict the melting of electrode- and work-material. The material removal is due to the splashing of molten material by the collapsing plasma bubble in the discharge (DiBitonto et al., 1989; Patel et al., 1989).

On the study of collapsing plasma bubble, Shervani-Tabar et al. (2006) conducted numerical analysis on the discharge bubble dynamics and showed the bubble was squeezed at the end of the discharge by the surrounding dielectric fluid and impinged on the melt pool. Hockenberry and Williams (1976) experimentally studied the discharge bubble dynamics using the high-speed photography and suggested that the material removal was induced by the impingement of the liquid dielectric jets at the end of the discharge. Klocke et al. (2007) measured the force of the discharge and concluded that the bubble collapsing created a dominating impact force. Eckman and Williams (1960) theoretically derived the discharge bubble dynamics using the Navier-Stokes equation. Tohi et al. (2002) measured the discharge force using the Hopkinson bar method and achieved good match with Eckman and Williams' theoretical results (1960).

To the best of our knowledge, there is not yet a model incorporating both the plasma heating phase and the bubble collapsing phase to simulate the discharge crater formation. This study constructs a model that includes material melting, bubble compression and collapsing, and molten material splashing and re-solidification. The model is constructed based on FLUENT. For the plasma heating phase, the model can simulate the melting process and track the migrating melt fronts. The latent heat effect, which was not considered in previous research (Patel et al., 1989; Murali and Yeo, 2005; Yeo et al., 2007; Das et al., 2003), is included in this research. For the bubble collapsing phase, processes of multi-phase interaction, liquid splashing and liquid-solid transformation are simulated using the modules of volume of fraction (VOF) and melting and solidification in FLUENT.

The model is utilized to simulate and compare the discharge and crater formation in wet EDM with liquid kerosene and near-dry EDM with kerosene-air mixture dielectric fluid. Different levels of discharge pulse energy are also studied by the model. In the following sections, the modeling approach will be explained in detail. The simulation results will be presented and crater geometry is compared with experimental measurements. Parametric study on the bubble initial pressure is carried out to improve the prediction accuracy on the crater geometry.

4.2. Modeling Approach

The modeling of the plasma heating phase and bubble collapsing phase are introduced in the following two sections.

4.2.1. Plasma Heating Phase

In the following sections, the modeling of the plasma heating phase is introduced from the aspects of energy input, heat flux distribution, initial and boundary conditions, melting and solidification modeling and material properties.

Energy input:

The energy for heating up the anode workpiece, E_a, comes from the discharge pulse energy, E_d, and is expressed as:

$$E_a(t) = \eta E_d(t) = \eta \int_0^{t_i} i_e(t) u_e(t) dt \tag{4.1}$$

where i_e is the discharge current, u_e is the discharge voltage, t_i is the pulse duration and η is the energy partition factor to the anode. In this study, $\eta = 0.39$ used by Yeo et al. (2007) is utilized.

The power input for heating up the anode, $Q_a(t)$, can be expressed as:

$$Q_a(t) = \eta i_e(t) u_e(t) \qquad \text{(4.2)`}$$

The i_e and u_e are experimentally measured. Three EDM finishing conditions, as shown Figure 4.2, are studied and are denoted as I, II and III in descending order of their discharge energy.

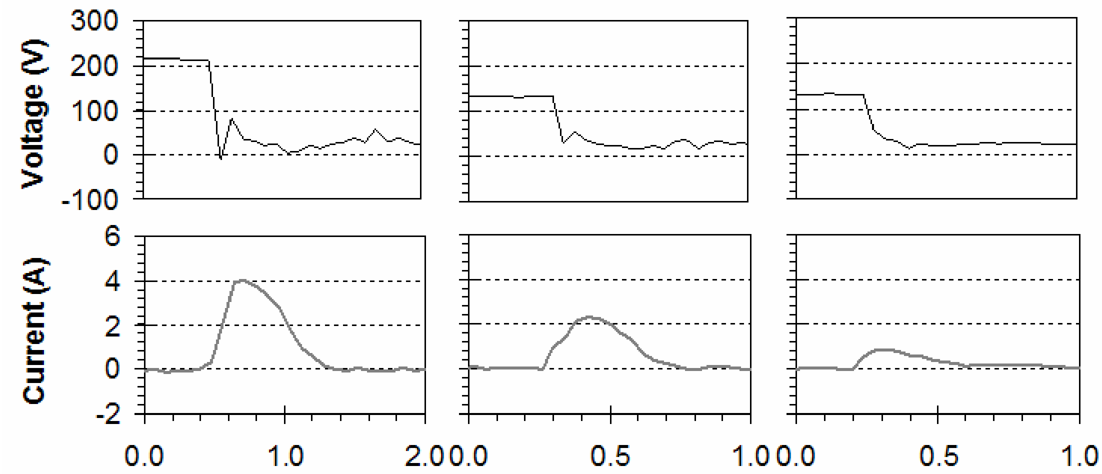

Condition I $E_d = 130$ μJ

Condition II $E_d = 30$ μJ

Condition III $E_d = 10$ μJ

Figure 4.2. Discharge waveforms of three experimentally measured discharge conditions.

Heat flux distribution:

Based on the expanding heat source model (Patel et al, 1989), the heat flux has a Gaussian distribution in the plasma channel, as shown in Figure 4.3. The time variant heat flux, $q_a(r, t)$, at a distance, r, from the center of the plasma column is expressed as:

$$q_a(r,t) = q_{\max}(t) \exp\left[-3\left(\frac{r}{r_p(t)}\right)^2\right] \tag{4.3}$$

where $q_{\max}(t)$ is the maximum heat flux (at $r = 0$) and $r_p(t)$ is the radius of the plasma heating area on the anode surface. Assuming a column shaped plasma, $r_p(t)$ is equivalent to the radius of the plasma. $r_p(t)$ grows with time and is given by (Patel et al, 1989):

$$r_p = 0.788 \times t^{3/4} \tag{4.4}$$

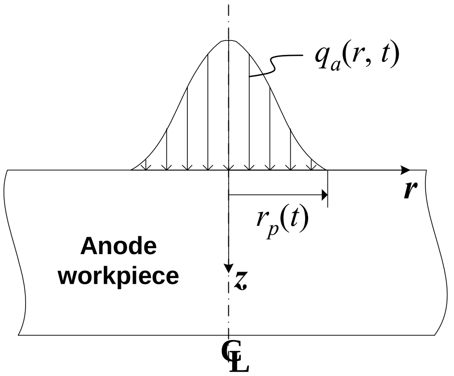

Figure 4.3. Profile of Gaussian distributed heat flux.

The integration of the heat flux, $q_a(r, t)$, over the plasma heating area is the total power input for heating the anode, $Q_a(t)$:

$$Q_a = \int_0^{r_p} q_a 2\pi r dr \tag{4.5}$$

Since $r_p(t)$ and $Q_a(t)$ are known for a specific time, t, $q_a(r, t)$ can be solved.

Model schematics and initial and boundary conditions

The axisymetric schematics of the model are shown in Figure 4.4. The plasma heating phase modeling only includes the region of the anode workpiece, DFHG region in Figure 4.4. The anode region is 100 and 80 μm along the ***r*** and ***z*** direction, respectively. This region is divided into 0.05 by 0.05 μm grids (cells).

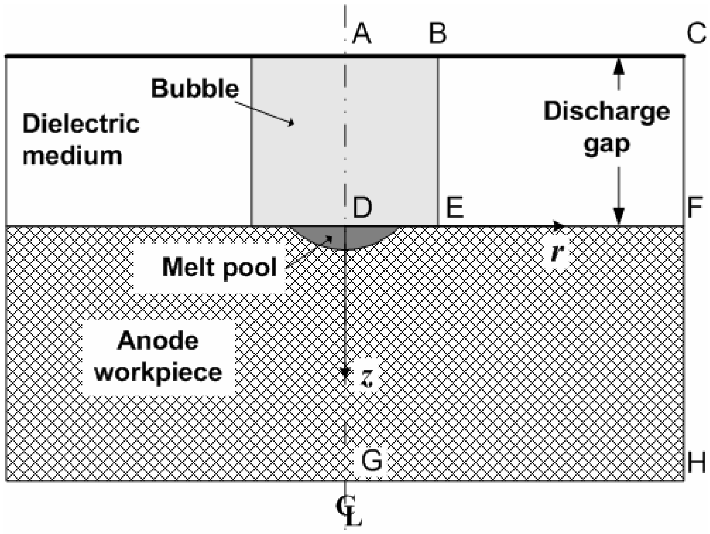

Figure 4.4. Schematics of the bubble collapsing model.

The initial temperature, T_i, of the workpiece is equal to the 300 K ambient temperature, T_0, at $t = 0$ for the entire anode region.

At $t > 0$, the heat source is applied on the anode surface, line DF. The heat flux boundary condition can be expressed as:

$$z = 0,\ k\frac{\partial T}{\partial z} = \begin{cases} q_a(r,t), \text{ if } 0 < r < r_p \\ 0, \text{ if } r > r_p \end{cases} \tag{4.6}$$

where k is the thermal conductivity of the workpiece material. The boundary condition at lines FH and GH (see Fig. 4), which are away from the discharge region, is assumed at a constant temperature T_0.

Melting and solidification:

The melting and solidification module in FLUENT is utilized to simulate the rapid heating and cooling of the material during a discharge. The enthalpy-porosity method (FLUENT Manual, 2003) is applied to tackle the energy balance and viscosity change in the melting process. The melt interface is not tracked explicitly. Instead, a quantity called the liquid fraction, β, which indicates the fraction of the cell volume that is in liquid form, is computed based on an enthalpy balance. The total enthalpy of the material, H, is composed of the sensible enthalpy, h, induced by the material temperature change, and the latent heat, ΔH, induced by the phase change:

$$H = h + \Delta H \tag{4.7}$$

$$h = h_{ref} + \int_{T_{ref}}^{T} C_p dT \tag{4.8}$$

$$\Delta H = \beta L \tag{4.9}$$

where h_{ref} is the reference enthalpy, T_{ref} is the reference temperature, L is the latent heat of the material and β is the liquid fraction. The work material, H13 tool steel, is an alloy material. The melting involves the mushy zone (Metals Handbook, 1980) and β can be expressed as:

$$\beta = \begin{cases} 0, & T < T_{solidus} \\ \dfrac{T - T_{solidus}}{T_{liquidus} - T_{solidus}}, & T_{solidus} < T < T_{liquidus} \\ 1, & T > T_{liquidus} \end{cases} \tag{4.10}$$

Material properties:

Tables 4.1 and 4.2 summarize the material properties of H13 tool steel. For the temperature-dependant properties, the linear interpolation is applied at the temperature level that is not prescribed by the tables.

Table 4.1. Constant thermophysical properties for H13 tool steel (Han et al., 2005; Childs et al., 2005).

Nomenclature	Symbol	Unit	Value
Solid density	ρ_s	kg/m^3	7760
Liquid density	ρ_l	kg/m^3	7000
Solid heat capacitance	$C_{p\text{-}s}$	J/kg-K	460
Liquid heat capacitance	$C_{p\text{-}l}$	J/kg-K	480
Latent heat of melting	$L_{\text{-}h}$	kJ/kg	250
Solidus temperature	T_s	K	1634
Liquidus temperature	T_l	K	1744
Reference enthalpy	h_{ref}	J/kg-mol	0
Dynamic viscosity of molten material	μ	(kg/m-s)	0.006
Surface tension coefficient	γ	N/m	1.9

Table 4.2. Temperature-dependent thermal conductivity for AISI H13 tool steel (Metals Handbook, 1980).

Temperature (K)	α
373	10.4
473	11.5
698	12.2
813	12.4
923	13.1

4.2.2. Bubble Collapsing Phase

In the following sections, the modeling of the bubble collapsing phase is introduced from the aspects of model schematics and initial and boundary conditions, VOF modeling and liquid, solid and mushy region modeling.

Model schematics and initial and boundary conditions

Figure 4.4 shows the axisymetric schematics of the bubble collapsing model. In addition to the anode region DFHG modeled in the plasma heating phase, the bubble (region ABDE), cathode surface (line AC) and dielectric fluid (region BCFE) are also included in the model. The same 0.05 μm square grid (cell) as in the anode region is applied.

As part of the initial conditions for the bubble collapsing phase, the temperature profile and melt pool geometry in the anode region DFHG are imported from the plasma heating phase. The cathode, line AC, is simplified as a rigid and adiabatic boundary with the same temperature distribution as that on the anode surface (line DF). The vertical distance between the cathode and anode surfaces, i.e. the discharge gap distance in Figure 4.4, is 20 μm and is determined experimentally by measuring the actual depth of cut and tool wear of the die-sinking EDM. The variation is less than 10% for all the investigated discharge conditions.

The column-shape bubble, region ABED, is adjacent to the anode melt pool. The initial radius of the bubble is equal to the plasma radius at the end of the plasma heating phase, which is determined by Equation 4.4. The bubble is filled with kerosene vapor, which is modeled as compressible ideal gas with properties listed in Table 4.3.

Table 4.3. Properties of kerosene vapor, kerosene liquid and air (FLUENT 6.3 User's Guide, 2006).

Model parameter	Symbol	Unit	Bubble	Dielectric fluid	
			Kerosene vapor	Kerosene	Air
Density	ρ	kg/m^3	Follow ideal-gas law	780	1.23
Molecular weight	m	kg/mol	167	167	29.0
Heat capacitance	C_p	J/kg-K	460	2090	1006
Thermal conductivity	k	(W/m-K)	0.018	0.149	0.024
Dynamic viscosity	μ	(kg/m-s)	7.0×10^{-6}	0.0024	1.8×10^{-5}

The initial temperature in the bubble is set at 5000 K (Natsu et al., 2004). The initial bubble pressure of 200 MPa, which falls into the estimated range according to the previous studies (Eubank et al., 1993; Eckman and Williams, 1960), is used in the first set of simulations. Since large variation is encountered in the bubble pressure estimation

(Eubank et al., 1993; Eckman and Williams, 1960), the second set of simulations study the effect of initial bubble pressure at four levels, 20 MPa, 200 MPa, 2GPa and 20 GPa, on crater geometry.

The region BCFE is filled with dielectric fluid. Liquid kerosene and kerosene-air mixture, which is composed of 20% kerosene and 80% air, are used for the wet and near-dry EDM simulations, respectively. Both the liquid kerosene and kerosene-air mixture are modeled as incompressible phase and properties are in Table 3. The initial temperature in the dielectric fluid region is assumed to have an exponential decaying distribution. At the bubble and dielectric fluid interface (line BE), 5000 K is assigned to the dielectric fluid and it exponentially drops to the ambient temperature, 300 K, at the boundary line CF. The boundary line CF is set as a pressure inlet with the flow direction perpendicular to the line CF. The initial pressure of boundary CF is set equal to the initial bubble pressure and is assumed to decay exponentially with a time constant of 10^{-8} s once the bubble is collapsed.

VOF modeling:

Since five phases, kerosene vapor, air, kerosene liquid, molten steel and solid steel co-exist in the bubble collapsing model, the VOF module is applied to analyze their interactions. The VOF models immiscible fluids (or phases) by solving a set of momentum equations and tracking the volume fraction of each of the phases (FLUENT User's Guide, 2006). The five phases are not interpenetrating in the model. For each phase, q, in the model, a variable, a_q, the phase volume fraction in the computational cell, is assigned to the phase. The volume fraction of phase q in the cell can be described by one of following three conditions:

$a_q = 0$, if the cell is empty of phase q;

$a_q = 1$, if the cell is full of phase q;

$0 < a_q < 1$, if the cell contains the interface between phase q and one or more other phases.

Based on the local value of a_q, the properties, such as density, ρ, and viscosity, μ, of the cell are approximated with a volume-averaged manner (FLUENT User's Guide, 2006), i.e.,

$$\rho = \sum \alpha_q \rho_q \tag{4.11}$$

$$\mu = \sum a_q \mu_q \tag{4.12}$$

The momentum equation is solved throughout the computational cell, and the resulting velocity vector, $\vec{v}$, is shared among the phases. The momentum equation is dependant on the volume-averaged density, ρ, and viscosity, μ, within the cell. The moment equation is (FLUENT User's Guide, 2006):

$$\frac{\partial}{\partial t}(\rho\vec{v}) + \nabla \cdot (\rho\vec{v}\vec{v}) = -\nabla p + \nabla \cdot \left[\mu\left(\nabla\vec{v} + \nabla\vec{v}^T\right)\right] + \rho\vec{g} + \vec{F} \tag{4.13}$$

where p is the pressure at the center of the cell, $\vec{g}$ is the gravitational acceleration and $\vec{F}$ is the volumetric force.

The energy equation is solved with the velocity vector also shared among the phases (FLUENT User's Guide, 2006):

$$\frac{\partial}{\partial t}(\rho E) + \nabla \cdot (\vec{v}(\rho E + p)) = \nabla \cdot \left(k_{eff}\nabla T\right) + S_h \tag{4.14}$$

where k_{eff} is the volume-averaged effective thermal conductivity and S_{h} is the volumetric heat sources. The energy, E, and temperature, T, are treated as mass-averaged variables (FLUENT User's Guide, 2006):

$$E = \frac{\Sigma \alpha_q \rho_q E_q}{\Sigma \alpha_q \rho_q} \tag{4.15}$$

$$T = \frac{\Sigma \alpha_q \rho_q T_q}{\Sigma \alpha_q \rho_q} \tag{4.16}$$

Liquid, solid and mushy region modeling:

Additional effort is needed to model the phases of liquid, solid and mushy zone, which co-exist at the alloy melting stage. It is difficult to incorporate both fluid and solid type cells together in the same analysis domain since they are constructed with different principles. In this study, both liquid and solid phases are modeled using the fluid type cell. Methods of temperature-dependant viscosity proposed by Li et al. (2002) and enthalpy-porosity technique built in FLUENT (FLUENT User's Guide, 2006) are adopted to make the modeling of solid and mushy phase possible. In the temperature-dependant viscosity method, the element of temperature lower than the solidus temperature is assigned a very high viscosity (100 to 2000 N-s/m depending on the simulation stability) to mimic the solid status. In this way, the flow or movement of the solid work-material is very small and its influence on the modeling accuracy is limited. If the material temperature is higher than the liquidus temperature, the material is in the liquid phase and the viscosity value listed in Table 1 is assigned.

Between the solidus and liquidus temperature, i.e., in the mushy zone, an intermediate viscosity could be used to simulate the solidus status. FLUENT's enthalpy porosity method is more effective to handle the transition between liquid and solid. It treats the mushy region as a porous medium (FLUENT User's Guide, 2006). The porosity is set equal to the liquid fraction in that cell. Thus, higher portion of the liquid fraction, i.e., more molten liquid, induces less stagnancy to dissipate the momentum of the fluid flow, i.e., the relative motion between the liquid and solid in the mushy zone. The momentum dissipation, M_d, in the mushy zone is (FLUENT User's Guide, 2006):

$$M_d = \frac{(1-\beta)^2}{(\beta^3+\varepsilon)} A_{mush} (\vec{v} - \vec{v}_p) \tag{4.17}$$

where β is the liquid fraction, ε is a small number to prevent division by zero for fully solidified case, $\vec{v}_p$ is the vector of solid velocity due to entire movement of the domain, and A_mush is the dimensionless mushy zone constant. Higher A_mush causes large energy dissipation. In this study, A_mush equals to 10^7 (FLUENT User's Guide, 2006) is used.

4.3. Simulation Results

4.3.1. Plasma Heating Phase

Figure 4.5 shows the simulation results of the temperature distribution on the anode work-material and solid fraction during the 0.5 μs plasma heating phase in discharge condition III (Figure 4.2). It is observed that the heated area on the anode increases with the duration of the plasma heating. The peak temperature is 10900 K at 0.1 μs and drops to 3400 K at 0.5 μs. The drop of the peak temperature is mainly due to the expansion of the plasma channel, which reduces the discharge power density, and the dissipation of energy to the surrounding area.

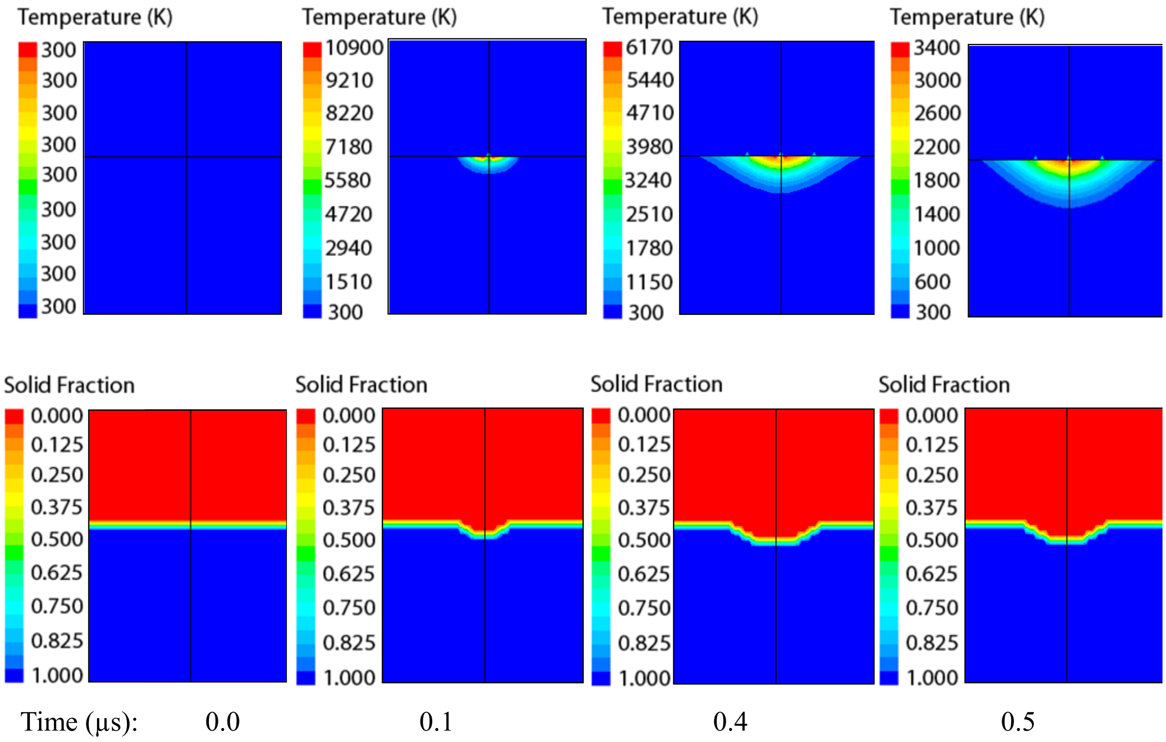

Figure 4.5. Simulation of the plasma heating phase.

The second row of plots in Figure 4.5 shows the solid fraction of the work-material representing its melting and solidification status. At the start (0.0 μs), the anode work-material (bottom portion in Figure 4.5) has 100% solid phase. The upper portion is the non-solid phase, which can contain both the molten liquid and other liquid phases, including the bubble and surrounding dielectric fluid. There is a thin transition band between the solid and liquid phases used in FLUENT to avoid abrupt change of phases and the associated computational problem. The transition band, about 1 μm thick, exists in all diagrams of phase fraction results. As the temperature rises, the anode workpiece starts to melt and a cavity formed on top indicates the formation of melt pool. The size of melt pool reaches the maximum at about 0.4 μs. After that, the growth stops. The size of melt pool at 0.5 μs is slightly smaller than that at 0.4 μs. This is related to the temperature drop during the plasma heating phase. The expansion of the plasma channel reduces the heating power density to such a level that the heat dissipation, mainly induced by conduction, surpasses the thermal input. The shrinkage of melt pool size during the plasma heating phase is a waste of discharge energy. Therefore, the modeling of plasma heating phase can potentially be applied to optimize the discharge power and duration to improve the material removal rate and energy efficiency.

4.3.2. Bubble Collapsing Phase

Figure 4.6 shows the simulation results of the bubble collapsing phase in wet EDM of discharge condition III. The plots of bubble fraction, work-material fraction and solid fraction are display at simulation time steps of 0.0, 0.12, 0.22, 0.32, 0.42 0.52 μs to describe the crater formation process.

As shown in the bubble fraction, the initial bubble column is 15 μm in diameter and 20 μm in height at 0.0 μs. The bubble is compressed rapidly due to the quick temperature drop and the high pressure of the surrounding dielectric fluid. At 0.12 μs, the bubble is compressed to less than 5 μm in diameter. The bubble collapses at around 0.22 μs when the dielectric fluid penetrates the bubble and breaks it into small pieces. The collapsing of bubble exerts an impact on the melt pool and causes splashing of the molten work-material.

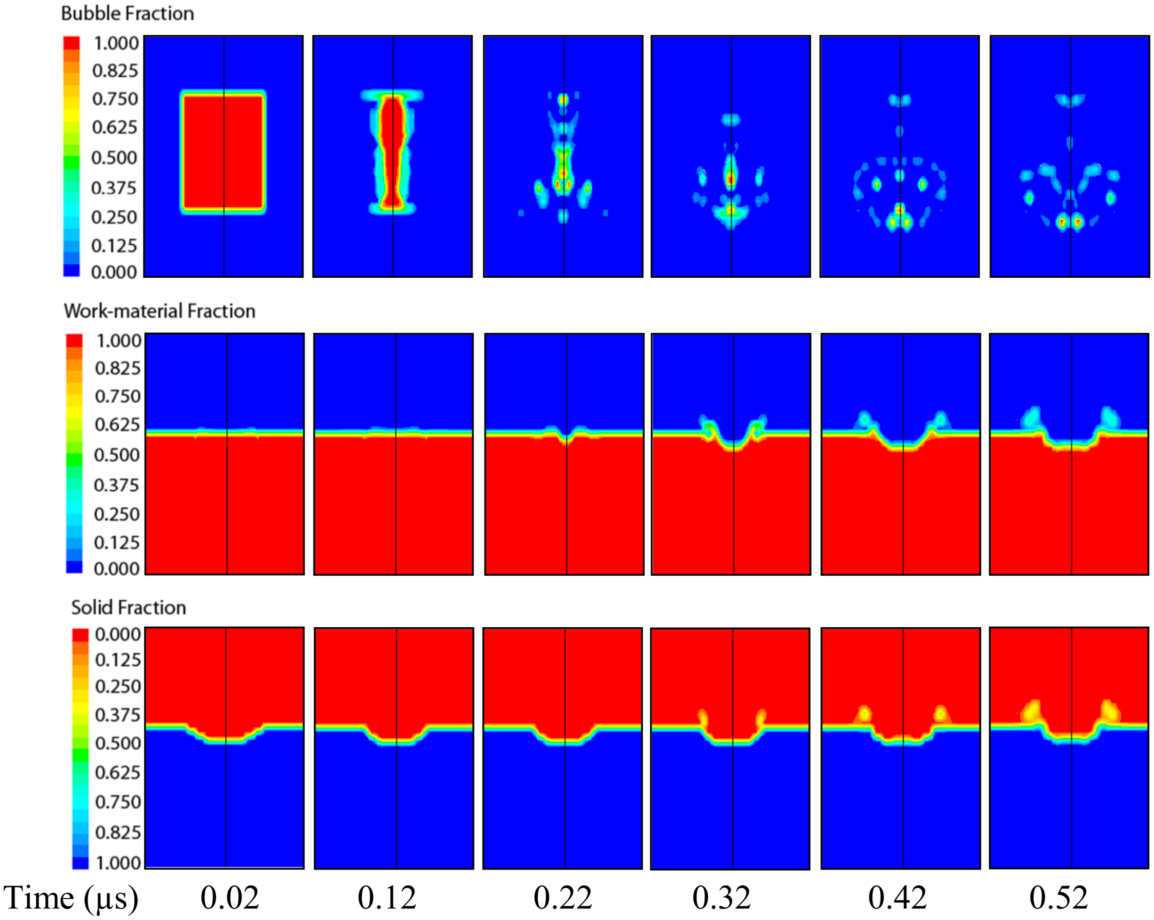

Figure 4.6. Simulated bubble collapsing phase in near wet EDM under discharge Condition III.

In the plots of the work-material fraction, the bottom portion represents the anode work-material. At 0.12 μs, before the collapsing of the bubble, the molten part of the work-material deforms slightly. At 0.22 μs, as the bubble collapses, the impact causes a dimple at the center of the melt pool. The molten liquid is agitated and displaced towards the side of the melt pool at 0.32 μs. Part of the material starts to detach from the melt pool at 0.42 μs. The detached material solidifies into small droplets and becomes ejected debris particles. The remainder molten material does not attain enough momentum from the impact and resolidifies and becomes the crater and part of the recast layer on the EDM surface.

In the plots of the solid fraction, the bottom portion is the solid (un-melt) work-material and a cavity of the melt pool in liquid phase can be identified. Before the bubble collapsing at 0.22 μs, solidification of the molten pool is observed from the reduction of the cavity size. The impact induced by the bubble collapsing displaces the molten material and induces strong convection in the melt pool. The ejected molten material starts to solidify 0.32 μs and becomes debris droplet at 0.42 μs. The final formation of the crater is at 0.52 μs when the profiles of the work-material fraction and solid fraction become identical indicating the complete solidification of the molten material.

4.3.3. Simulated Craters

The crater geometry, represented by the work-material fraction after the material solidification for near-dry and wet EDM under discharge conditions I, II and III are shown in Figure 4.7. The initial bubble pressure is set to 2×10^8 Pa. The model predicted crater geometry will be compared to the experimentally measured craters for model validation.

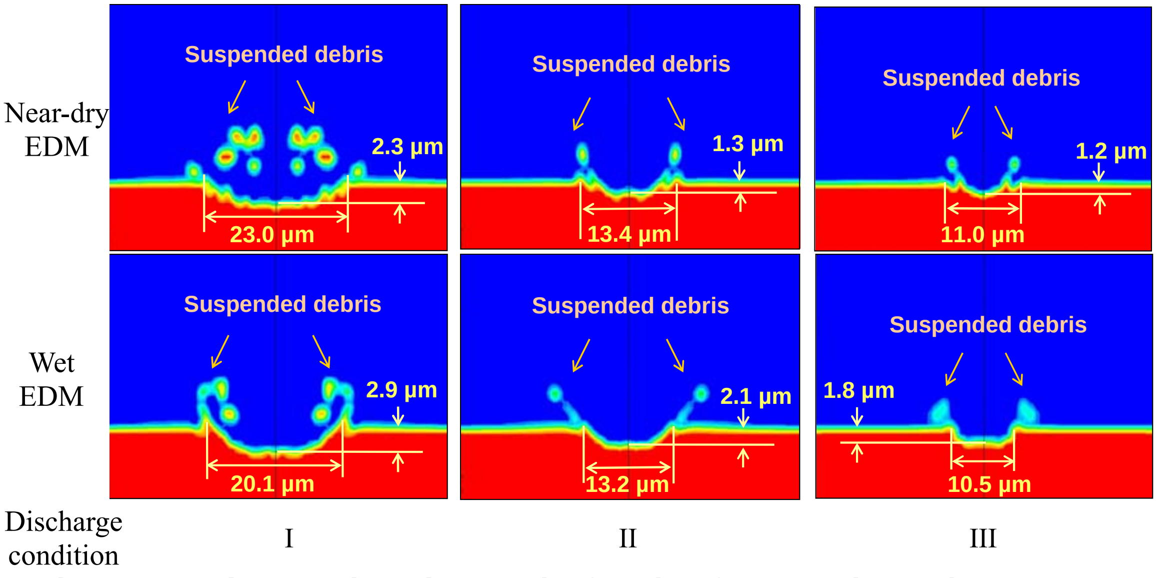

Figure 4.7. Simulated work-material fraction for near-dry and wet EDM craters under discharge Conditions I, II and III.

For discharge conditions I, II, III, the crater diameter is estimated to be 23.0, 13.4, 11.0 µm for near-dry EDM and 20.1, 13.2, 10.5 µm for wet EDM. In general, the near-dry EDM has slightly larger crater diameter than that of the wet EDM. The opposite trend is observed for the crater depth, i.e., near-dry EDM has shallower crater depth than that of dry EDM. The crater geometry is affected by density, viscosity and thermal conductivity of the dielectric fluid. The high density and viscosity of the kerosene liquid in wet EDM yields larger momentum when compressing the bubble and causes stronger impact at the bubble collapsing. The molten material is agitated and ejected deeper from the molten pool than near-dry EDM. Therefore, the crater is deeper and has smaller diameter for wet EDM.

The crater diameter and depth is observed to reduce with the decrease of discharge energy in discharge conditions I to III. With lower discharge energy to melt less material, smaller size of the melt pool is generated and the size of the final crater is reduced.

4.4. Experimental Crater Generation and Measurement

Experiments were performed to create discharge craters. The size and shape of the crater is measured using the NanoScope IIIa-phase atomic force microscope (AFM) using the J-type scanner head at tapping mode, 0.4 Hz scanning rate and 0.07 µm resolution. The measured crater geometry is compared with the model prediction.

Discharge craters can be generated under different discharge conditions. The EDM process creates overlapping craters, as illustrated in Figure 4.1(a), and difficult to accurately measure individual crater geometry. The single discharge process (Wong et al., 2003; Natsu et al., 2006) can be utilized but the discharge gap is small (Wong et al., 2003) which is different from that the EDM condition. A new method called sparsely continual discharge (SCD) is utilized.

In SCD, the workpiece is first polished to a mirror finish to make sure the small discharge craters can be distinguished from the original surface. For a 10 mm x 10 mm area, H13 anode work-material and copper electrode, the discharge gap distance is around 20 µm, which is very close to the gap distance in the continual discharge condition. After about 2 to 3 s of discharge, a cluster of sparsely distributed craters can be observed on the surface for analysis. Figure 4.8 shows an example of the crater cluster for near-dry EDM using discharge Condition II. Craters with reasonable consistency in size and shape are attained. Representative craters are thus selected for measurement and analysis.

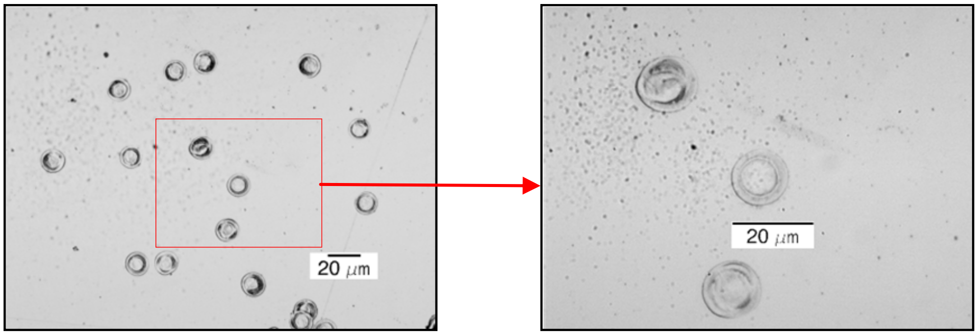

Figure 4.8. Discharge craters generated by continual discharge process (near-dry EDM with discharge Condition II).

Figure 4.9 shows the optical micrograph, AFM 3D image, and cross section of craters generated under wet and near-dry EDM with discharge Conditions I, II and III. The optical micrograph, AFM 3D image are for visual assessment of the crater morphology. The crater cross section is obtained from AFM data and applied to measure the crater diameter and depth.

As seen in Figure 4.9, from Conditions I to III, the crater size reduces with the decrease of the discharge energy. When the discharge energy is 130, 30, 10 µJ, the crater diameter is around 20, 13, 10 µm and the peak crater depth is around 2.0, 0.4, 0.1 µm. From Condition I to Conditions II and III, the reduction of the crater depth is significant. For crater under discharge Condition II and III, a bulged bottom is observed the center of the crater. It is most obvious for the crater generated by near-dry EDM with Condition II and can be identified simply from the 3D image. The cross section profiles show that the similar bulged bottom exists in discharge Conditions II and III. For Condition III, the bulged center can even raise above the original surface level causing a slightly negative depth. This is effective to make a flattened crater and achieve fine surface finish on the machined surface in EDM finish machining.

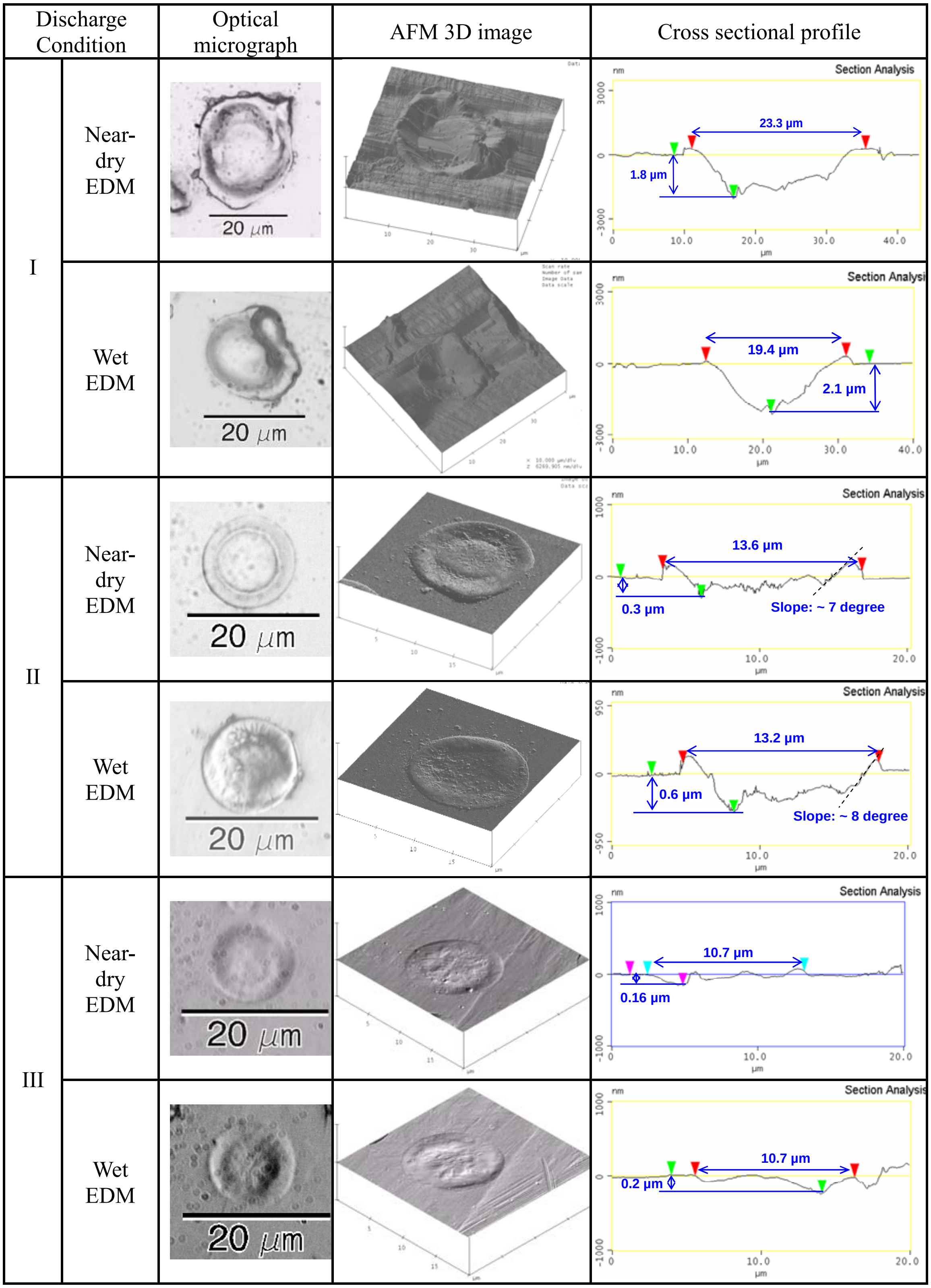

Figure 4.9. Experimental craters under six EDM conditions.

Wet and near-dry EDM generate different crater, especially in the high discharge energy case, Condition I. The near-dry EDM crater has larger diameter (23 μm vs. 18 μm) and smaller depth (1.8 μm vs. 2.3 μm). Under the same EDM condition, a relatively flat crater is created in near-dry EDM, which is more suitable for finishing EDM, as discussed in previous chapter. The crater diameter and depth is related to the different dielectric fluid properties. The kerosene-air mixture used in near-dry EDM has lower viscosity and density because of the dilution by air. It generates less momentum when compressing the bubble and consequently smaller bubble collapsing impact force.

As the pulse energy decreases, the differences in crater geometry between the near-dry and wet EDM become less obvious. For Condition II, the crater generated by near-dry EDM is slightly shallower, around 0.3 μm, in depth. No significant difference of crater geometry is observed between near-dry and wet EDM for Condition III. The smaller discharge energy reduces the bubble collapsing impact force. The molten material thus attains less momentum to overcome the surface tension of the melt pool. As the surface tension plays a larger role for low pulse energy EDM, the higher impact force in wet EDM is not significant enough to yield a deeper crater than in wet EDM.

4.5. Comparison and Discussion

Figure 4.10 compares the diameter and depth of the model predicted and experimentally measured discharge craters. The model provides good prediction on the crater diameter with less than 10% deviation from the mean value of the experiments for all the six discharge conditions. It captures characteristics of actual crater formation. Both modeled and real craters in Figures 4.8 and 4.9, respectively, show features of ridge and bulged crater bottom. The model distinguishes the craters generated by near-dry and wet EDM and predicts the trend of decreasing crater size with the reduction of discharge energy. However, the model is not able to accurately estimate the shallow crater depth in Conditions II and III.

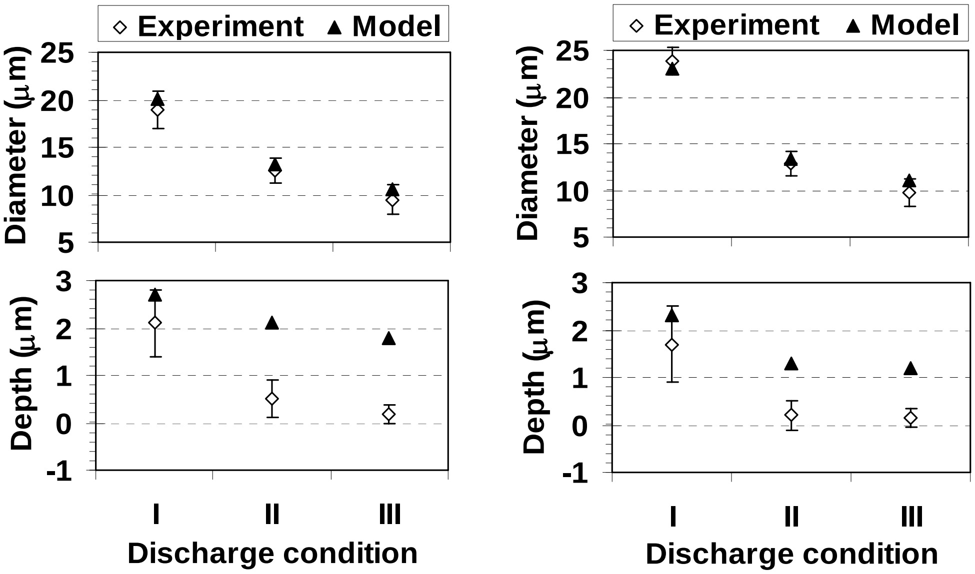

(a) Wet EDM (b) Near-dry EDM

Figure 4.10. Dimensional comparison of experimental and simulated craters.

The model tends to overestimate the crater depth. For Condition I, which has relatively high pulse energy, 130 μJ, the simulated crater depth is in the upper range of experimental variation. As the discharge energy drops to 30 and 10 μJ for Conditions II and III, respectively, the experimentally measured crater depth reduces to less than 1 μm and some bulged part of the crater even rises above the original surface level. In these cases, the simulated craters are all deeper than 1.2 μm.

The overestimation of the crater depth can be attributed to several reasons. First, the specific volume of the solidified metal can increase, i.e., the material volume expands, if the cooling rate exceeds a critical value (Reed-Hill and Abbaschian, 1994). The cooling rate encountered during the discharge crater formation is higher than 10^9 K/s as estimated by the simulation. This rapid cooling rate has surpassed the critical value, generally 10^5 K/s (Reed-Hill and Abbaschian, 1994), for metallic alloys. The steel work-material is thus expected to expand during solidification after the discharge. The expanded volume occupies more space in the crater and reduces the crater depth.

Second, the melt pool depth can possibly be overestimated. A rough estimation of the actual melt pool depth is to sum up the measured crater depth, which is less than 0.9 and 0.4 μm for Conditions II and III, respectively, and the recast layer thickness, which is less than 1.7 and 1.5 μm in continual EDM with Conditions II and III, respectively. Although this causes overestimation because multiple recast layers may overlap in continual EDM, the deduced pool depth (2.6 and 1.9 μm for Conditions II and III, respectively) is still smaller than the simulated results (2.7 and 2.2 μm for Conditions II and III, respectively).

Third, the initial bubble pressure in the simulation is uncertain. In the simulation, the initial bubble pressure was 2×10^8 Pa for all the discharge conditions. Because the build-up of the bubble pressure is related to the discharge pulse energy, the actual pressure should vary. Higher energy is expected to expand the bubble more violently, resulting in a higher initial bubble pressure and consequently stronger compression at the end of the discharge. To overcome the absence of accurate bubble pressure, study is conducted in the next section to investigate the effect of initial bubble pressure on the crater formation.

4.6. Effect of Initial Bubble Pressure

The simulation is conducted at four levels of initial bubble pressure, 2×10^7, 2×10^8, 2×10^9 and 2×10^{10} Pa, in near-dry EDM with discharge Conditions I, II and III. Results are shown in Figure 4.11.

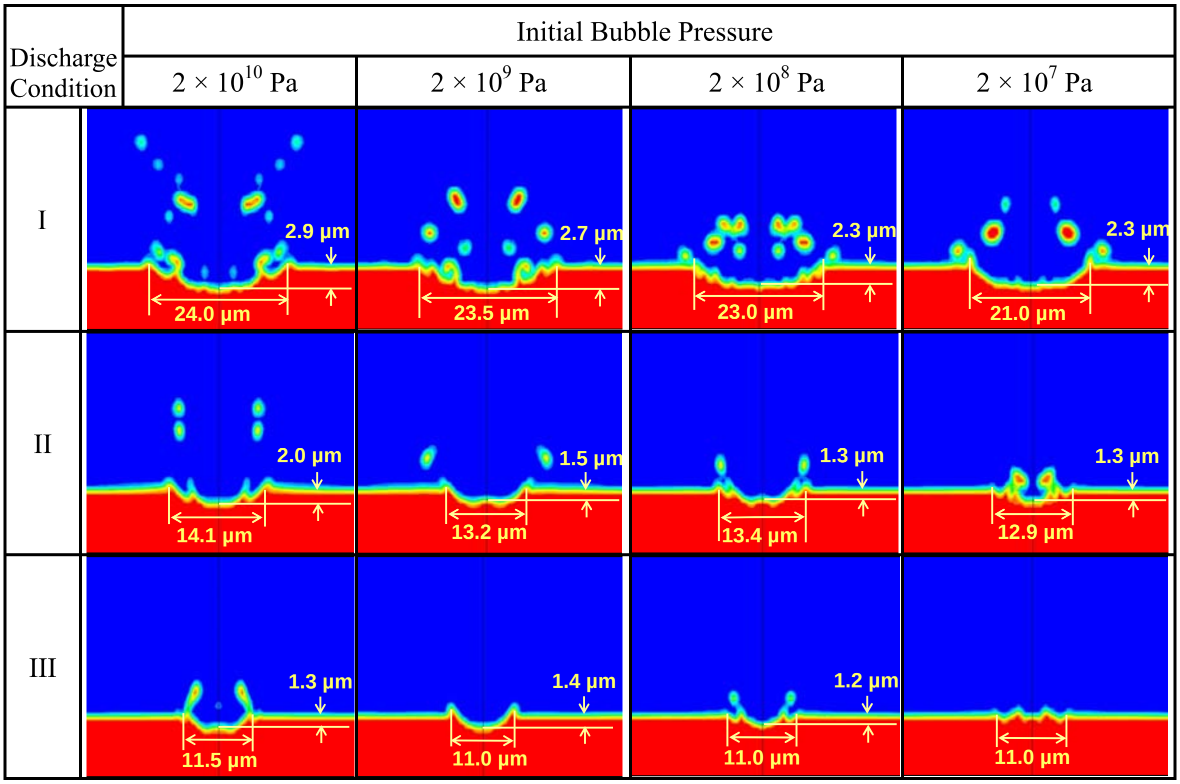

Figure 4.11. Effect of initial bubble pressure in near-dry EDM on craters geometry in three discharge conditions.

In Figure 4.11, the simulated crater diameter and depth increases with the rise of the initial bubble pressure. For Conditions I, II and III, when the initial bubble pressure is increased from 2×10^7 to 2×10^{10} Pa, the percentages of crater diameter and depth increases are 14%, 9% and 5% and 26%, 50% and 30%, respectively. The variation of initial bubble pressure has a larger effect on the crater depth. Also, the material ejection appears more violent in the high pressure case with wider spread debris droplets.

Comparing the simulated and real craters, the initial bubble pressure of 2×10^8 Pa provides the closest prediction on crater diameter and depth for Conditions I and II. For Condition III, the pressure of 2×10^7 Pa yields a good match in the simulated and real crater profiles (Figure 4.9, near-dry EDM with Condition III). In both profiles, the side slightly slides downward while the center bulges up and rises above the original surface level. No material ejection happens in that simulation.

The prediction of the crater depth does not improve by varying the initial bubble pressure in discharge Conditions I and II. The bubble pressure is not the major factor for the crater depth overestimation by the model. The other two factors, material volume expansion and overestimation of the melt pool depth, discussed in Section 5 are inferred as the major problems that should be solved to improve the model accuracy.

The model improvement can be expected as follows. First, model parameters in the plasma heating phase, which have used the literature values in the current study, should be revised to better fit the low discharge energy (less then 100 μJ) case. Second, the factor of material expansion at high cooling rate needs to be included by implementing an empirical data base that correlates the change of material specific volume with its cooling rate. Also, another potential advancement is to incorporate the modeling of bubble expansion. With that, a more accurate bubble pressure can be utilized instead of using the literatures values. The challenge is that the bubble expansion modeling requires two compressible flows, one for vapor bubble and the other for surrounding dielectric fluid. Currently, this condition is infeasible for FLUENT and other CFD software.

4.7. Concluding Remarks

This study demonstrated a model for the discharge crater formation on anode electrode. Advancing based on the plasma heating model (Patel et al., 1989), the model developed in this study could handle the material melting and solidification by taking the latent heat into consideration. This model further incorporated the bubble collapsing phase to simulate the multi-phase interactions among dielectric fluid, bubble, molten material, and solid workpiece. The modeling of discharge crater formation process using FLUENT software was proven feasible by comparing with experimentally measured crater diameter and depth. .

The experimental validation was conducted using SCD which can better imitate the practical EDM process. The simulation generated realistic crater morphology, such as build-up crest and bulged bottom. The model provided good prediction on the crater diameter. Both the experiment and simulation suggested that the near-dry EDM using kerosene-air generates larger but shallower discharge craters than wet EDM using liquid kerosene. The model traced the trend of reducing crater size with the decrease of discharge energy. The initial condition of the bulb pressure influenced the simulation accuracy to some extent. The initial bubble pressure ranging from10^7 to 10^8 Pa was found appropriate to simulate the crater geometry that can match with the experiments. Lower initial bubble pressure was found associated with the lower discharge pulse energy.

The model was found to overestimate the crater depth. The reason was identified as the inaccurate initial bubble pressure input, the overestimation of the melt pool depth and the ignorance of the material volume expansion under high cooling rate. The model could be improved by revising the plasma heating phase model to better estimate the melt pool size and by incorporating the cooling-rate effect on the material specific volume.

CHAPTER 5

CONCLUSIONS AND FUTURE WORK

This research is a contribution to the on-going development of next-generation EDM process. The dry and near-dry EDM milling process was investigated through the experimental exploration and process modeling.

5.1. Major Contributions

The major contributions of this research are made in two areas:

Integrated dry and near-dry EDM milling processes development

- The feasibility of dry and near-dry EDM milling processes was demonstrated using gas and liquid-gas mixture as non-conventional dielectric media and rotating tubular tool electrode with the internal flushing of dielectric fluids.
- The oxygen-assisted dry EDM milling was proved as an ideal EDM roughing process capable to achieve high MRR and the rapid oxidation was recognized as the mechanism for its enhanced MRR.

- The DOE was conducted to investigate the oxygen-assisted dry EDM roughing process. Key discharge parameters and their effects were identified.
- The near-dry EDM milling was found desirable for the EDM finishing operation and the effects of dielectric fluids, electrode materials and discharge parameters were categorized with extensive experimental investigation.
- An integrated process of dry EDM roughing and near-dry EDM finishing was demonstrated to achieve a mirror-like surface finish with 0.09 µm R_a. It can be a potential upgrade of PMD EDM process in ultra-fine surface finish machining with much lower dielectric fluid cost and environmental concern.

Modeling of anode discharge crater formation

- A model for the discharge crater formation on anode electrode was constructed. The bubble collapsing phase with complex multi-phase interactions among dielectric fluid, bubble, molten material and solid workpiece was modeled.
- The model constructed using FLUENT software was proven feasible by comparing with experimentally measured crater diameter and depth.
- The model was applied to prove the advantage of near-dry EDM over wet EDM in generating smooth craters and better surface finish.

The research on the dry and near-dry EDM milling processes opens up the area of exploring non-conventional EDM dielectric medium and implementing the EDM milling configuration. The effort on the discharge crater modeling provides the opportunity to simulate more realistic discharge crater enabling better understanding of the material removal mechanism in EDM and thus better process prediction, control and optimization.

5.2. Recommendations for Future Studies

With the exploratory work carried out in this research, several future studies can be suggested in the area of dry and near-dry EDM processes optimization and the area of EDM process modeling.

Study can be continued to exploit the liquid-gas dielectric fluid for the near-dry EDM. On one hand, new liquid and gas contents can be tested for the purposes of machining performance enhancement and as well as machined surface modification. For instance, since it is found that the rapid oxidation is beneficial for the high MRR, dielectrics that promote oxidation can be formulated and tested for EDM roughing process. Dielectrics and electrodes with special material compositions may be utilized for surface alloying and modification. Similar practice has been successfully carried out by Yan et al. (2005), Wang et al. (2002) and Mohri et al. (1993) in conventional wet EDM process. It is worthwhile to explore this potential in near-dry EDM considering its flexibility to mix different liquid and gas fluids. On the other hand, since the liquid-gas percentage has observable effect on the machining performance, characterization of this effect can be conducted using a better liquid-gas dispenser of more accurate flow rate control such that process can be customized by tailoring the liquid-gas percentage depending on the machining requirement.

More efforts are needed in the tool wear characterization and compensation for the precision application of near-dry EDM milling process. Since high electrode wear ratio, > 50% for the current finest finishing operation, takes place as a natural of the EDM finishing, the algorithm and system to detect, predict and compensate the tool wear will be essential for the successful application of EDM milling. An on-line electrical discharge pulse monitoring system and an adaptive control algorithm may be needed for this purpose. The material removal on both the workpiece and tool electrode is realized by individual electrical discharges and hence by the number of discharge pulses should have a correlation with the amount of tool wear. In addition, the material removal per pulse varies with the discharge parameter setting, the workpiece and electrode material combination and even the discharge conditions. Therefore, an algorithm, probably semi-empirical based, able to adapt to varied machining conditions will be of large value to provide good predication on the material removal per pulse and thus predict and compensate the electrode wear accurately.

It is also suggested to further supplement and expand the crater formation model. The individual crater formation model is considered potential to help realize the continual EDM process modeling by utilizing the realistic crater geometry and debris particles attained through the simulation. In continual EDM, the consecutive discharge depends on the electric field distribution and is initiated at the spot experiencing the highest field strength. The electric field is influenced by the debris distribution in the discharge gap and the morphology of anode and cathode's surfaces since insertions in the field and abrupt geometries of the electrodes can cause the electric field distortion to locally strengthen the field, and they are considered the major factors to determine the location and condition (spark, arc, or short circuit) of the consecutive discharge (Luo, 1997). Hence, by using the simulated crater geometry to update the machining surface topography and use the simulated debris particles to calculate the debris distribution through CFD or statistical analysis, the electric field distribution can be simulated after each discharge to determine the location and possibly condition (spark, arc, or short circuit) of the following discharge. The topology of the discharge location can thus be updated by geometric morphing of the crater geometry, which can be categorized into different shape depending on the discharge condition (spark, arc, or short circuit). Iterating this procedure, a continual EDM process can be simulated with the capability of predicting the material removal rate (MRR) and the machined surface topography.

Each of these suggested future topics can be used to further enhance the understanding and control of the EDM process and contribute to increasing the productivity and quality of EDM at lower cost.

APPENDIX

APPENDIX

CHARACTERIZATION OF EDM SURFACE AND SUBSURFACE PROPERTIES

A.1. Introduction

In EDM, the electrical discharge spot experiences a rapid melting and re-solidification cycle leaving the EDM machined surface a layer of thermally affected zone. The micro structure, chemical composition and consequently mechanical properties of the EDM surface layer differ from the substrate material.

On the very top of the thermally affected zone is the recast layer, which is composed of re-solidified material. The formation of the recast layer experiences high temperature gradients in both time and space domains. It makes the recast layer possess extremely fine and dense micro-structure as well as tensile thermal stress. High thermal stress can induce porosities and micro cracks (Abu Zeid, 1997). These surface defects can cause stress concentration and deteriorate the mechanical properties and the fatigue resistance of the machined part. Chemical reaction and material transfer can also occur under the high temperature, 4000 to 8000 K (Natsu et al., 2004), thus altering the chemical composition of the EDM surface. In cutting carbon steel, Kruth et al. (1995) observed an increase of carbon content (about 4 times) in the recast layer when using hydrocarbon dielectric; while a decrease in carbon content (up to 50%) is detected when using water dielectric. Change of the carbon content in steel influences the mechanical properties, such as hardness, surface friction coefficient and toughness. Kulkarni et al. (2005) detected the diffusion of hydrogen into the workpiece during EDM using deionized water , which can reduce the ductility of steel and cause premature material failures (Gabe, 2001). Soni et al. (1996) confirmed the existence of material migration from the tool electrode to workpiece.

Therefore, characterization of the machined surface properties is desirable for a comprehensive understanding of the dry and near-dry EDM milling processes. In this study, efforts were made to inspect the recast layer, micro hardness, material composition and residual stress of the EDM surface.

A.2. Experimental Setup

The surfaces generated in Chapter 3 at five different dry and near-dry EDM conditions, R2, R5, F10, F5 and F1 (Table 3.3), are investigated. The first two machining steps (R2, R5) are oxygen-assisted dry EDM and the following three steps (F10, F5, F1) are near-dry EDM finishing using kerosene-air mixture.

A.2.1. Sample preparation

The workpiece material used in the investigation is DMD deposited H13 tool steel. The top- and sub-surface properties of the machined surfaces are investigated. The top surfaces are examined as-is after machining. The sub-surface properties are inspected by looking at the cross sections of the machined surface. The sample is sectioned axially using diamond saw, coated with Ni on the top surface and mounted using epoxy. The Ni coating helps to preserve the top brittle recast layer which can otherwise easily peel off during the preceding polishing process. The cross section polishing starts with a sand paper of 400 grid and gradually down to 2400 grid, and then the 1 μm Al_2O_3 suspension solution is used for the fine polishing. Chemical etching with 5% nitric acid diluted in ethanol is then conducted to reveal the micro structure of the material.

A.2.2. Analysis equipment and procedure

The recast layer is observed using an Olympus PME3 optical microscope and a Philips XL30 FEG scanning electron microscope (SEM). Both the top and cross section of the machined surface are inspected

The micro hardness analysis is conducted using a MTS NanoIndenter II indentation equipment. A 2000 μN indentation force is applied resulting in an indent with depth around 100 nm and size around 1 μm. A 3 × 6 array of indents are made along the cross section from the top surface to the substrate with six steps vertically and three replicates laterally. The first indent is made approximately 2 μm beneath the top surface and the vertical increment is 15 μm for the R2 and R5 surfaces and 7 μm for F10 surfaces. For F5 and F1 surfaces, the recast layer is thin (< 1.5 μm), it is difficult to place the indents right inside the layer to attain consistent measurement. Indentation is therefore conducted on the top surfaces for the F5 and F1 surface to attain the micro hardness of the recast layers.

The material composition analysis is conducted with an EDAX energy dispersive spectroscope (EDS) attached to the Philips XL30FEG SEM. The possible elements exist in the material are first identified and the weight percentage of each element is approximated from the material spectrum. The composition of the base material is first analyzed and used as the reference value. The result is listed in Table A.1. The compositions of the machined surface and subsurface are then inspected and the weight percentage of each element is divided by the reference value in Table A.1 to attain the normalized weight percentage of each element. The decrease and increase of the material composition is thus presented by the normalized weight percentage lower and higher than 1, respectively.

Table A.1. Material composition of DMD H13 from EDS measurement.

Element	Element Wt. %
C	0.3 ± 0.07
V	2.43 ± 0.58
O	0.47 ± 0.13
Si	0.75 ± 0.07
Mo	0.67 ± 0.01
Cr	2.09 ± 0.06
Fe	93.29 ± 0.61

The surface residual stress analysis was conducted using a Bruker Discover D8 X-ray diffraction (XRD) system. The most widely used $\sin^2\psi$ method was applied as a nondestructive method for the stress evaluation (Cullity, 1959).

In the XRD stress measurement, the strain accompanied by the residual stress distorts the lattice plane and results in the change of the lattice spacing, d, which shifts the material's diffraction angel, 2θ, when X-ray is applied. For a stressed surface, the 2θ angel varies with different X-ray incident angle, ψ. According to the elasticity theory (Saada, 1993), the difference between $2\theta_n$ and $2\theta_i$, which are the diffraction angle in the normal direction ($\psi = 0$) and inclined direction ($\psi = \psi$), respectively, holds a relationship with the surface stress, σ_φ, as shown in Figure A.1. Therefore, with the relationship as of

$$\begin{cases} \sigma_\varphi = K(2\theta_n - 2\theta_i) \\ K = \dfrac{E\cot\theta}{2(1+\nu)\sin^2\psi} \end{cases} \tag{A.1}$$

where, K is the stress factor, E is Young's Modulus of the testing material, v is Poisson's Ratio of the testing material, and θ is the unstressed material's diffraction angel, the σ_φ can be attained by applying X-ray measurement in the nominal direction and inclined direction.

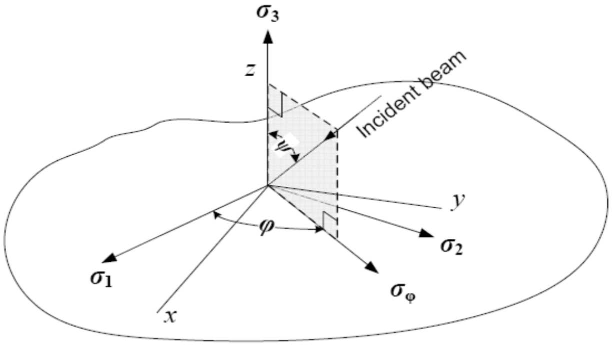

Figure A.1. Schematics of XRD residual stress measurement (Cullity, 1959).

In the residual stress measurement, only the final-finished mirror-like surface was evaluated because other surfaces are rough and can diffract the incident X-ray in diverged directions thus introducing extra measurement noise. Methods other than XRD should be applied if accurate measurement is needed for those rough surfaces.

A.3. Experimental Results

A.3.1. Recast layer observation

Formed during a rapid melting and solidification cycle, the recast layer is usually brittle and has micro-cracks induced by the thermal stress. Depending upon the application, post processes are needed to remove the recast layer and sometimes the heat affected zone beneath it to avoid the detrimental effect it could have.

Figure A.2 shows the cross section and top views of the five dry and near-dry EDM surfaces in sequence from roughing to finishing (R2, R5, F10, F5 and F1). From the cross sections, the recast layer is distinguished from the base material as a white layer on the top. The white and grey color contrast in the base material indicates the micro structure of two different phases, martensite and austenite, in the DMD H13 tool steel (Ghosh and Choi, 2006). In contrast to the micro structure of the base material, no clear pattern of micro structure is observed in the recast layer because the rapid cooling rate, higher than 10^9 K/s as observed in Chapter 4, during the layer formation prohibits the growth and development of the micro structure. The short discharge duration, less than 2μs, allows an extremely short heating cycle and correspondingly short cooling cycle which suppresses the growing of the micro structure. The supercooled liquid metal is found to exhibit an amorphous glass structure (Reed-Hill and Abbaschian, 1994) and hence it can be the micro structure in the recast layer. To determine the exact micro structure, the transmission electron microscopy (TEM) can be used to analyze the diffraction pattern of the recast material.

Figure A.4 shows the measured recast layer thickness. From the first step roughing process to final finishing process, the recast layer thickness reduces from 14 ± 4 μm to 1.5 ± 0.2 μm. The recast layer becomes thinner and smoother through the transition. It is in accordance with the fact that lower discharge energy generates shallower discharge crater and better surface finish.

In addition, from the top views in Figure A.2, it is seen that the surface features becomes finer and finer from roughing to finishing operations. In the surfaces machined by R2 (Step 1) and R5 (Step 2), micro cracks are easily observed as a result of the strong thermal stress. For F10 (Step 3) machined surface, visible micro cracks have been reduced considerably. Micro cracks are no longer dominant features on the recast layer surface. For the last two finishing steps by F5 (Step 4) and F1 (Step 5), very fine surface features are attained with distinguishable individual discharge craters and without signs of cracks. Low discharge power density reduces the temperature gradient and thermal stress and thus helps to relieve the surface from defects.

In general, better surface integrity and less impact from the EDM process are observed in terms of the recast layer morphology from the roughing to finishing EDM processes.

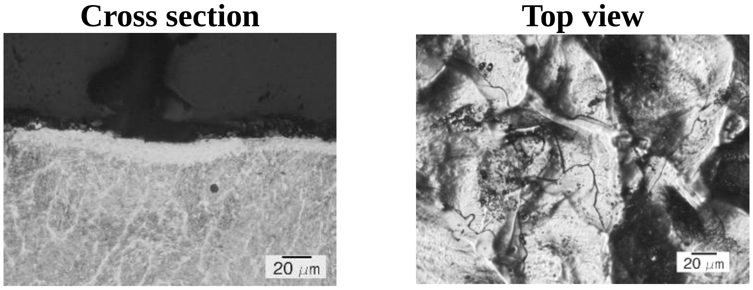

R2 (Step 1)

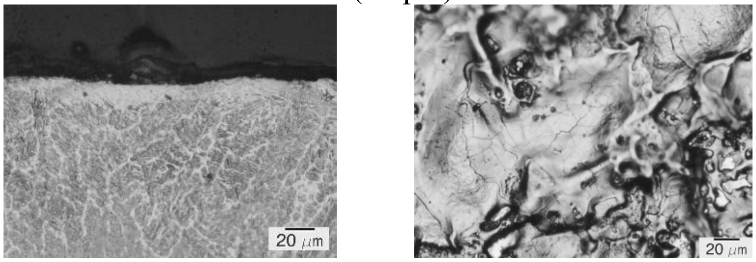

R5 (Step 2)

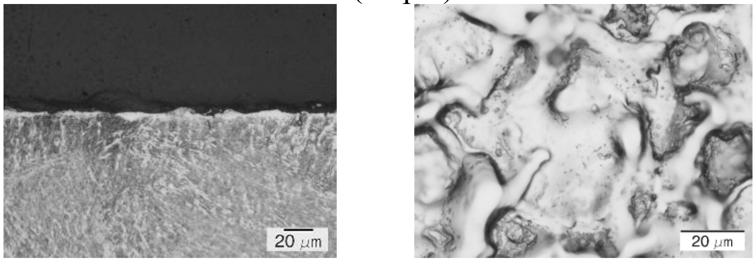

F10 (Step 3)

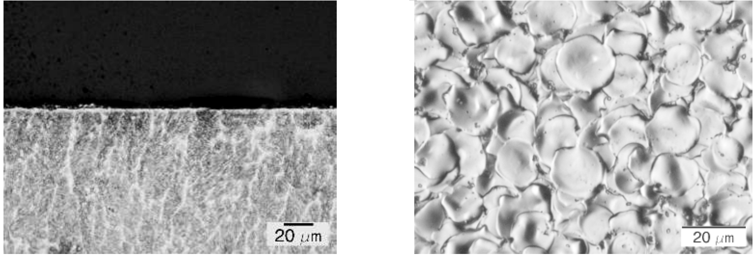

F5 (Step 4)

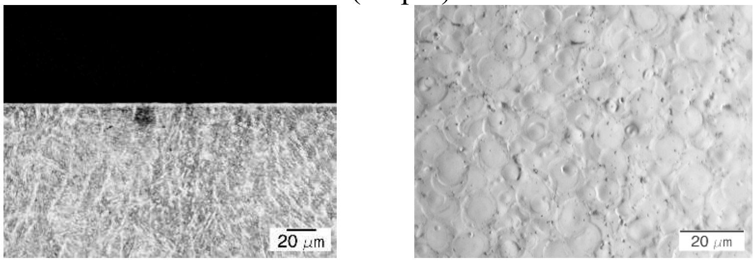

F1 (Step 5)

Figure A.2. Section and top views of the EDM surfaces.

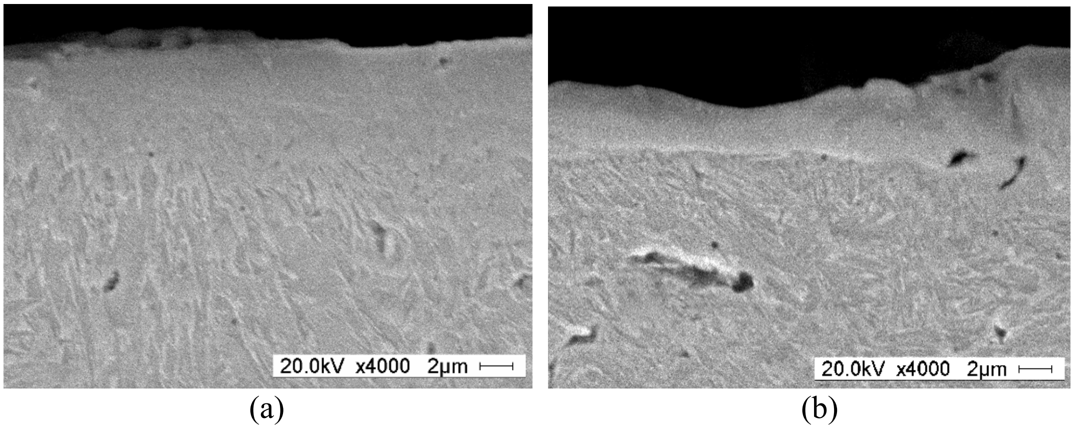

(a) (b)

Figure A.3. Cross sections observed at high magnification, (a) surface generated at Step 2 and (b) surface generated at Step 3.

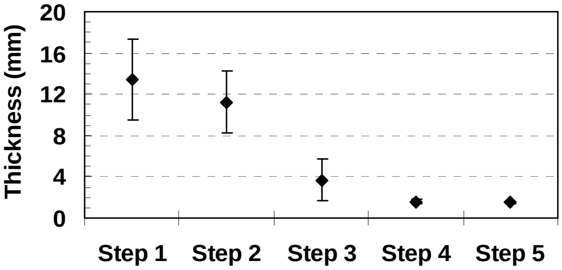

Figure A.4. Summarized recast layer thickness for different machining steps.

Beneath the recast layer, the observation of heat affected zone has been reported (Bleys et al., 2006). The heat affected zone is the layer experiences the "heat treat" during the electrical discharge but does not go through the melting and solidification cycle. It is reported to have finer micro structure than the base material. However, no distinguishable size transitioning of the micro structure has been observed in the investigated surfaces, as in Figure A.3. It can be because the low discharge duration (no longer than 5 μs for all five machining steps) does not allow the heat to penetrate in depth and modify the microstructure. However, simply from the micro structure observation it is not evident enough to say that the impact of EDM process is limited to the recast layer.

The evaluation of micro hardness and material composition helps to further reveal the surface and subsurface properties.

A.3.2. Nano-indentation

The nano-indentation is conducted on the cross section of the workpiece in the direction from the top surface to the substrate. The measured micro-hardness in GPa versus the distance from the top surface is shown in Figure A.5. The base material micro hardness is about 4.5 to 5.0 GPa.

For the surface machined by R2 (Step 1), the peak hardness near the top surface is very high, about 11 GPa. Transitioning towards the substrate, the effect of cooling rate and alloying diminishes and the hardness value gradually decreases. The micro hardness returns to the base material level at 45 μm beneath the top surface. Since the recast layer is about 9 to 17 μm (Figure A.4), it indicates the heat affect zone does exist with the increase of micro hardness but could not be seen using the nitric acid etchant.

For the surface machined by R5 (Step 2), the peak micro-hardness is about the same (11 GPa) but the depth of high micro-hardness is reduced to less than 16 μm, slight larger than the recast layer thickness (Figure A.4).

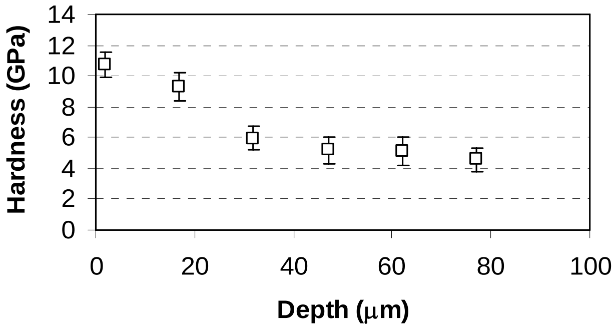

(a) Step 1

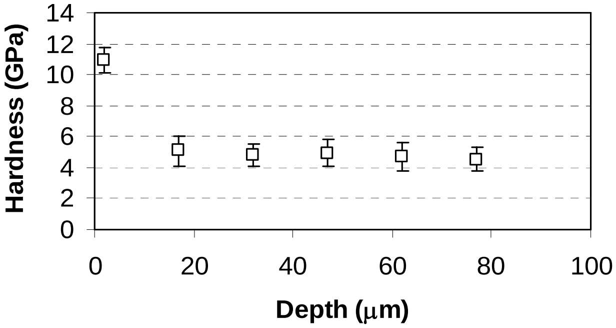

(b) Step 2

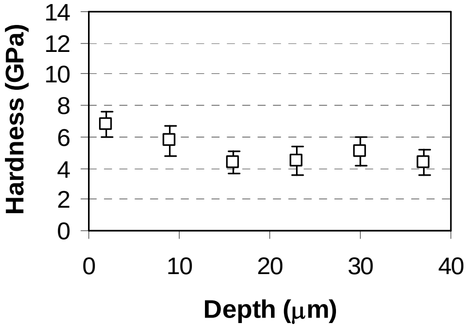

(c) Step 3

Figure A.5. Measurements of micro hardness for machining steps R2, R5 and F10.

For the finishing EDM process F10 (Step 3), the increase in peak hardness (to 7 GPa) and the depth of hardened layer (about 10 μm) are not high.

For surfaces machined by F5 and F1 (Steps 4 and 5), the nano indents are applied directly on the top of the machined surface. The measured micro hardness of the recast layer is 9.3 ± 2.9 and 9.1 ± 1.5 GPa for F5 and F1 surfaces, respectively. The average micro hardness of the recast layer in finishing EDM is high. The measurement variation is larger than that of the cross-sectional measurement because the top surface is composed of overlapped discharge craters and is rougher than the polished cross section surface.

For all the EDM surfaces, dramatic increase of the micro hardness is observed in the recast layer. This is first attributed to the unique dense micro structure of the recast layer. The second reason is the material composition change (increase of carbon and oxygen contents) and is discussed in the next section.

A.3.3. Material composition analysis

Figure A.6 shows the material composition information for surfaces generated under the five machining steps (R2, R5, F10, F1 and F5). The normalized weight percentage of each material element is presented to characterise the variation of material composition at different depths from the machined surface.

For R2 and R3 (Step 1 and Step 2) machined surfaces, significant increase of carbon and oxygen contents are observed in Figure A.6. The oxygen increases about 18 times and the carbon content increases about 7 times on top of the machined surface. The layer that experiences material composition change is less than 5 μm and 3 μm in depth for R2 and R3 surfaces, respectively. This is thinner than the recast layer thickness. It is considered the material composition change is only limited within the recast layer. Figures A.7(a) and (b) compare the EDS spectrums of the base material and the machined surface after EDM roughing. The peak rise of the oxygen and carbon elements indicates the increase of these two material compositions. The peak oxygen composition on top of the machined surface is more than 10 times of that in the base material. The increase of oxygen is due to the oxygen machining medium and the oxidation process that promotes the immigration of oxygen content during the EDM. The increase of carbon content is subject to debate since there is no external source of carbon in the roughing process except for the carbon in the original material (less than 1%). A possible explanation is that rearrangement of carbon distribution happens during the material melting and solidification process. The low molecular weight carbon content floats up and accumulates at the upper part of the recast layer.

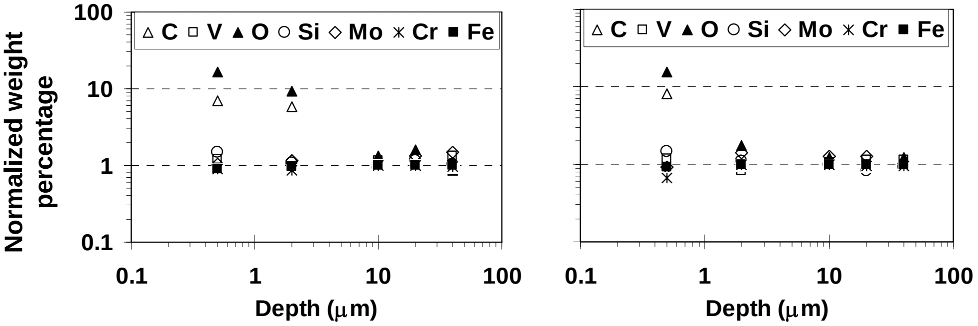

R2 (Step 1)

R5 (Step 2)

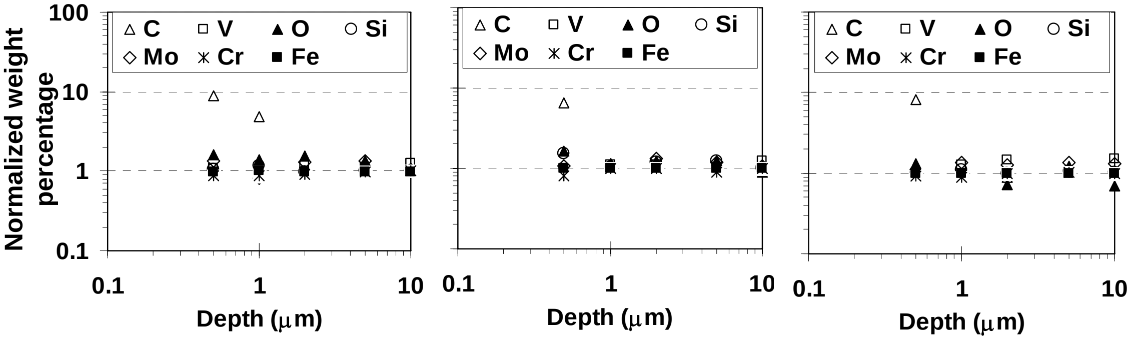

F10 (Step 3) F5 (Step 4) F1 (Step 5)

Figure A.6. Material composition results for five EDM conditions.

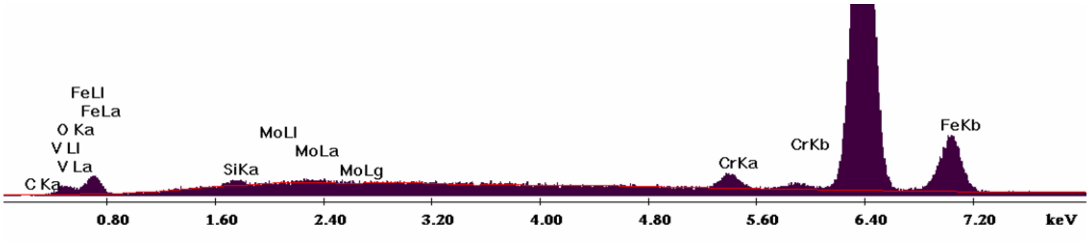

(a) Original material

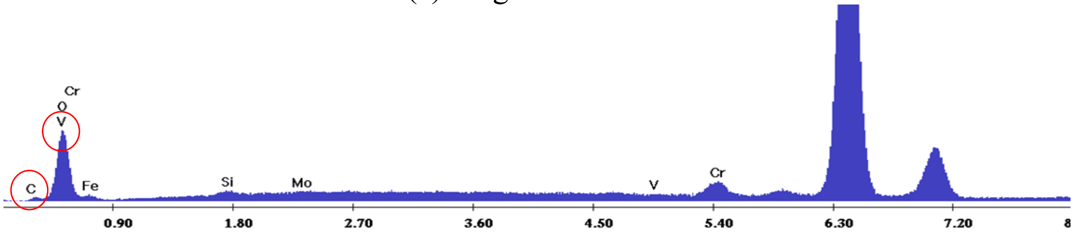

(b) Machined surface after dry EDM roughing using oxygen

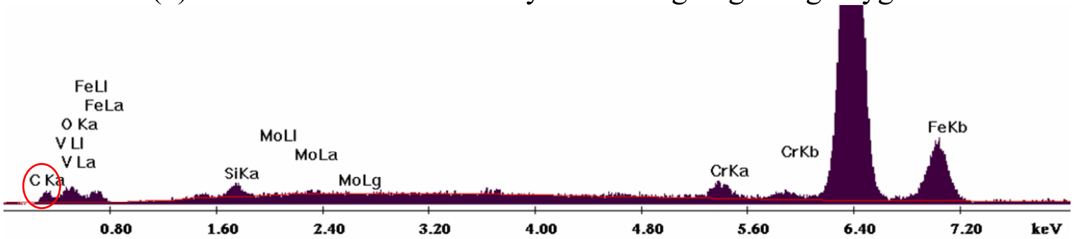

(c) Machined surface after near-dry EDM finishing using kerosene-air mixture

Figure A.7. EDS spectrums of H13 tool steel under before and after EDM roughing and finishing processes.

The increase of oxygen and carbon contents both help to raise the material micro hardness. Increase amount of carbon can help enhance the hardenability and surface wear resistance of the steel material (Kruth et al., 1995) and the oxygen element makes the material hard but also brittle (Emsley, 1998). In addition, the exhibition of additional carbon and oxygen element also indicates the loss of base material elements due to decomposition and vaporization. The loss of chromium is the most significant and it can reduce the corrosion resistance of the machined surface. Certain loss of iron element is also observed.

For the surface generated by F10, F5 and F1, the increase of carbon content (about eight times of increase) is the most significant. In Figure A.5, the carbon composition is observed to increase to about 8 times of the base material composition. Since the near-dry EDM uses kerosene-air mixture, the additional carbon content should come from the decomposed kerosene, a type of hydrocarbon oil (Kruth et al. 1995). The layer that has increased carbon content is about 2 μm thick for F10 machined surface and less than 1 μm thick for F5 and F1 machined surfaces. The increase of the carbon content helps to raise the micro hardness of the recast layer.

A.3.4. Surface residual stress analysis

Figure A.8 shows a pair of XRD spectrums with different beam incident angles, ψ, and the shift of the diffraction angle, 2θ, has been observed. Based on the 2θ shift and Equation A.1, the surface residual stress can be calculated.

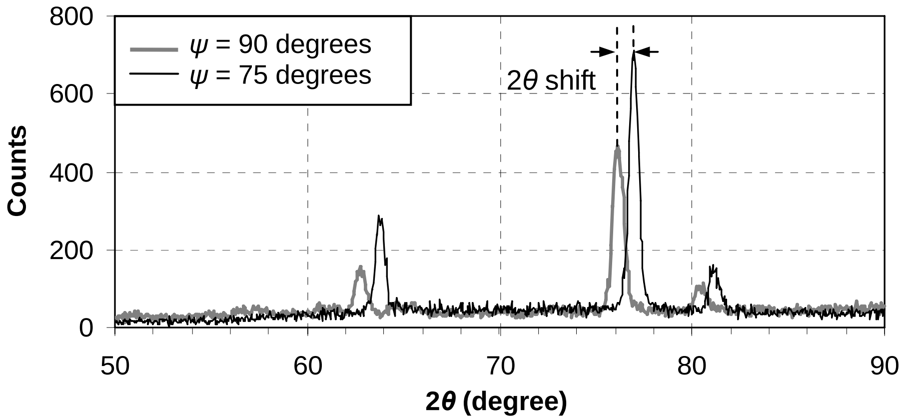

Figure A.8. XRD spectrums measured at different beam incident angles.

The calculated stress is 467 ± 561 MPa. It noticed that the result has an abnormally large variation, which makes the measurement range varies between the yield stress of the material and the compressive stress region. It obviously does not give an accurate judgement on the residual stress status even though the recognition of tensile stress is in accordance with the expectation.

The large variation is in fact caused by the limitation of the available XRD equipment. Assuming the measurement error only comes from the 2θ identification, the variance of the stress measurement, $\sigma^2(\sigma_\varphi)$, can be attained by applying variance analysis on Equation A.2:

$$\sigma^2(\sigma_\varphi) = K^2(\sigma^2(2\theta_n) + \sigma^2(2\theta_i)) \quad \text{(A.2)}$$

, where $\sigma^2(\sigma_\varphi)$ and $\sigma^2(\sigma_\varphi)$ are the variance in $2\theta_\mathrm{n}$ and $2\theta_\mathrm{i}$ measurement, respectively, and K is considered as constant since it only depends on the unstressed material properties and the setting of ψ, which is fixed in each measurement and we assume a good repeatability for each repositioning of ψ. Equation A.2 shows that small measurement variation can be achieved given high precision 2θ identification and small K value. The XRD equipment has a minimum θ positioning resolution of 0.02 degree, which is of general XRD application capacity, and thus the best precision can be achieved for 2θ identification is 0.04 degree. From Equation B.1, the K for a specific testing material is known dependant on θ and ψ. Large θ and large ψ helps yield small K. For stress measurement, the ψ angle should ideally vary from 0 to 90 degrees while the maximum ψ of the current equipment is 20 degrees. As to θ, it is the theoretical diffraction angle of the unstressed material and is determined by the Bragg Law:

$$\sin\theta = \lambda / 2d \quad \text{(A.3)}$$

, where d is the lattice spacing of the reflection plane, which is the property of the unstressed material and varies with the plane index, and λ is the wavelength of the incident X-ray, which is determined by the target material of X-ray generation. To inspect ferritic and martensitic steel workpiece, the combinations of (211) plane and Cr target or (220) plane and Co target are recommended (Bruker AXS Inc., 1999). However, Cu is the only target available with the current XRD equipment. The Cu target generates X-ray wavelength shorter than that from Cr and Co, and results in smaller θ. Combining all these factors, the stress measurement error under varied target materials and ψ settings can be estimated from the variance calculation in Equation A.2. Table A.1 summarises the estimation results. It is seen that the current XRD setup, Cu target, on (221) plane of the testing material and 20 degrees of ψ, yields unacceptably large measurement error, nearly 800 MPa. Hence, further study is recommended to achieve better residual stress measurement by using XRD system that can provide longer wavelength X-ray and larger ψ angle adjustment or alternative methodologies for residual stress measurement, such as neutron diffraction, blind-hole drilling, etc.

Table A.2. Estimation of stress measurement error (MPa).

Target material / **ψ (degree)**	Cu, (211)	Co, (200)	Cr, (211)
20	784	362	145
50	156	72	29
90	92	42	17

A.4. Concluding Remarks

In this chapter, the effect of dry and near-dry EDM processes on the machined surface properties, including recast layer morphology, micro hardness and material composition were characterized. The recast layer exhibits no clear pattern of micro structures. Micro cracks were observed to exist on the surfaces generated by the roughing processes and diminish in the finishing process. The recast layer thickness was reduced from roughing to finishing processes. High micro hardness was observed on the EDM surface. The micro hardness in the recast layer was found to be twice of that in the base material. The unique micro structure and material composition change are attributed to the intensive micro hardness increase. The layer of increased hardness extends beneath the recast layer indicating the existence of heat affected zone on the EDM surface. The material composition change was detected on the EDM surface and only limited within the recast layer. The oxygen and carbon contents were increased in the surfaces machined by dry EDM using oxygen. The carbon content was increased on the surfaces generated by near-dry EDM using kerosene-air mixture.

As transitioning towards the finishing process, the surface integrity improves and the impact of is reduced on the material properties change. The material layer affected by the EDM process is less than 2 μm in thickness for the finest finished surface (by F1).

Tensile residual stress was detected on the final finished surface but the exact stress value cannot be determined due to the equipment limitation. XRD system with long X-ray wavelength and large ψ adjustment was found desirable to achieve accurate measurement.

BIBLIOGRAPHY

BIBLIOGRAHPY

Abu Zeid, O.A. (1997) On the effect of electrodischarge machining parameters on the fatigue life of AISI D6 tool steel, Journal of Materials Processing Technology 68 (1) 27-32.

Albinski, K., Musiol, K., Miernikiewicz, A., Labuz, S., Malota, M. (1995) Plasma temperature in electro discharge machining, Proceedings of ISEM XI 143-152.

Arunachalam, C. (1995) Modeling the electrical discharge machining process, PhD Dissertation, Texas A&M University, 4.

ASTM A681-94 (2004) Standard Specification for Tool Steel Alloy, ASTM International, West Conshohocken, PA.

Avallone, E.A., and Baumeister, T. (1996) Standard Handbook for Mechanical Engineers, 10th Ed., McGraw-Hill, New York, NY, 4-82.

Bleys, P., Kruth, J.P., and Lauwers, B. (2004) Sensing and compensation of tool wear in milling EDM, Journal of Materials Processing Technology 140 139-146.

Bleys, P., Kruth, J.P., Lauwers, B., Schacht, B., Balasubramanian, V., Froyen, L., Van H. (2006) Surface and sub-surface quality of steel after EDM, Advanced Engineering Materials, 8 (1-2) 15-25.

Bruker AXS Inc. (1999) GADDS User Manual, Madison, WI, 6-10.

Carrano, A.L., Mehta, B., Low, J.C. (2004) Response surface methodology of die-sink electro-discharge machined surfaces, IIE Annual Conference and Exhibition 2004, IIE Annual Conference and Exhibition 2004 787-792.

Chen, Y., Mahdivian, S.M. (2000) Analysis of electro-discharge machining process and its comparison with experiments, Journal of Materials Processing Technology 104 (1) 150-157.

Childs, T.H.G., Hauser, G., Badrossamay, M. (2005) Selective laser sintering (melting) of stainless and tool steel powders: experiments and modeling, Proceedings of the Institutions of Mechancial Engineers, Part B: Journal of Engineering Manufacture 219 339-357.

Coelho, R. (1979) Physics of dielectrics for the engineer, Elsevier Scientific Publishing Company 97-101, 159.

Cornell, R.M., Schwertmann, U., The Iron Oxides, 2nd edition, Wiley-VCH Verlag GmbH & Co. KGaA, Weinheim, 2004.

Curodeau, A., Marceau, L.F., Richard, M., Lessard, J. (2005) New EDM polishing and texturing process with conductive polymer electrodes, Journal of Materials Processing Technology 159 (1) 17-26.

Curodeau, A., Richard, M., Frohn-Villeneuve, L. (2004) Molds surface finishing with new EDM process in air with thermoplastic composite electrodes, Journal of Materials Processing Technology 149 (1-3) 278-283.

Das, S., Koltz, M., Klocke, F. (2003) EDM simulation: finite element-based calculation of deformation, microstructure and residual stress, Journal of Materials Processing Technology 142 434-451.

DiBitonto, D.D., Eubank, P.T., Patel, M.R., Barrufet, M.A. (1989) Theoretical models of the electrical discharge machining process. I. A simple cathode erosion model, Journal of Applied Physics 66 (9) 4095-4103.

Eckman, P.K., Williams, E.M. (1960) Plasma dynamics in an arc formed by low-voltage sparkover of a liquid dielectric, Applied Science Research Section B 8 299-320.

Egashira, K., Matsugasako, A., Tsuchiya, H., Miyazaki, M. (2006) Electrical discharge machining with ultra-low discharge energy, Precision Engineering 30 (4) 414-420.

Emsley, J. (1998) The Elements, 3r ed., Clarendon Press 148-149.

Eubank, P.T., Patel, M.R., Burrufet, M.A. and Bozkurt, B. (1993) Theoretical models of the electrical discharge machining process. III. The variable mass, cylindrical plasma model, Journal of Applied Physics 73 7900-7909.

Fallbohmer, P., Altan, T., Tonshoff, H.-K., Nakagawa, T. (1996) Survey of the die and mold manufacturing industry - practices in Germany, Japan, and the United States, Journal of Materials Processing Technology 59 (1-2) 158-168.

Fallbohmer, P., Rodriguez, C.A., Ozel, T., Altan, T. (2000) High-speed machining of cast iron and alloy steels for die and mold manufacturing, Journal of Materials Processing Technology 98 (1) 104-115.

FLUENT 6.3 User's Guide, Fluent Inc., 2006.

Forsythe, W.E. (2003) Smithsonian Physical Tables, Knovel, Norwich, NY, 322.

Gabe, D.R. (2001) Hydrogen embrittlement from metal finishing processes, Transactions of the Institute of Metal Finishing 79 (5) B78-B80.

Gerasimov, A.I. (2005) Water as an insulator in pulsed facilities, Instruments and Experimental Techniques 48(2) 141–167.

Golladay J. (2006) Iron oxide, http://web1.caryacademy.org/chemistry/rushin/StudentProjects/CompoundWebSites/2003/ironoxide/home.htm, as on Aug. 27, 2006.

Ghosh, S., Choi, J. (2006) Modeling and experimental verification of transient/residual stresses and microstructure formation of multi-layer laser aided DMD process, Journal of Heat Transfer 128 (7) 662-679.

Grosvenor, A.P., Kobe, B.A., McIntyre, N.S. (2005) Activation energies for the oxidation of iron by oxygen gas and water vapour, Surface Science (574) 317-321.

Han, L., Liou, F.W., Musti, S. (2005) Thermal behavior and geometry model of melt pool in laser material process, Transactions of ASME, Journal of Heat Transfer 127 1005-1014.

Hashimoto, G., Kunieda, M. (1997) Spectroscopic analysis of temperature variation of EDM arc plasma, Journal of JSME B 31 32-40 (in Japanese).

Hockenberry, T.O., Williams, E.M. (1967) Dynamic evolution of events accompanying the low-voltage discharge employed in EDM, IEEE Trans. on Industry and General Applications, IGA-3 (4) 302-309.

Imai, Y., Hiroi, M., Nakano, M. (2001) Investigation of EDM machining states using ultrasonic waves, ISEM 13 109-116.

Incropera, F.P., DeWitt, D.P. (2007) Introduction to Heat Transfer, 5th Ed., Wiley, Hoboken, NJ, 102-111.

Jeswani, M.L. (1980) Electrical discharge machining in distilled water, Microtecnic (3) 31-35.

Jilani, S., Tariq, Pandey, P.C. (1984) Experimental investigation into the performance of water as dielectric in EDM, International Journal of Machine Tool Design & Research 24 (1) 31-43.

Kansal, H.K., Singh, S., Kumar, P. (2005) Parametric optimization of powder mixed electrical discharge machining by response surface methodology, Journal of Materials Processing Technology 169 (3) 427-436.

Kao, C.C., Tao, J., Lee, and Shih, A.J. (2006) Dry wire electrical discharge machining of thin workpiece, Transactions of NAMRI/SME 34 253-260.

Kao, C.C. and Shih, A.J. (2006) Sub-nanosecond monitoring of micro-hole electrical discharge machining pulses and modeling of discharge ringing, International Journal of Machine Tools and Manufacturing 46 1996-2008.

Kao, C.C., Tao, J., Shih A.J. (2007) Near dry electrical discharge machining, International Journal of Machine Tools and Manufacture 47 2273-2281.

Klocke, F., Thomaidis, D., Garzon, M., Veselovac, D., Klink, A. (2007) Force measurements in the micro spark erosion with various electrode materials, polarities and working media, Proceedings of 15th International Symposium on Electromachining, ISEM XV, Pittsburgh, USA, 263-268.

Koenig, W., Wertheim, R., Zvirin, Y., Toren, M. (1975) Material removal and energy distribution in electrical discharge machining, Annals of the CIRP 24 (1) 95-100.

Kozak, J., Rozenek, M., Dabrowski, L. (2003) Study of electrical discharge machining using powder-suspended working media, Proceedings of the Institution of Mechanical Engineers, Part B (Journal of Engineering Manufacture) 217 (B11) 597-602.

Kruth, J.P., Stevens, L., Froyen, L., Lauwers, B. (1995) Study on the white layer of a surface machined by die sinking electro discharge machining, Annals of the CIRP 44 (1) 169-172.

Kulkarni, V.N., Jain, V.K., Shukla, A.K. (2005) Measurement of hydrogen content in electrical discharge machined components, Machining Science and Technology 9 (2) 289-299.

Kunieda, M., Furudate, C. (2001) High precision finish cutting by dry WEDM, CIRP Annals – Manufacturing Technology 50 (1) 121-124.

Kunieda, M., Furuoya, S. (1991) Improvement of EDM efficiency by supplying oxygen gas into gap, Annals of the CIRP 40 (1) 215-218.

Kunieda, M., Lauwers, B., Rajurkar, K.P., Schumacher, B.M. (2005) Advancing EDM through fundamental insight into the process, CIRP Annals - Manufacturing Technology 54 (2) 599-622.

Kunieda, M., Miyoshi, Y., Takaya, T., Nakajima, N., Yu, Z.B., Yoshida, M. (2003) High speed 3D milling by dry EDM, Annals of the CIRP 52 (1) 147-150.

Kunieda, M., Takaya, T., Nakano, S. (2004) Improvement of dry EDM characteristics using piezoelectric actuator, CIRP Annals – Manufacturing Technology 53 (1) 183-186.

Kunieda, M., Yoshida, M. (1997) Electrical discharge machining in gas, Annals of the CIRP 46 (1) 143-146.

Lauwers, B., Kruth, J.P., Liu, W., Eeraerts, W., Schacht, B., Bleys, P. (2004) Investigation of material removal mechanisms in EDM of composite ceramic materials, Journal of Materials Processing Technology 149 (1-3) 347-52.

Lasagni, A., Soldera, F., Mucklich, F. (2004) FEM simulation of local heating and melting during electrical discharge plasma impact, Modelling and Simulation in Materials Science and Engineering 12 835-844

Lazarenko, B.R. (1943) To invert the effect of wear on electric power contacts, Dissertation of The All-Union Institute for Electro Technique in Moscow/CCCP.

Leao, F.N., Pashby, I.R. (2004) A review on the use of environmentally-friendly dielectric fluids in electrical discharge machining, Journal of Materials Processing Technology 149 (1-3) 341-346.

Li, L., Wong, Y.S., Fuh, J.Y.H., Lu, L. (2001) Effect of TiC in copper-tungsten electrodes on EDM performance, Journal of Materials Processing Technology 113 (1-3) 563-567.

Li, L.Q., Wang, Z.L., Zhao, W.S. (2004) Mechanism analysis of electrical discharge machining in gas, Journal of the Harbin Institute of Technology, 36 (3) 359-62 (in Chinese).

Li, Y.B., Lin, Z.Q., Chen, G.L., Wang, Y.S., Xi, S.Y. (2002) Study on moving GTA weld pool in an externally applied longitudinal magnetic field with experimental and finite element methods, Modelling and Simulation in Materials Science and Engineering 10 781-798.

Luis, C.J., Puertas, I., Villa, G. (2005) Material removal rate and electrode wear study on the EDM of silicon carbide, Journal of Materials Processing Technology 164-165 (15) 889-96.

Luo, Y.F., Zhang, Z.Y. and Yu, C.Y. (1988) Mirror surface EDM by electric field partially induced, Annals of CIRP 37 (1) 179-181.

Luo, Y.F. (1997) Dependence of interspace discharge transitivity upon the gap debris in precision electrodischarge machining, Journal of Materials Processing Technology 68 (2) 121-131.

Luo, Y.F. (1998) An evaluation of spark mobility in electrical discharge machining, IEEE Transactions on Plasma Science 26 (3) 1010-1016.

Luo, Y.F. (1998) An investigation into the actual EDM off-time in SEA machining, Journal of Materials Processing Technology 74 61-68.

Luo, Y.F., Chen, C.G. (1990) Effect of a pulsed electromagnetic field on the surface roughness in superfinishing EDM, Precision Engineering 12 (2) 97-100.

Luo, Y.F., Tao, J (2008) Characterization of EDM craters involving secondary discharges on ferrous cathodic workpice, submitted to Journal of Materials Processing Technology

Manna, A., Bhattacharyya, B. (2006) Taguchi and Gauss elimination method: a dual response approach for parametric optimization of CNC wire cut EDM of PRAISiCMMC, International Journal of Advanced Manufacturing Technology 28 (1-2) 67-75.

Mazumder, J., Choi, J., Nagarathnam, K., Koch, J., Hetzner, D. (1997) Direct metal deposition of H13 tool steel for 3-D components, the Journal of the Minerals, Metals & Materials Society, 49 (5) 55-60.

Mazumder, J., Dutta, D., Kikuchi, N., Ghosh, A. (2000) Closed loop direct metal deposition: art to part, Optics and Lasers in Engineering 34 (4-6) 397-414

Metals Handbook, 9th edition, v3: Properties and Selection: Stainless Steels, Tool Materials and Special-Purpose Metals, ASM International, 1980.

Mohri, N., Saito, N., Narumiya,H., Kawatsu, Y., Otake, H., Tsunekawa, Y., Takawashi, T., Kobayashi, K. (1987) Study on finishing of large area workpiece by EDM. J. Japan Soc. Precision Engng 53 (1) 29–32.

Mohri, N., Saito, N., Takawashi, T., Takawashi, T. (1985) Mirror-like finishing by EDM, Proceedings of the 25th International Symposium on Machine Tool Design and Symposium, UK, 329–336.

Mohri, N., Satio, N., Higashi, M. (1991) A new process of finish machining of free surface by EDM method, Annals of CIRP 40 (1) 207-210.

Mohri, N., Saito, N., Tsunekawa, Y., Kinoshita, N. (1993) Metal surface modification by electrical discharge machining with composite electrode, CIRP Annals 42 (1) 219-222.

Montgomery, D.C. (2005) Design and Analysis of Experiments, 6th edition, John Wiley & Sons, Hoboken, NJ.

Murali, M.S, Yeo, S.H. (2005) Process simulation and residual stress estimation of micro-electrodischarge machining using finite element method, Japan Journal of Applied Physics 44 5254-5263

Narumiya, H., Mohri, N., Saito, N., Ootake, H., Takawashi, T., Kobayashi, K. (1987) Finishing on the large area of work surface by EDM, Journal of Japan Society of Precision Engineering 53 (1) 124–130.

Narumiya, H., Mohri, N., Saito, N., Ootake, H., Tsunekawa, Y., Takawashi, T., Kobayashi, K. (1989) EDM by powder suspended working fluid, Proceedings of 9th International Symposium on Electromachining (ISEM IX) 5–8.

NASA (1985) Inert-gas electrical-discharge machining, NTIS Tech Note.

Natsu, W., Ojima, S., Kobayashi, T., Kunieda, M. (2004) Temperature distribution measurement in EDM arc plasma using spectroscopy, JSME International Journal C 47 (1) 384-390.

Natsu, W., Shimoyamada, M., Kunieda, M. (2006) Study on expansion process of EDM arc plasma, JSME International Journal, Series C 49 600-605.

Okada, A., McGeough, J.A., MacMillan, D., Flynn, B. (2006) Machining characteristics of EDM by radio-frequency plasma, Annals of CIRP 55 (1) 167-170.

Reed-Hill, R., Abbashian R. (1994) Physical Metallurgy Principles, PWS Publishing Company, Boston, 427-428.

Robinson, J.W. (1973) Finite-difference simulation of an electrical discharge in water, Journal of Applied Physics 44 76-81.

Pandit, S.M., Rajurkar, K.P. (1980) Data dependant systems approach to EDM process modeling from surface roughness profiles, Annals of the CIRP 29 (1) 107-112.

Pandit, S.M., Venkatapathy, B., Rajurkar, K.P. (1983) Stochastic approach to thermal modeling applied to electro-discharge machining, Journal of Heat Transfer, Transactions ASME, 105 (3) 555-562.

Patel, M.R., Barrufet, M.A., Eubank, P.T., DiBitonto, D.D. (1989) Theoretical models of the electrical discharge machining process. II. The anode erosion model, Journal of Applied Physics 66 (9) 4104-4111.

Peyton, K.B. (2002) Ondeo/Nalco Fuel Field Manual, McGraw-Hill, New York, NY, 112.

Pecas, P., Henriques, E. (2003) Influence of silicon powder-mixed dielectric on conventional electrical discharge machining, International Journal of Machine Tools and Manufacture 43 (14) 1465-1471.

Puertas, I., Luis, C.J., Villa, G. (2005) Spacing roughness parameters study on the EDM of silicon carbide, Journal of Materials Processing Technology (164-165) 1590-1596.

Qu J., Shih, A.J., Scattergood, R.O., Luo J. (2005) Abrasive micro-blasting to improve surface integrity of electrical discharge machined WC-Co composite, Journal of Materials Processing Technology 166 (3) 440-448.

Rampling, K. (2000) Spontaneous combustion of drying oils as a fire cause, http://www.tcforensic.com.au/docs/uts/essay6.pdf#search='temperature iron combustion', as on Aug. 27, 2005.

Reed-Hill, R.E., Abbaschian, R. (1994) Physical Metallurgy Principles, PWS Publishing Company, Boston, MA, 427-428.

Robinson, J.W. (1973) Finite-difference simulation of an electrical discharge in water, J. Appl. Phys. 44 76-81.

Saada, A.S. (1993) Elasticity Theory and Applications, 2nd Edition, Krieger, Malabar, FL, 117.

Satio, N., Kobayashi, K. (1968) Research into electro-discharge machine, Bull. Soc. Precision Eng. 2 280.

Schulze, H.P., Herms, R., Juhr, H., Schaetzing, W., Wollenberg, G. (2004) Comparison of measured and simulated crater morphology for EDM, Journal of Materials Processing Technology 149 (1-3) 316-22.

Schumacher, B.M. (1987) EDM technology for precision workpieces with excellent surface quality, Proceedings of 7th International Symposium of Electro Machining (ISEM VII), IFS Ltd., Birmingham, England, 124-135.

Shervani-Tabar, M.T., Abdullah, A., Shabgard, M.R. (2006) Numerical study on the dynamics of an electrical discharge generated bubble in EDM, Engineering Analytical

Boundary Element 30 503-514

Shugg, W.T. (1986) Handbook of Electrical and Electronic Insulating Materials, Van Nostrand Reinhold, New York, NY, 230-234 .

Simao, J., Lee, H.G., Aspinwall, D.K., Dewes, R.C., Aspinwall, E.M. (2003) Workpiece surface modification using electrical discharge machining, International Journal of Machine Tools & Manufacture 43 (2) 121-128.

Singh, P.N., Raghukandan, K., Rathinasabapathi, M.; Pai, B.C. (2004) Electric discharge machining of Al-10%SiCP as-cast metal matrix composites, Journal of Materials Processing Technology 155-156 (1-3) 1653-1657.

Snoeys, R., Van Dijck, F. (1972) Plasma channel diameter growth affects stock removal in EDM, Annals of the CIRP 21 39-40.

Soni, J.S., Chakraverti, G. (1996) Experimental investigation on migration of material during EDM of die steel (T215 Cr12), Journal of Materials Processing Technology 56 (1-4) 439-451.

Suzuki, K., Iwai, M., Sharma, A., Ninomiya, S., Uematsu, T., Sano, S. (2005) Performance of an electrically conductive CVD diamond electrode for EDM and FEM analysis for a very low wear, Key Engineering Materials (291-292) 543-548.

Takeuchi, H., Kunieda, M. (2007) Effects of volume fraction of bubbles in discharge gap on machining phenomena of EDM, Proceedings of 15th International Symposium on Electromachining, ISEM XV, Pittsburg, USA 63-68.

Tanimura, T., Isuzugawa, K., Fujita, I., Iwamoto, A., Kamitani, T. (1989) Development of EDM in the mist, Proc. ISEM 9 313-316.

Tamura, T., Kobayashi, Y. (2004) Measurement of impulsive forces and crater formation in impulse discharge, Journal of Materials Processing Technology 149 (1-3) 212-216.

Tlusty, J., High-speed machining (1993) Annals of the CIRP 42(2) 733-738.

Tohi, M., Komatsu, T. Kunieda, M. (2002) Measurement of process reaction force in EDM using Hopkinson bar method, International Journal of Japan Society of Precision Engineering 68 822-826 (in Japanese).

Tomlinson, W.J., Adkin, J.R. (1992) Surface Engineering 8 (4) 283-288.

Tzeng, Y.F., Chiu, N.H. (2003) Two-phase parameter design for the optimization of the electrical-discharge machining process using a Taguchi dynamic experiment, International Journal of Advanced Manufacturing Technology 21 (12) 1005-1014.

Van Dijck, F.S., Dutre, W.L. (1974) Heat conduction model for the calculation of the volume of molten metal in electric discharges, Journal of Physics D: Applied Physics 7 (6) 899-910.

Vedensky, B.A., Vul, B.M., (1965) Encyclopedia Dictionary in Physics 4, Soviet Encyclopedia Publishing House, Moscow.

Wang, T., Kunieda, M. (2004) Dry WEDM for finish cut, Key Engineering Materials, (259-260) 562-566.

Wang, Z.L., Fang, Y., Wu, P.N., Zhao, W.S., Cheng, K. (2002) Surface modification process by electrical discharge machining with a Ti powder green compact electrode, Journal of Materials Processing Technology 129 (1-3) 139-142.

Wong, Y.S., Lim, L.C., Rahuman, I; Tee, W.M. (1998) Near-mirror-finish phenomenon in EDM using powder-mixed dielectric, Journal of Materials Processing Technology 79 (1-3) 30-40.

Wong, Y.S., Rahman, M., Lim, H.S., Han, H., Ravi, N. (2003) Investigation of micro-EDM material removal characteristics using single RC-pulse discharges, Journal of Materials Processing Technology 140 303-307.

Wu, K.L., Yan, B. H., Huang, F.Y., Chen, S.C. (2005) Improvement of surface finish on SKD steel using electro-discharge machining with aluminum and surfactant added dielectric, International Journal of Machine Tools & Manufacture 45 (10) 1195-201.

Xia, H., Hashimoto, H., Kunieda, M., Nishiwaki, N. (1996) Measurement of energy distribution in continuous EDM process, J. of JSPE 62 (8) 1141-1145.

Xia, H., Kunieda, M., Nishiwaki, N. (1996) Removal amount difference between anode and cathode in EDM process, IJEM 1 45-52.

Yan, B.H., Tsai, H.C., Huang, F.Y. (2005) The effect in EDM of a dielectric of a urea solution in water on modifying the surface of titanium, International Journal of Machine Tools & Manufacture 45 (2) 194-200.

Yan, B.H., Wang, C.C., Liu, W.D., Huang, F.Y. (2000) Machining characteristics of Al2O3/6061Al composite using rotary EDM with a disklike electrode, International Journal of Advanced Manufacturing Technology 16 (5) 322-333.

Yang, D.Y., Cao, F.G. (2007) The development of mirror machining in EDM sinking process, Proceedings of 15th International Symposium of Electro Machining (ISEM XV), Industrial and Management Systems Engineering, Pittsburgh, PA, 57-62.

Yaws, C.L. (1995) Handbook of Transport Property Data: Viscosity, Thermal conductivity, and Diffusion Coefficients of Liquids and Gases, Gulf Pub. Co., Houston, TX, 192-193.

Yeo, S.H., Kurnia, W., Tan, P.C. (2007) Electro-thermal modelling of anode and cathode in micro-EDM, Journal of Physics D: Applied Physics 40 (8) 2513-2521.

Yeo, S.H., Tan, H.C., New A.K. (1998) Assessment of waste streams in electric-discharge machining for environmental impact analysis, Proceedings of the Institution of Mechanical Engineers, Part B: Journal of Engineering Manufacture, 212 (B5) 393-401.

Yu, Z.B., Jun, T., Kunieda, M. (2004) Dry electrical discharge machining of cemented carbide, Journal of Materials Processing Technology 149 (1-3) 353-357.

Zhang, Q.H., Zhang, J.H., Deng, J.X., Qin, Y., Niu, Z.W. (2002) Ultrasonic vibration electrical discharge machining in gas, Processing Technology 129 (1-3) 135-138.

Zhao, F.L., Lu, Z.Z., Wang, H., Qian, Z.Q. (2005) Research on effecting mechanism of particles in powder-mixed EDM, Journal of Dalian University of Technology 45 (5) 668-671.

Zologtykh, B.N. (1961) The mechanisim of electrical erosion of metals in liquid dielectric medium, Proceedings of the Conference on Electro-erosion Machining of Metals, 1 Moscow.